This is to certify that the
dissertation entitled

COMPOSITE MATERIAL DESIGN AND
CHARACTERIZATION FOR RF APPLICATIONS

presented by

DANIEL STEVEN KILLIPS

has been accepted towards fulfillment
of the requirements for the

Doctoral degree in Electrical Engineering

Major Professor's Signature

15 Aug 2007

Date

Composite Material Design and Characterization for RF Applications

By

Daniel Steven Killips

A DISSERTATION

Submitted to
Michigan State University
in partial fulfillment of the requirements
for the degree of

DOCTOR OF PHILOSOPHY

Electrical Engineering

2007

ABSTRACT

Composite Material Design and Characterization for RF Applications

By

Daniel Steven Killips

As radio frequency technology continues to evolve, understanding of the electromagnetic behavior of materials is increasingly significant. Applications of such materials can range from radomes in which controlled transmission is required, to radar absorbing materials in which high loss and low reflection is a dominant factor. This is the motivation for creating materials in which the permittivity and permeability can be controlled depending upon the application.

The design of such materials, which will ultimately determine the effective permittivity and permeability, will depend on such factors as: geometry, volume fraction, thickness, and permittivity and permeability of the individual materials being combined. Composite design using classic mixing formulae, such as Maxwell-Garnet and Bruggeman formulations, are not valid for dense composites or ones possessing significant coupling between inclusions. Hence, more accurate homogenization techniques are needed. For layered composites, alternating dielectric and magnetic layers simulated using the method of wave matrices for both isotropic and anisotropic layers is both useful and efficient. For composites consisting of rod shaped inclusions, an integral equation based formulation is utilized.

In addition to material design, care must be taken in characterization of these materials such that the effective material properties are valid. Various characterization methods and fixtures are used in this work to determine effective properties for a variety of composite materials. These composites were fabricated both at Michigan State University and at partner universities over the past several years.

For Shana and Ella

ACKNOWLEDGMENTS

There are many who deserve thanks and appreciation. I must first extend my gratitude Dr. Leo Kempel for extending to me the opportunity to continue my education with Michigan State University. This experience has been invaluable to both my development as a researcher and as a person who enjoyed and cherished the advice given to me. Another special thanks is extended to Dr. Ed Rothwell, who has continued to spark my interest in electromagnetics since my sophomore year. Dr. Rothwell has also been available countless times to answer questions in times of confusion for a wide range of topics. To Dr. Shanker Balasubraniam, much appreciation for his consultation on the integral equation formulation including the use of the periodic Green's function. Also, his classes have given me a better understanding of some of the more complex topics in theoretical electromagnetics. Thanks to Dr. Martin Hawley for agreeing to participate in my graduate committee and for his excellent recommendations on how to improve my dissertation. Recognition must be extended to Dr. Charles Lee from AFOSR for this work performed under grants F-496-2002-10196 and FA9550-06-1-0023 as well as the NSF Career grant, ECS-0134236. Drs. Mark Scott and Jeff Berrie have provided very beneficial conversations on the topics of magnetics and composite materials. Also, Dr. Stephen W. Schneider deserves appreciation for his thoughts contributing to the motivation for this work. Finally, I would like to thank my wife, Shana, for her love and support and for putting up with me throughout this process. Not to mention, she gave me a beautiful daughter who was able to help me keep smiling through even the most stressful times.

TABLE OF CONTENTS

LIST OF TABLES

LIST OF FIGURES

KEY TO SYMBOLS AND ABBREVIATIONS

$\hat{a}$: Unit vector

$\overline{A}$: Column Vector

$\overline{\overline{a}}$: Rank 2 Tensor

$\overrightarrow{A}$: Spatial Vector

MUT: Material Under Test

TEM: Transverse Electromagnetic

FMR: Ferrimagnetic Resonance

TM: Transverse Magnetic

IE: Integral Equation

EFIE: Electric Field Integral Equation

PEC: Perfect Electric Conductor

CHAPTER 1

INTRODUCTION

The motivation in this dissertation is to be capable of understanding how different geometries of composite mixtures can effect the electromagnetic properties of materials, called permittivity and permeability. Typically, an RF designer is constrained to certain electromagnetic characteristics of materials which are available in bulk form. A potential solution to this problem is to add an additional degree of freedom in the design of RF devices, namely the capability to design a composite material that best fits the application. This could range from circumstances requiring total transmission such as in the case of a radome structure generally used to protect an antenna from the elements. Ideally, the permittivity and permeability would be designed to be equal to each in order to provide a better impedance match to free space which minimizes reflection. In addition, the product of the permittivity and permeability would be designed to be as low as possible in order to reduce the index of refraction. Another potential application would be used for antenna loading. Typically, designers use dielectric loadings in antennas in order to reduce the overall size of the antenna. However, the addition of dielectric materials increases the capacitance of the antenna substrate and subsequently results in a degradation in the bandwidth. It has been proposed by Hansen [1] that an antenna with a magneto-dielectric substrate can further reduce the surface are of a patch antenna but also increase the bandwidth. In this situation, the product of the permittivity and permeability would need to be as high as possible in order to fully decrease the size of the antenna. This is just a subset of the potential benefits of having the capability to design a composite material with appropriate values of permittivity and permeability.

The analysis performed in this dissertation will form a foundation for the understanding of the electromagnetic properties of two-phase composite materials for three different geometries. These geometries include; composites with spherical inclusions analyzed using classical mixing laws, layered composites using method of wave matrices for both isotropic and anisotropic layers, and composites with cylindrical inclusions using the method of moments. It will be demonstrated how the volume fraction and differences in permittivity and permeability between the two-phases can be used to tune the effective permittivity and permeability of the composites. An additional degree of freedom in the layered composites is provided based on the number of layers in the direction of propagation. The unique contribution in this work involves analysis of the composites consisting of layers and columnar inclusions based on the effective permittivity and permeability. In this stage of development, the analysis is purely theoretical, however experimental verification is a crucial portion of future work in order to further the design methodology.

This chapter provides an introduction to the concept of permittivity and permeability, composites and methods of characterizing these materials. It should form a good basis for main concepts covered in this dissertation while chapter 2 will go into greater detail about the motivation and composite structures.

1.1 Permittivity and Permeability

The interaction of electromagnetic fields with their surrounding mediums can be described with various concepts including polarization, susceptibility, and even conductivity to describe one type of loss mechanism. This work focuses on the parameters permittivity and permeability which signify the dielectric and magnetic properties of materials, respectively. Mathematically, this can be seen in (1.1), where both permittivity, $\overline{\overline{\varepsilon}}$ and permeability, $\overline{\overline{\mu}}$ are in their most general form and the double overlines indicate that these quantities are rank 2 tensors.

$$\vec{D} = \bar{\bar{\varepsilon}}\vec{E} \tag{1.1a}$$

$$\vec{B} = \bar{\bar{\mu}}\vec{H} \tag{1.1b}$$

The vector field quantites will be referred to as follows: $\vec{B}$ and $\vec{D}$ are the magnetic and electric *flux densities*, respectively, while $\vec{H}$ and $\vec{E}$ are the magnetic and electric *field intensities*, respectively. For time-harmonic fields, many materials can have both ε and μ represented using complex scalar quantities, where $\mu_0 = 4\pi * 10^{-7}(H/m)$ and $\varepsilon_0 \simeq 8.854 * 10^{-12}(F/m)$ are the permeability and permittivity of free space.

$$\mu = \mu_0(\mu_r' - j\mu_r'') \tag{1.2a}$$

$$\varepsilon = \varepsilon_0(\varepsilon_r' - j\varepsilon_r'') \tag{1.2b}$$

The time convention $e^{+j\omega t}$ is assumed for all the work done in this dissertation. The real portion of these values represents the stored power while the imaginary portion represents the dissipated power and the ratio of imaginary to real is referred to as the loss tangent. It should be noted, that the quantities in paranthesis in (1.2), are relative values and therefore are dimensionless.

The motivation of this work is to accurately calculate the permittivity and permeability of materials with an ultimate goal of composite design in which both μ and ε can be adjusted to better fit a particular application.

1.2 Composites

The majority of the analysis in this work consists of two-phase composite materials, involving dielectric-dielectric or dielectric-magnetic mixtures. These composites are clearly inhomogeneous, meaning the values of permeability and permittivity vary with position within the material. Therefore, *homogenization* of the composites is a term that will be introduced which implies that an *effective* permeability and permittivity will be used to represent an inhomogeneous mixture. The three different geometries to be investigated are: spherical particles mixed in a background, alternating layered structures, and finally rod shaped inclusions mixed in a background material [2]. In the following chapters, all three of these composite geometries will be analyzed using different methods.

The composite consisting of spherical particles has been previously analyzed [3] using classical mixing formulae [4] and compared to experimentally obtained data. It was shown that these mixing laws become less reliable to accurately predict the permittivity as the volume of the particles relative to the total volume of the composite is increased. These mixing laws are even more unrelieable in the ability to predict permeability for even small volume fractions. One reason for this inaccuracy is due to the fact that these classical mixing formulae do not account for particle to particle interaction.

Next, layered composites will be analyzed using the method of wave matrices for both isotropic and anisotropic layers. The reason for modeling anisotropic layers is to account for the tensor permeability that is common with many ferrimagnetic materials. The effect of layering will be investigated for both dielectric-dielectric and dielectric-magnetic composites. It can be seen that as the volume fraction, thickness, and constrast ratio of both permittivity and permeability are varied the homogenized values can be predicted and controlled. This provides a good foundation for design of composite materials for which a layered structure compliments the given application.

The final geometry to be analyzed will involve an integral equation formulation to solve for the scattered fields due to periodically arranged cylindrical rods in a background material. Volume fraction is shown to be the dominant factor for electromagnetic design of this composite type.

1.3 Material Characterization

Material characterization is the process of measuring some particular property of a sample and using that value to calculate or extract the material properties. Many characterization techniques are employed at Michigan State University, however only two of such techniques will be discussed here as they are sufficient for the needs of this work. The first technique involves a stripline field applicator [5] and the HP8510 Network Analyzer. A sample is inserted into the stripline and the scattering parameters are measured using the Network Analyzer. The permittivity and permeability are then extracted from the measured S-parameters using a traditional root searching algorithm. This structure is particularly useful due to its broadband nature and the capability to clamp the MUT (Material Under Test) into place which minimizes error due to air gaps. Samples can be characterized using this method in the frequency range 1GHz-18GHz.

The latter of these characterization techniques involves the E4991A Impedance Analyzer and both dielectric and magnetic test fixtures [6]. The permittivity and permeability are calculated from measured capacitance and inductance, respectively. These test fixtures are operational in the frequency range 1MHz-1GHz.

These characterization techniques allow for experimental verification of composites in a wide range of frequencies. This is a crucial contribution to the development of a solid design method for composites used in electromagnetic applications.

CHAPTER 2

COMPOSITE BACKGROUND AND CHARACTERIZATION

2.1 Motivation

Understanding of the electromagnetic behavior of materials continues to gain importance as radio frequency technology continues to grow [7]-[16]. These materials are used in a wide range of applications from radomes in which controlled transmission is required, to radar absorbing materials in which high loss and low reflection is a dominant factor. Within this range, applications such as antenna substrates are used to reduce antenna surface area, increase bandwidth, or modify the input impedance. Many times, either the material with the most desirable properties is unavailable in its bulk form or the technology is designed around a readily available material. It is therefore advantageous to have the capability to choose the properties of the material such that it best fits the particular application. One possible method to achieve this design is through the use of composite materials.

Electromagnetic omposites are mixtures of two or more dissimilar materials, either dielectric or magnetic, combined in a matter in order to control the effective permittivity and permeability. The effort in determining a solid composite design can be split into three basic activities. The first activity involves material synthesis. This centers around creating the materials being simulated and understanding the binding and dispersion processes involved when attempting to combine multiple materials. The author's contribution to this activity was to consult with the chemical engineers, material scientists, and chemists on the topic of electromagnetics. However, section 2.3 has been devoted to this topic in a very broad sense to assist in the understanding of composite design process. The next activity incorporates the computional effort ivolved. A suitable simulation of the composite is needed for a complete understanding of how the different mixtures can be modified to adjust the effective permittivity and permeability. The simulation methods used will include classical mixing formulae, analytical solutions, and computational electromagnetic techiniques. Experimental verification of these simulations is also of great importance and is the final activity of composite design. Numerous techniques are available for characterizing materials [17]-[26], two of them will be discussed in section 2.4. The remainder of this work is on the analysis of three different geometries of composites illustrated in Figure 2.1. The first of these composites consisting of spherical inclusions is discussed in the last section of this chapter. Layered materials are investigated for isotropic materials in Chapter 3 and anisotropic layers in Chapter 4. The final geometry with rod shaped inclusions is examined in Chapter 5.

It has been suggested here that a composite material would be highly useful for situations where a bulk material is not commonly found with the desired electromagnetic properties. However, even if the desired properties are found in a bulk material, composites could also be valuable in situations where the flexibility or conformability of the material is of importance. Perhaps the weight of the material is an issue and a composite material can be shown to have the same electromagnetic properties but exhibit less density. Finally, with proper understanding of electromagnetic material properties and composite simulation, a design method could be formulated for which an appropriate mixture is devised that best fits the application.

2.2 Homogenization

Consider a material occupying a volume region V enclosed by a surface S as illustrated in Figure 2.2 where the left body shows an inhomogenous material and the right body shows an effectively homogeneous material. To a wave, the homogenized material "looks" like it is a material occupying region V with the effective material properties.

$$\langle \overrightarrow{D} \rangle = \varepsilon_{eff} \langle \overrightarrow{E} \rangle \tag{2.1a}$$

$$\langle \overrightarrow{B} \rangle = \mu_{eff} \langle \overrightarrow{H} \rangle \tag{2.1b}$$

Equation (2.1) gives a mathematical representation of this concept where $\langle\rangle$ is a spatial average of the fields and the subscript $'eff'$ stands for effective. The effective permittivity and permeability are the design goals for the composites discussed throughout this dissertation.

2.3 Composite Synthesis

As mentioned above, composites consist of two or more dissimilar materials combined in order to achieve some property, physical or chemical, which cannot be found in those materials in their bulk form. The materials within a composite can be specified by one of two categories, matrix and reinforcement [27]. The matrix phase is the material which surrounds and supports the reinforcement phase keeping the geometry fixed in position. The reinforcement phase is needed to create the necessary parameters for the application in which the composite will be utilized. The matrix phase is commonly a form of plastic or polymer, while the reinforcement phase can be anything from carbon or magnetic powders and fibers to metallic rods of flakes depending on the desired end product. Various methods can be employed in order to process and manufacture composites. Only a few are introduced in this section and are only be briefly summarized since the focus of this work is on the electromagnetics of composites. The first method is *hand lay-up molding* where the reinforcement is put into position and the matrix is painted layer by layer until the desired thickness has been reached [28]. The advantages of this time consuming process is the ability to align the fiber reinforcement materials as needed and to accomodate for irregular shaped objects. A less time consuming process called *spray-up molding* uses a cutter to chop up the fiber reinforcement which is sprayed onto a mold with a combination of resin mist and catalyst. The mixture cures on the mold at room temperature and is finished. An advantage besides lower time consumption is the ability to handle large, complex objects due to the spraying operation. *Compression molding* uses a hydraulic press to compress the mixture or layers created by hand lay-up at an elevated temperature and help until the composite has cured. The compression allows the mixture to be distributed properly over the entire mold giving it the ability to mold large and fairly intricate products. Finally, *injection molding* involves heating the material into a molten state then injecting it into a mold at very high pressure where it cools to solidification. A few polymer processing techniques have been introduced with a brief description in order to include all aspects of composite design. The focus of this work however, does not involve material production and thus that topic will be left for this section alone. Also, it should be noted that the terminology, matrix and reinforcement, in this section was based on [27],[28] and will not be used anywhere else in this dissertation. The corresponding terminology for matrix is either background or environment, and inclusions for reinforcement.

2.4 Composite Characterization

Both permittivity and permeability are not values that are easily measured through direct methods. However, it is convenient to measure other quantities such as reflection, transmission and impedance from which the permittivity and permeability can be extracted.

2.4.1 Dielectric Test Fixture and Impedance Analyzer

The first method involves the Agilent E4991A Impedance Analyzer and 16453A Dielectric Test Fixture [6]. The dielectric test fixture measures the admittance of the material under test (MUT) between two electrodes within the fixture as seen in Figure 2.3 from 1MHz to 1GHz. Figure 2.3a and Figure 2.3b show the test fixture and a close up look at the electrodes. Figure 2.3c illustrates the electric field lines between the electrodes, including the fringing effects.

Prior to taking this measurement, a three part calibration process must be performed. This includes an open measurement with the electrodes separated by a fixed distance, a shorted measurement with the electrodes in contact with each other, and the final measurement with a known load, e.g. Teflon. Once the calibration is completed, the measured complex admittance can be represented by (2.2).

$$Y = G + j\omega C_p \tag{2.2}$$

The real part, G, is the conductance and represents dielectric loss. The imaginary part, C_p, is the capacitance between the parallel plate electrodes and ω is the angular frequency. The effective relative permittivity of the MUT can then be calculated by (2.3) where C_0 is the capacitance of an empty test fixture.

$$\varepsilon_r = \frac{C_p}{C_0} - j\frac{G}{\omega C_0} \tag{2.3}$$

Figure 2.4 shows the measured real and imaginary values of permittivity for a sample of acrylic which has a known relative permittivity of $\varepsilon = 2.6 - j0$. Also included in the figure is a device uncertainty bar that illustrates the potential range of variation in measurement results. This uncertainty is calculated using (2.4) where t is the thickness of the sample in mm, f is the frequency in GHz, and ε'_{rm} is the real part of the measured permittivity.

$$\frac{\Delta\,\varepsilon'_{rm}}{\varepsilon'_{rm}} = \pm\left[5 + \left(10 + \frac{0.1}{f}\right)\frac{t}{\varepsilon'_{rm}} + 0.25\frac{\varepsilon'_{rm}}{t} + \frac{100}{\left|1 - \left(\frac{13}{f\sqrt{\varepsilon'_{rm}}}\right)^2\right|}\right]\ [\%] \qquad (2.4)$$

The complete calibration to measurment procedure is repeated five times to ensure consistency and accuracy of the measurements and to check that the data is well within the uncertainty bars.

2.4.2 Magnetic Test Fixture and Impedance Analyzer

The next method involves the Agilent E4991A Impedance Analyzer and 16454A Magnetic Test Fixture [6]. This test fixture measures the inductance in a toroidal shaped sample as seen in Figure 2.5 from 1MHz to 1GHz. The inductance within the fixture is created from current flowing upwards through the center conductor and then outward and down the walls of the fixture. This current loop forms a magnetic flux, which by the right hand rule, is in the direction normal to the surface created by that loop. Mathematically, the relationship between the inductance and magnetic flux density is given by (2.5), where $\overrightarrow{B}$ is the magnetic flux density vector and I is the magnitude of the current.

$$L = \frac{1}{I}\int \overrightarrow{B}\cdot\overrightarrow{dS} = \frac{1}{I}\int_0^{h_0}\int_a^e \frac{\mu}{2\pi\rho}d\rho dz \qquad (2.5)$$

As shown in Figure 2.5, h_0 is the height of the fixture, a is the diameter of the inner conductor, and e is the diameter of the fixture. All of these distances are in measured in mm,and the self inductance of an empty fixture is given by (2.6) and is an important contribution to the calibration procedure.

$$L_{ss} = \frac{\mu_0}{2\pi} h_0 \ln \frac{e}{a} \tag{2.6}$$

Before connecting the fixture to the test head a four part calibration process is performed. This includes an open, short, 50Ω load, and a low-loss capacitor. Once the test head has been properly calibrated, the fixture is attached and the self-inductance is measured and saved completing the calibration. Now the complex impedance Z_m of the material can be measured.

$$Z_m = R_s + j\omega L_s \tag{2.7}$$

Finally, the complex permeability can be calculated by (2.8).

$$\mu_r = \frac{2\pi Z_m - j\omega L_{ss}}{j\omega\mu_0 h \ln \frac{c}{b}} + 1 \tag{2.8}$$

The inner and outer radii of the MUT are given in mm by b and c, respectively and $\omega = 2\pi f$ where f is the frequency in GHz. Figure 2.6 shows the measured real and imaginary values of permittivity for a sample of acrylic which has a known relative permeability of $\mu_r = 1 - j0$. As with the dielectric measurements, Figure 2.6 has a device uncertainty bar which is calculated using (2.9).

$$\frac{\Delta\,\mu'_{rm}}{\mu'_{rm}} = \pm\left[4 + \frac{0.02}{f}\left(\frac{25}{h\ln(c/b)\,\mu'_{rm}}\right) + h\ln\left(\frac{c}{b}\right)\mu'_{rm}\left(1 + \frac{15}{h\ln(c/b)\,\mu'_{rm}}\right)^2 f^2\right] [\%] \tag{2.9}$$

2.4.3 Stripline Field Applicator

The stripline is a waveguiding structure consisting of two parallel conducting plates with a thin conducting strip down the center. Figure 2.7 shows a side view of the stripline and placement of the material under test. The stripline supports a Transverse

Electromagnetic (TEM) wave with zero frequency cutoff and the design described herein allows for measurements over a wide range of frequencies, namely 1-18GHz. One advantage the stripline has over similar measurement techniques using coaxial and rectangular waveguides is the ability to clamp the material in place and minimize air gaps. Also, the fields within the stripline are concentrated to the area surrounding the center conductor and are well confined [5] as illustrated in Figure 2.8.

Unlike the characterization procedures discussed in 2.4.1 and 2.4.2 where permittivity and permeability were determined through measured impedance, the stripline uses measured transmission and reflection. There are three sets of measurements needed to characterize these materials. The first set involves measuring transmission through and reflection from an empty stripline. The next step measures the reflection from a short placed in three different locations within the stripline and the final measurement is done with a sample inside the stripline.

One method for obtaining both permittivity and permeability involves comparing the measured and calculated propagation constant within the material region, β, and reflection coefficient from the interface of the material, Γ, until they are identical using a Newton's two-dimensional complex root-searching algorithm. The subscript "m" denotes measured values.

$$\beta(\varepsilon, \mu, \omega) - \beta_m(\omega) = 0 \tag{2.10a}$$

$$\Gamma(\varepsilon, \mu, \omega) - \Gamma_m(\omega) = 0 \tag{2.10b}$$

Both β and Γ can be related to permittivity and permeability using (2.11).

$$\beta = \frac{\omega}{c}\sqrt{\mu_r \varepsilon_r} \tag{2.11a}$$

$$\Gamma = \frac{\sqrt{\mu_r/\varepsilon_r} - 1}{\sqrt{\mu_r/\varepsilon_r} + 1} \tag{2.11b}$$

A technique developed by Nicholson, Ross, and Weir is used to calculate β_m and Γ_m from the measured S_{11} and S_{21} at the sample plane [5].

$$S_{11}^{s} = \frac{\Gamma_m \left(1 - z^2\right)}{1 - (\Gamma_m z)^2} \tag{2.12a}$$

$$S_{21}^{s} = \frac{z \left(1 - \Gamma_m^2\right)}{1 - (\Gamma_m z)^2} \tag{2.12b}$$

$$z = \exp(-j\beta_m t_s) \tag{2.12c}$$

The subscript/superscript "s" denotes sample plane S-parameters which can be found from the measured S-parameters at the stripline terminals using a de-embedding technique. The sample thickness is given as t_s and the complex permittivity and permeability are given by (2.13b).

$$\varepsilon_r = \frac{\beta}{k_0}\left(\frac{1-\Gamma}{1+\Gamma}\right) \tag{2.13a}$$

$$\mu_r = \frac{\beta}{k_0}\left(\frac{1+\Gamma}{1-\Gamma}\right) \tag{2.13b}$$

Finally, measured permittivity and permeability for acylic is shown in Figure 2.9 and is in agreement with previous measurements.

2.5 Previous Work: Spherical Inclusions and Classical Mixing Rules

Composites consisting of dielectric spherical particles mixed throughout a dielectric background have been studied for over a hundred years providing many classical mixing laws to predict effective permittivity [4]. Several of these classical mixing laws have been summarized and tested against experimental data using the stripline method discussed in section 2.4.3 for magneto-dielectric composites to check for accuracy in predicting BOTH effective permittivity and permeability [3, 29]. A summary of three of these classical mixing laws as well as general conclusions are provided in this section. The three classical mixing laws, Maxwell-Garnett, Bruggeman, and Coherent Potential, were chosen because of the difference in their basic philosphy on homogenization. Figure 2.10 is a geometrical representation of a composite with spherical inclusions where subscripts i and e denote inclusion and environment phases, respectively. A necessary assumption in the derivation of the classical mixing laws is that the spherical particles are small enough in diameter such that they approximately obey the rules of electrostatics and magnetostatics. The maximum diameter, as defined by Sihvola and Kong [30] is given by (2.14), and is appoximately proportional to wavelength.

$$d_{max} \cong \frac{\lambda}{2\pi} \tag{2.14}$$

2.5.1 Maxwell Garnett

The first and probably most widely known mixing law to be discussed is the *Maxwell Garnett* formulation for effective permittivity shown in (2.15), where f is the volume fraction of the inclusions [31].

$$\varepsilon_{eff} = \varepsilon_e + 3f\varepsilon_e \frac{(\varepsilon_i - \varepsilon_e)}{\varepsilon_i + 2\varepsilon_e - f(\varepsilon_i - \varepsilon_e)} \tag{2.15}$$

This equation is based on the polarizability of a dielectric sphere, and algebraic manipulation of the spatial averaged electric fields. This formula is assymetric in that the inclusion phase affects the effective permittivity of the composite differently than the environment phase. This implies that the inclusion phase is considered a *guest* dispersed throughout the environment which is considered a *host*. The guest versus host philosophy is the foundation for the Maxwell Garnett formulation in that the inclusions are compared against the environment.

2.5.2 Bruggeman

The next mixing rule is the *Bruggeman* formulation, (2.16), for effective permittivity of a two-phase composite [32].

$$(1-f)\frac{\varepsilon_e - \varepsilon_{eff}}{\varepsilon_e + 2\varepsilon_{eff}} + f\frac{\varepsilon_i - \varepsilon_{eff}}{\varepsilon_i + 2\varepsilon_{eff}} = 0 \tag{2.16}$$

The major difference from Maxwell-Garnett is the symmetry of the Bruggeman formula which no longer employs a host versus guest philosophy. Instead, both the inclusions and environment phases are evaluated equally against the effective properties of the homogenized composite. This allows the environment to potentially provide the same contribution to the effective permittivity of the composite as the inclusions, unlike Maxwell-Garnett. Essentially, both the inclusions and environment are treated as inclusions within the entire medium. The *Bruggeman* formula is known by several names; *Polder van Santen*, *de Loor*, *Böttcherr*, and *effective medium model* [4],[32]-[36].

2.5.3 Coherent Potential

The final mixing rule discussed in this section is the *Coherent Potential* formula [37] which is seen in its most convenient form in (2.17) for spherical inclusions.

$$\varepsilon_{eff} = \varepsilon_e + f(\varepsilon_i - \varepsilon_e)\frac{3\varepsilon_{eff}}{3\varepsilon_{eff} + (1-f)(\varepsilon_i - \varepsilon_e)} \tag{2.17}$$

Unlike the previous two mixing rules which analyze the problem of a single scatterer approximation weighted by the volume fraction of the materials, the Coherent Potential formulation uses the Green's function to represent the polarization density of the effective medium [4].

2.5.4 Conclusions

All three of the classical mixing laws discussed in this section tend to predict the same effective permittivity as the volume fraction gets very small ($f \lessapprox 0.3$) and can all be approximated by (2.18) [4].

$$\varepsilon_{eff} \approx \varepsilon_e + 3f\varepsilon_e \frac{\varepsilon_i - \varepsilon_e}{\varepsilon_i + 2\varepsilon_e} \tag{2.18}$$

Another important factor in calculating the effective permittivity is the difference in the dielectric constant of the inclusion and environment phases. As the contrast gets small the mixing rules tend to agree and also predict the permittivity more accurately. The cause for this is due to the fact that the classical mixing laws do not take into account particle to particle interaction, thus as the volume fraction is increased and the particles become more tightly packed, these formulas will tend to deviate from each other and from the effective permittivity. See Figure 2.11 and Figure 2.12 for a graphical illustration of the effects of volume fraction and dielectric contrast. These figures compare the effective permittivity of the three classical mixing laws described in this chapter as a function of volume fraction.

When the volume fraction is low ($f \lessapprox 0.3$), and there is not a great dielectric contrast, all three of the classical mixing laws discussed here can be used to predict the effective permittivity of a composite with spherical particle inclusions fairly accurately. On the other hand, using these same classical mixing laws in attempting to predict permeability through the concept of duality between the electric and magnetic fields, the formulas were unable to yield accurate results and hence could not be used as a tool for composite simulation and design [3]. Another important observation in [3] and through extensive experience measuring materials with spherical magnetic particles, is that this geometry doesn't allow for a significant magnetization within the composite and thus the permeability is approximately unity and therefore is essentially non-magnetic. This is partially due to the fact that spherical ferrimagnetic particles have a demagnetization factor of 1/3 and hence these particles need to be very tightly packed in order to achieve an appreciable permeability. This difficulty is the motivation to progress to a new geometry for composite design. This new geometry is a layered structure and is discussed in chapters 3 and 4 for isotropic and anisotropic materials, respectively. The reason for layered composites is that it provides a controlled geometry which can be modeled using exact methods.

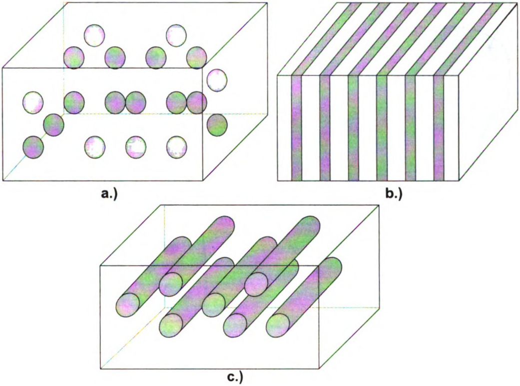

Figure 2.1. Possible Geometries for Composite Material Design

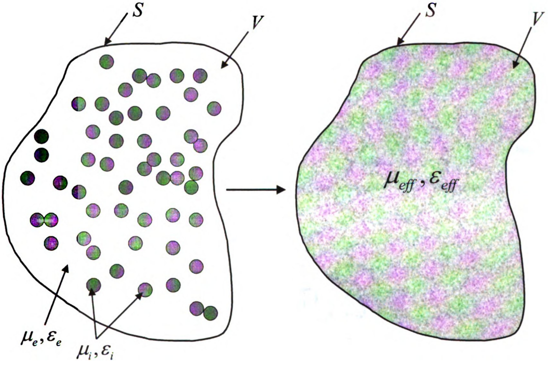

Figure 2.2. Homogenization Illustration

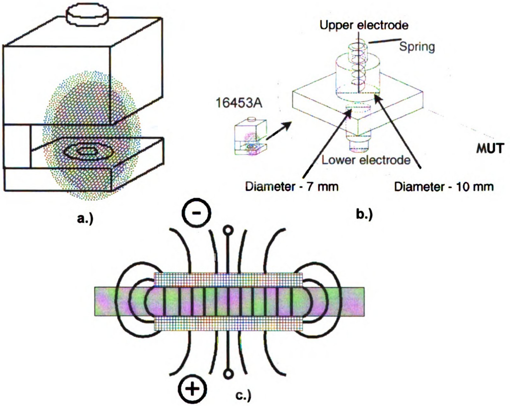

Figure 2.3. Agilent 16453A Dielectric Test Fixture [6].

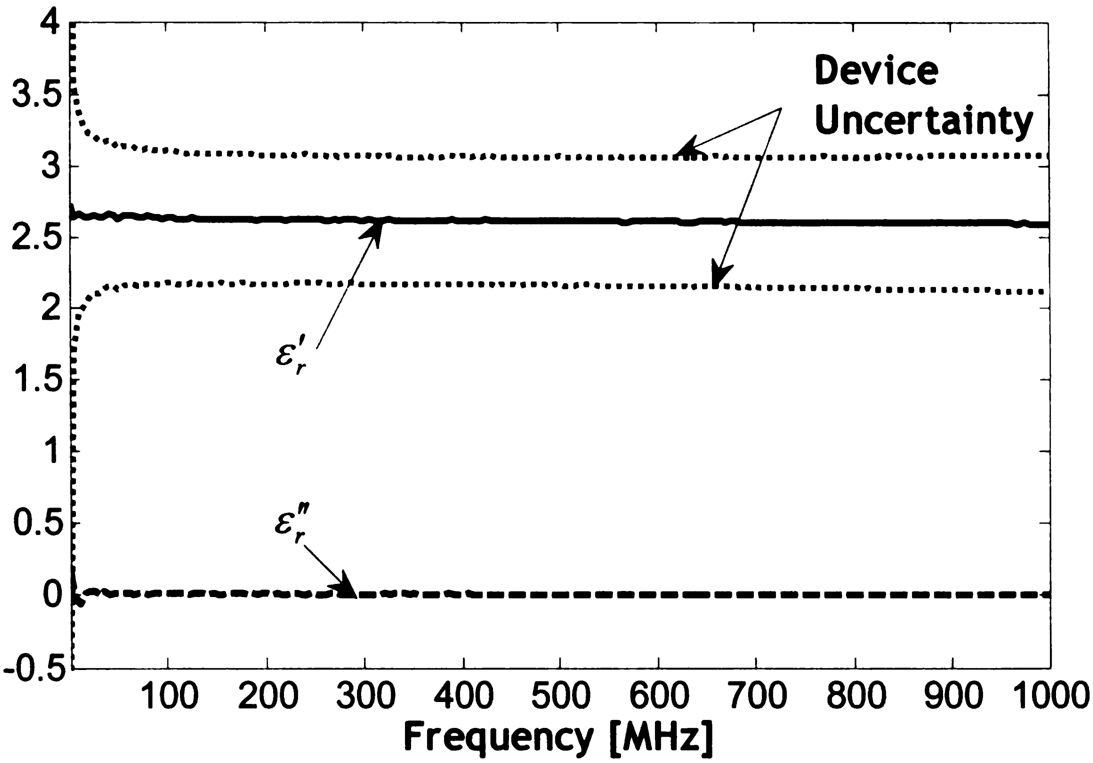

Figure 2.4. Measured permittivity of acrylic using 16453A Dielectric test fixture.

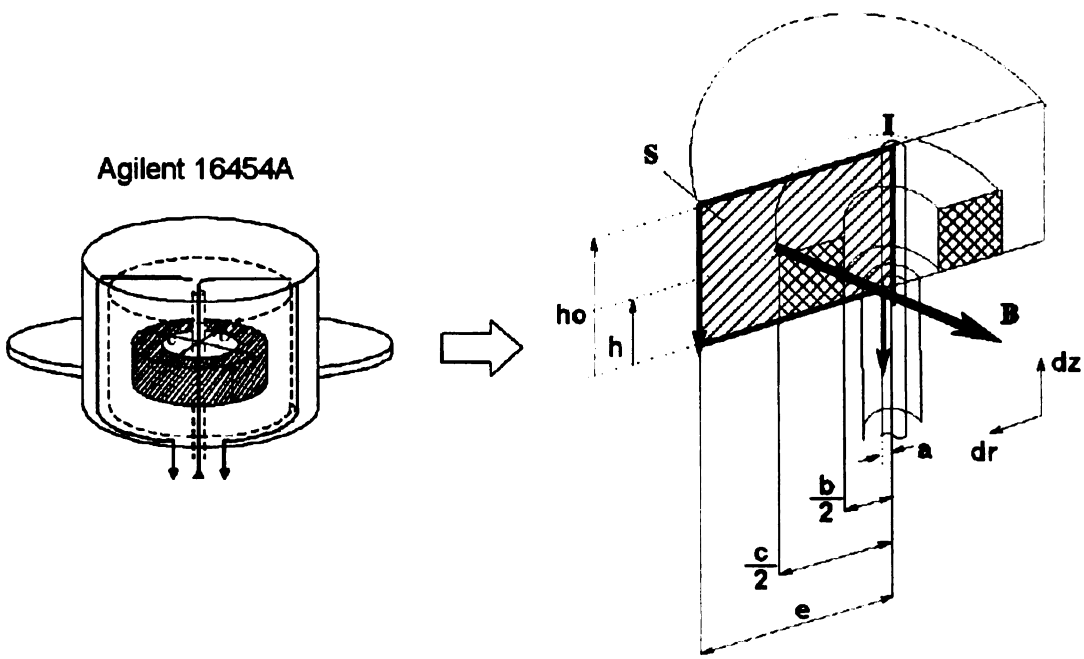

Figure 2.5. Agilent 16454A Magnetic Test Fixture [6].

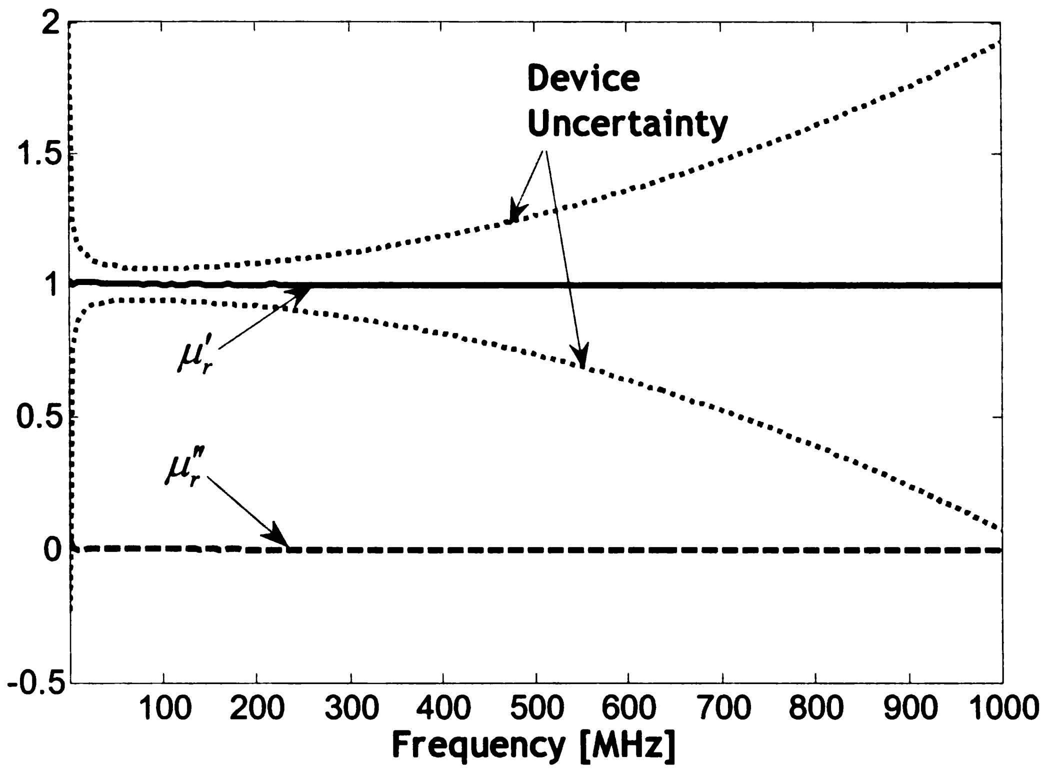

Figure 2.6. Measured permeability of acrylic using 16454A Magnetic test fixture.

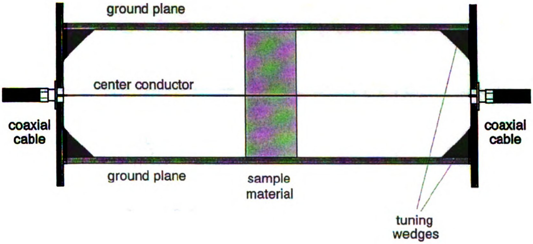

Figure 2.7. Sideview of the stripline field applicator [5].

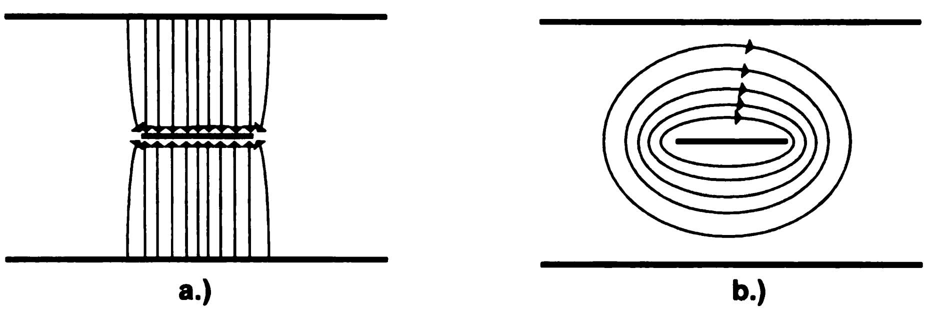

Figure 2.8. Field lines within the stripline: a.) Dynamic Electric Field, b.) Dynamic Magnetic Field.

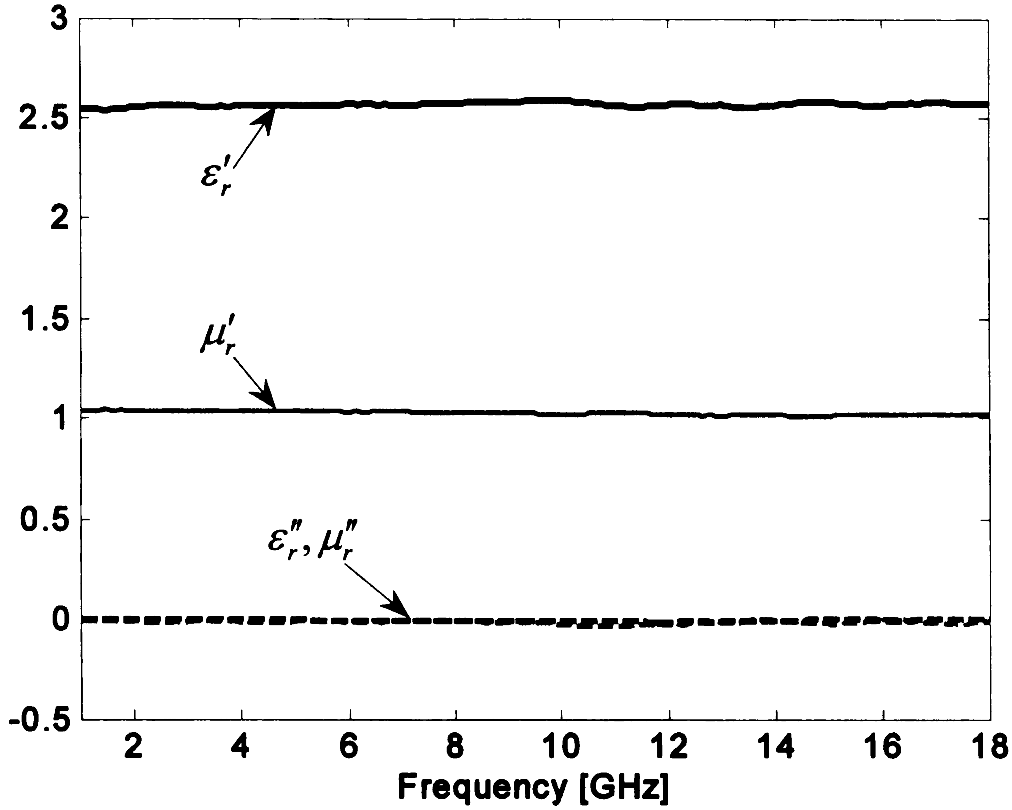

Figure 2.9. Measured permittivity and permeability of acrylic using stripline.

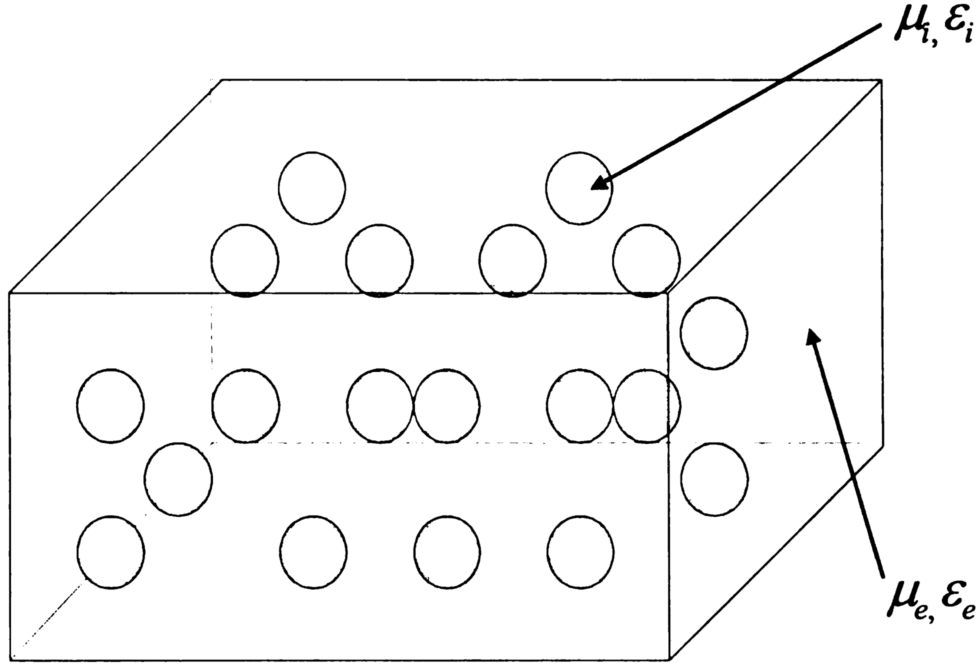

Figure 2.10. Composite with spherical inclusions

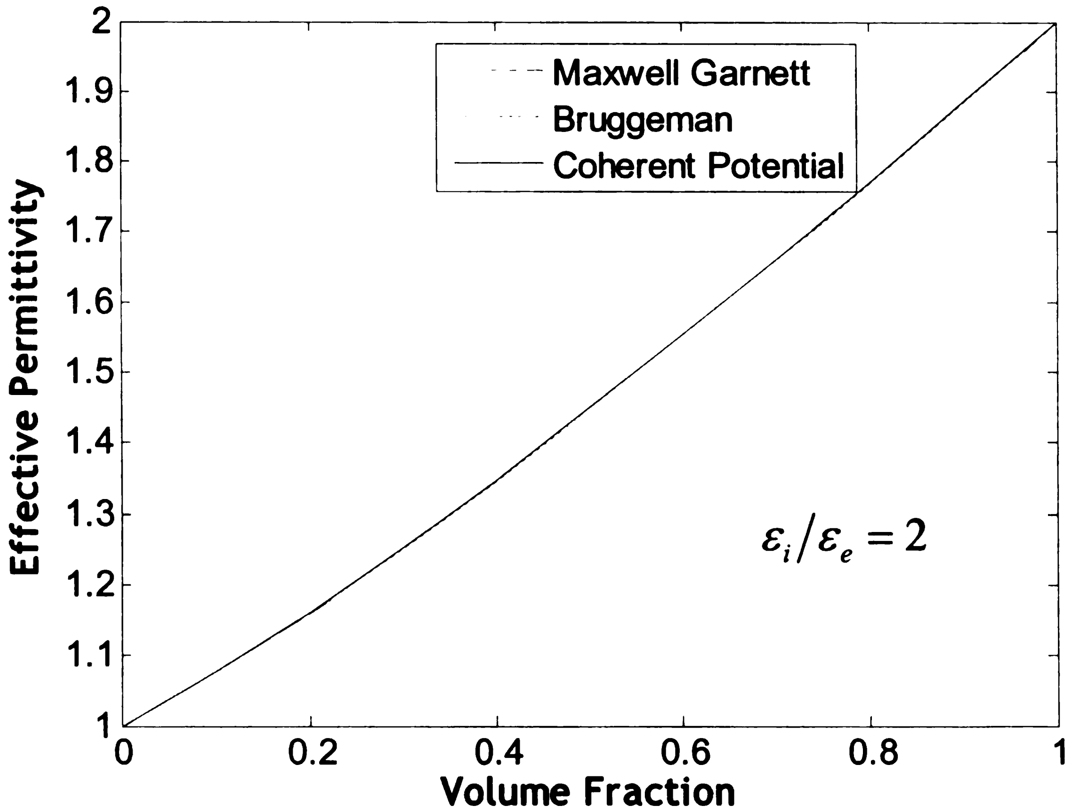

Figure 2.11. Comparison of 3 classical mixing laws for dielectric contrast ratio of $\varepsilon_i/\varepsilon_e = 2$.

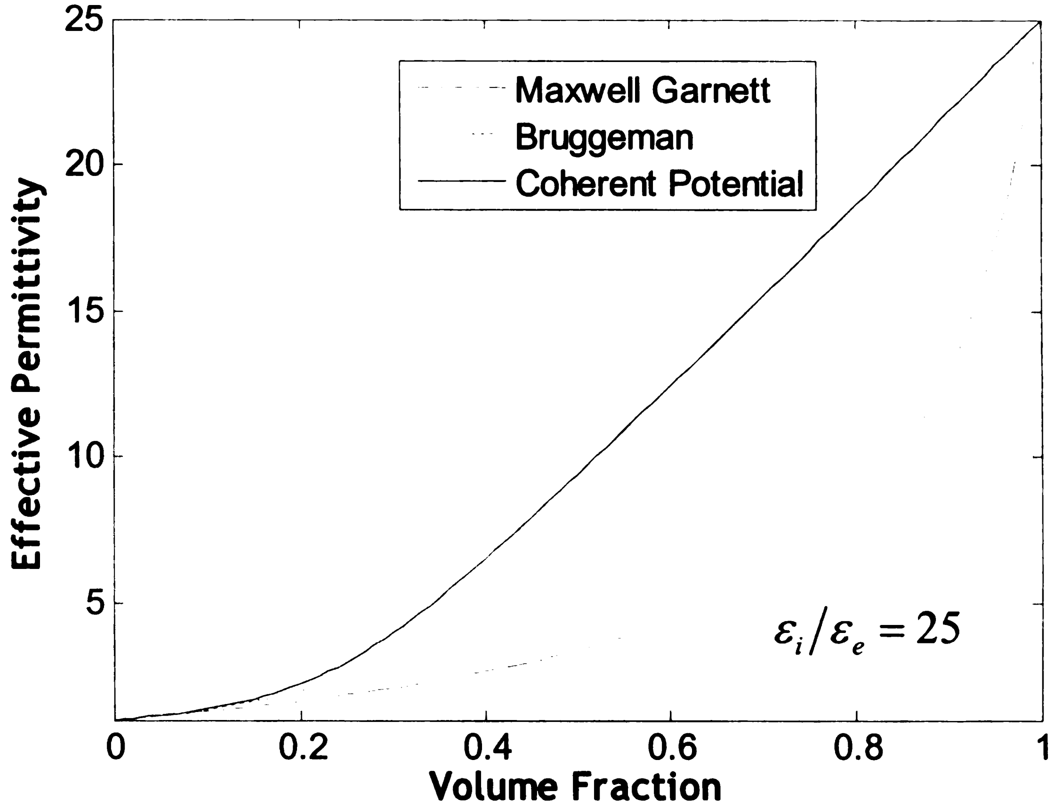

Figure 2.12. Comparison of 3 classical mixing laws for dielectric contrast ratio of $\varepsilon_i/\varepsilon_e = 25$.

CHAPTER 3

ISOTROPIC LAYERED COMPOSITES

This chapter focuses on composites consisting of layered isotropic materials with a geometry given by Figure 3.1. Isotropic materials are those in which $\overrightarrow{D}$ is related to $\overrightarrow{E}$ and $\overrightarrow{B}$ to $\overrightarrow{H}$ by complex scalar quantities such that the field direction in each pair is aligned [38].

$$\overrightarrow{D} = \varepsilon \overrightarrow{E} \tag{3.1a}$$

$$\overrightarrow{B} = \mu \overrightarrow{H} \tag{3.1b}$$

The focus of this chapter will be limited to the simulation of isotropic dielectric materials and the impact of layering on the effective permittivity of the composite. Magnetic materials are discussed in chapter 4. The analysis of this structure will be done using the method of wave matrices for planar layered dielectric materials assuming a plane wave normally incident on the interface. Although the wave matrix method is fully capable of handling oblique incidence, normal incidence is assumed here in order to accurately model the characterization procedure within the stripline described in section 2.4.3. Doing so will allow the effective permittivity to be extracted from the calculated scattering paramters using the same program as for the stripline. Also, with normal incidence, phase matching can be achieved at each interface. Section 3.1 derives this method in detail and follows directly from Collin [39]. Using wave matrices, a straightforward calculation of the reflection and transmission coefficients for a layered structure can be used in the extraction of complex effective permittivity as demonstrated in section 2.4.3 for the stripline material characterization technique.

In the design of a composite with tunable effective permittivity, there are three main parameters of interest. The number of layers, the difference in the dielectric constant of the two materials (dielectric contrast ratio), and the volume fraction of the layers will form a basis for the following analysis. To simplify the problem, the material layers are extended to infinity in the directions parallel to the interfaces but is finite in length in the direction perpendicular. Therefore, the analysis will proceed for several different dielectric contrast ratios and volume fractions. The layering effect will be examined by first holding the total thickness, d, fixed in length, while second increasing the number of layers within the composite. Hence, the volume fraction is kept constant. This is illustrated in Figure 3.2 where the first case involves material A on the outside, followed by interchanging the materials such that material B is on the outside. It will be demonstrated later that the effective permittivity is heavily persuaded by the outer layer for composites with a small number of layers. The permittivities of adjacent layers, A and B, are based on the dielectric contrast ratio and are therefore real numbers independent of frequency. Since the layers are non-dispersive, a frequency analysis is not performed here because the effective permittivity would be a constant value over any frequency range in which the sample thickness is not equal to or greater than a half wavelength. In that case, possible resonances could potentially cause problems in the characterization process.

3.1 Wave Matrix

The wave matrix method is an exceptionally useful and simple tool for the analysis of layered dielectrics. In the case of a normally incident plane wave, each layer can be completely described by its material properties (ε, μ) and thickness. This section begins with a derivation of reflection and transmission coefficients in terms of permittivity and permeability for one interface. This is followed by the implementation of multiple interfaces and finally the method of wave matrices.

3.1.1 Reflection and Transmission Coefficients

This study begins with the investigation of the reflection and transmission of a plane wave normally incident at the interface of a planar dielectric in the same plane as the transverse component of the wave. Figure 3.3 illustrates that when an incident wave arrives from the left (z<0) at the dielectric interface, part of that wave is reflected and part is transmitted. The incident and transmitted waves are shown traveling in the positive z-direction while the reflected wave is traveling in the negative z-direction. For this work, the time convention $e^{j\omega t}$ is assumed and suppressed which results in the following representation for the fields.

$$\vec{E}^i = \vec{\Psi}^i_E e^{-jk_1 z} \tag{3.2a}$$

$$\vec{E}^r = \vec{\Psi}^r_E e^{+jk_1 z} \tag{3.2b}$$

$$\vec{E}^t = \vec{\Psi}^t_E e^{-jk_2 z} \tag{3.2c}$$

The wavenumber, k, in (3.2) is dependent on frequency, permittivity and permeability and can be represented as $k_i = \omega\sqrt{\mu_i \varepsilon_i}$ where i could be either 1 or 2, and the vector amplitude coefficients for the transverse components of the electric fields are given by $\vec{\Psi}_E$. The transverse components of the magnetic field can be written in terms of the electric field amplitude coefficients and impedance matrices in each region.

$$\vec{\Psi}^i_H = \overline{\overline{Z}}_1^{-1} \cdot \vec{\Psi}^i_E \tag{3.3a}$$

$$\vec{\Psi}^r_H = \overline{\overline{Z}}_1^{-1} \cdot \vec{\Psi}^r_E \tag{3.3b}$$

$$\vec{\Psi}^t_H = -\overline{\overline{Z}}_2^{-1} \cdot \vec{\Psi}^t_E \tag{3.3c}$$

The inverse of the impedance matrix (admittance matrix) is given by $\overline{\overline{Y_i}} = \eta_i^{-1}(\hat{y}\hat{x} - \hat{x}\hat{y})$ where i is given by either 1 or 2 and the wave impedances by $\eta_i = \sqrt{\mu_i/\varepsilon_i}$. Assuming there are no currents or charge buildup along the interface, boundary conditions imply that the tangential fields must be continuous.

$$\overrightarrow{E}^{i}(z=0)+\overrightarrow{E}^{r}(z=0)=\overrightarrow{E}^{t}(z=0) \tag{3.4a}$$

$$\overrightarrow{H}^{i}(z=0)+\overrightarrow{H}^{r}(z=0)=\overrightarrow{H}^{t}(z=0) \tag{3.4b}$$

These boundary conditions can also be represented by the transverse components of the fields since these are tangent to the interface. Also, in the $z = 0$ plane, the exponentials in (3.2) becom unity.

$$\overrightarrow{\Psi}^{i}_{E}+\overrightarrow{\Psi}^{r}_{E}=\overrightarrow{\Psi}^{t}_{E} \tag{3.5a}$$

$$\overrightarrow{\Psi}^{i}_{H}+\overrightarrow{\Psi}^{r}_{H}=\overrightarrow{\Psi}^{t}_{H} \tag{3.5b}$$

Using (3.3), the magnetic field amplitued coefficients can be written in terms of the transverse electric field components and (3.5b) becomes

$$\overline{\overline{Z}}_{0}^{-1}\cdot\left(\sqrt{\frac{\varepsilon_{r1}}{\mu_{r1}}}\overrightarrow{\Psi}^{i}_{E}-\sqrt{\frac{\varepsilon_{r1}}{\mu_{r1}}}\overrightarrow{\Psi}^{r}_{E}\right)=\sqrt{\frac{\varepsilon_{r1}}{\mu_{r1}}}\overline{\overline{Z}}_{0}^{-1}\cdot\overrightarrow{\Psi}^{t}_{E} \tag{3.6}$$

Furthermore, the reflection coefficient, R_1, into region 1 from region 2 at $z = 0$ is defined as the ratio of the reflected field to that of the incident field. Also, the transmission coefficient, T_{21}, into region 2 from region 1 is given as the ratio of the transmitted field to the incident field.

$$R_1=\frac{\Psi^{r}_{E}}{\Psi^{i}_{E}} \tag{3.7a}$$

$$T_{21}=\frac{\Psi^{t}_{E}}{\Psi^{i}_{E}} \tag{3.7b}$$

Using (3.7), both (3.5a) and (3.6) can be written in terms of the incident electric field, Ψ^i_E.

$$(1+R_1)\,\Psi^i_E = T_{21}\Psi^i_E \tag{3.8a}$$
$$\frac{1}{\eta_0}\left[\sqrt{\frac{\varepsilon_{r1}}{\mu_{r1}}} - \sqrt{\frac{\varepsilon_{r1}}{\mu_{r1}}}R_1\right]\Psi^i_E = \frac{1}{\eta_0}\sqrt{\frac{\varepsilon_{r1}}{\mu_{r1}}}T_{21}\Psi^i_E \tag{3.8b}$$

Dividing out Ψ^i_E, this becomes two equations and two unknowns for which the reflection and transmission coefficients can now be solved.

$$R_1 = \frac{\eta_{r2} - \eta_{r1}}{\eta_{r2} + \eta_{r1}} \tag{3.9}$$
$$T_{21} = \frac{2\eta_{r2}}{\eta_{r2} + \eta_{r1}} \tag{3.10}$$

Now that the reflection and transmission coefficients have been derived for a plane wave normally incident on the interface between two isotropic materials, this discussion can be extended to multiple interfaces and the method of wave matrices.

3.1.2 Wave Matrix Method

The derivation of wave matrices begins with a description of the problem seen in Figure 3.4. A plane wave is incident from the left in the region $z<0$ with an amplitude of a_1 and another wave with an amplitude of b_2 incident from the right in the region $z>0$. For this analysis, all waves traveling in the positive z-direction will be denoted by a, while the waves traveling in the negative z-direction will be denoted by b. The backward traveling wave in region 1 is comprised of the reflected portion of a_1 and the transmitted portion of b_2 as seen in (3.11a). The same is true of a forward traveling wave in region 2 given by (3.11b).

$$b_1 = R_1 a_1 + T_{12} b_2 \tag{3.11a}$$

$$a_2 = R_2 b_2 + T_{21} a_1 \tag{3.11b}$$

Solving for a_1 in (3.11b) and inserting it in (3.11a), the backward traveling wave in region 1, b_1, can be written terms of the forward and backward traveling waves in region 2. The same can be done to solve for a_1.

$$a_1 = \frac{a_2}{T_{21}} - \frac{R_2 b_2}{T_{21}} \tag{3.12a}$$

$$b_1 = \left(T_{12} - \frac{R_1 R_2}{T_{21}}\right) b_2 + \frac{R_1}{T_{21}} a_2 \tag{3.12b}$$

On the left side of (3.12) are the fields in region 1, while on the right side are the fields in region 2 as well as the reflection and transmission coefficients which are functions of the material properties in both regions. These equations can now be put into matrix format as shown in (3.13).

$$\begin{bmatrix} a_1 \\ b_1 \end{bmatrix} = \frac{1}{T_{21}} \begin{bmatrix} 1 & -R_2 \\ R_1 & T_{21}T_{12} - R_1 R_2 \end{bmatrix} \begin{bmatrix} a_2 \\ b_2 \end{bmatrix} = \begin{bmatrix} A_{11} & A_{21} \\ A_{12} & A_{22} \end{bmatrix} \begin{bmatrix} a_2 \\ b_2 \end{bmatrix} \tag{3.13}$$

The matrix $\overline{\overline{A}}$ shown above is commonly referred to as the wave-transmission chain matrix and it relates the amplitudes of the forward and backward propagating waves in region 1 to those in region 2. Symmetry of the problem under consideration Yields $T_{12} = T_{21}$ and $R_1 = -R_2$ for reflection and transmission on either side of the interface. Remembering also that $T_{21} = 1 + R_1$ and $T_{12} = 1 + R_2$ the elements in $\overline{\overline{A}}$ can be simplified into the following forms,

$$A_{11} = \frac{1}{T_{21}} \quad (3.14a)$$

$$A_{12} = \frac{-R_2}{T_{21}} = \frac{R_1}{T_{21}} \quad (3.14b)$$

$$A_{21} = \frac{R_1}{T_{21}} \quad (3.14c)$$

$$A_{22} = \frac{T_{21}T_{12} - R_1R_2}{T_{21}} = \frac{1}{T_{21}} \quad (3.14d)$$

which can be put back into a simpler matrix form.

$$\begin{bmatrix} a_1 \\ b_1 \end{bmatrix} = \frac{1}{T_{21}} \begin{bmatrix} 1 & R_1 \\ R_1 & 1 \end{bmatrix} \begin{bmatrix} a_2 \\ b_2 \end{bmatrix} \quad (3.15)$$

Once multiple interfaces are incorporated, the length of each region must be taken into consideration since the phase of the waves will change depending on the properties of each region and the distance each wave travels within the regions. This is done by considering first a forward traveling wave a_1e^{-jkz} and then a backward traveling wave b_1e^{jkz}. For z=0, the waves are simply represented by their amplitude coefficients, however the waves at a distance $z = z_1$ from the $z = 0$ plane are given as $a_2 = a_1e^{-jkz_1}$ and $b_2 = b_1e^{jkz_1}$. Finally, relating the waves in region 1 to region 2 gives the following equations where kz_1 is the electric thickness θ_1 as represented in Figure 3.5 which accounts for the phase progression of the wave in that layer.

$$a_1 = a_2e^{jk_zz_1} = a_2e^{j\theta_1} \quad (3.16)$$

$$b_1 = b_2e^{-jk_zz_1} = b_2e^{-j\theta_1} \quad (3.17)$$

This phase relationship can also be put into matrix form.

$$\begin{bmatrix} a_1 \\ b_1 \end{bmatrix} = \begin{bmatrix} e^{j\theta} & 0 \\ 0 & e^{-j\theta} \end{bmatrix} \begin{bmatrix} a_2 \\ b_2 \end{bmatrix} \tag{3.18}$$

Combining both (3.15) and (3.18) both reflection and transmission at a single interface as well as propagation through the layer have been included. Finally, after carrying out the matrix multiplication, (3.20) gives the wave transmission matrix for one layer.

$$\begin{bmatrix} a_1 \\ b_1 \end{bmatrix} = \frac{1}{T_{21}} \begin{bmatrix} 1 & R_1 \\ R_1 & 1 \end{bmatrix} \begin{bmatrix} e^{j\theta} & 0 \\ 0 & e^{-j\theta} \end{bmatrix} \begin{bmatrix} a_2 \\ b_2 \end{bmatrix} \tag{3.19}$$

$$\begin{bmatrix} a_1 \\ b_1 \end{bmatrix} = \frac{1}{T_{21}} \begin{bmatrix} e^{j\theta} & R_1 e^{-j\theta} \\ R_1 e^{j\theta} & e^{-j\theta} \end{bmatrix} \begin{bmatrix} a_2 \\ b_2 \end{bmatrix} \tag{3.20}$$

This gives a straightfoward method for calculating the fields at the $z = 0$ in terms of material properties, layer thickness and the fields at the interface located at $z = z_1$. For the case of an arbitrary number of layers, (3.21) can be formed by cascading each wave transmission matrix until finally having the fields at $z = 0$ in terms of the fields at $z = z_{n+1}$,

$$\begin{bmatrix} a_1 \\ b_1 \end{bmatrix} = \prod_{i=1}^{n} \frac{1}{T_i} \begin{bmatrix} e^{j\theta_i} & R_i e^{-j\theta_i} \\ R_i e^{j\theta_i} & e^{-j\theta_i} \end{bmatrix} \begin{bmatrix} a_{n+1} \\ b_{n+1} \end{bmatrix} \tag{3.21}$$

where T_i and R_i are given by the following equations.

$$R_i = \frac{\eta_i - \eta_{i-1}}{\eta_i + \eta_{i-1}} \tag{3.22}$$

$$T_i = \frac{2\eta_i}{\eta_i + \eta_{i-1}} \tag{3.23}$$

3.1.3 Scattering Matrix

This wave transmission matrix is exceptionally useful because the matrices can simply be cascaded for each additional layer. Another useful property is the ability to convert this final matrix into other useful quantities, such as the scattering matrix, impedance matrix, and admittance matrix [40]. The scattering matrix is of particular interest to this work because it relates the backward traveling waves to the forward traveling waves as seen in (3.24). Besides, scattering parameters are the measured quantity at practice. With the calculated S-parameters, the effective permittivity can be extracted using the same procedure as in section 2.4.3 for the stripline characterization technique.

$$\begin{bmatrix} b_1 \\ b_2 \end{bmatrix} = \begin{bmatrix} S_{11} & S_{12} \\ S_{21} & S_{22} \end{bmatrix} \begin{bmatrix} a_1 \\ a_2 \end{bmatrix} \tag{3.24}$$

The scattering matrix is calculated from the wave matrix using (3.25) [40].

$$\begin{aligned}
S_{11} &= \frac{A_{11} + A_{12}/\eta_0 - A_{21}\eta_0 - A_{22}}{A_{11} + A_{12}/\eta_0 + A_{21}\eta_0 + A_{22}} && \text{(3.25a)}\\
S_{12} &= \frac{2(A_{11}A_{22} - A_{12}A_{21})}{A_{11} + A_{12}/\eta_0 + A_{21}\eta_0 + A_{22}} && \text{(3.25b)}\\
S_{21} &= \frac{2}{A_{11} + A_{12}/\eta_0 + A_{21}\eta_0 + A_{22}} && \text{(3.25c)}\\
S_{22} &= \frac{-A_{11} + A_{12}/\eta_0 - A_{21}\eta_0 + A_{22}}{A_{11} + A_{12}/\eta_0 + A_{21}\eta_0 + A_{22}} && \text{(3.25d)}
\end{aligned}$$

For the two-port network used in this model the wave transmission matrix for each layer can be reduced to the form seen in (3.26) [40].

$$\begin{aligned}
A_{11,i} &= \cos(\theta_i) && \text{(3.26a)}\\
A_{12,i} &= j\eta_0 \sin(\theta_i) && \text{(3.26b)}\\
A_{21,i} &= j\eta_0^{-1} \sin(\theta_i) && \text{(3.26c)}\\
A_{22,i} &= \cos(\theta_i) && \text{(3.26d)}
\end{aligned}$$

3.2 Analysis and Results

Using the methods described in the previous section, the effective permittivity of a composite comprised of layered dielectrics is investigated. More specifically, the composition consists of two dissimilar dielectrics with differing relative permittivities alternating such that the first layer is the same as the final layer. This last requirement allows the system to be symmetric, a necessity of the inversion method used herein.

As the number of layers is increased the total volume of the mixture being simulated is held constant, as is the volume of each of the two dielectrics. Therefore, different volume fractions, dielectric contrast ratios and number of layers will be analyzed in order to interpret their consequence on the effective permittivity of the composite. The fixed thickness of the composite being simulated is $\lambda/50$ and is sufficiently small enough to realize homogenization.

Figure 3.6 gives the effective permittivity for the first case in which the volume fraction of dielectric A is 0.75 and has the lower value of permittivity. As seen in Figure 3.2, the scattering parameters are calculated when dielectric A is on the outside (e.g., facing the impinging waves), then again when dielectric B is on the outside. For the situation when dielectric A is on the outside, the effective permittivity is seen to start at a lower value and begin to rise as the number of layers is increased and eventually saturate to the dashed line calculated using the linear law which is discussed below. The later situation when dielectric B is the outer later results in the effective permittivity beginning at a higher value and lowering to the same dashed line. For all cases in which layer A has the lower permittivity in the dielectric contrast ratio, this trend is repeated. Figure 3.7 is the same analysis as in the previous case, however the volume fraction of material A is 0.5, and finally Figure 3.8 illustrates the same effects with the volume fraction of material A equal to 0.25. In each of these cases, six different dielectric contrast ratios are calculated ranging from $1:4$ up to $1:49$.

As mentioned earlier, the dashed lines in each figure are calculated using the linear law by (3.27). This is the simplest formula for determining the effective permittivity of a two-phase mixture where subscript A implies dielectric A, and subscript B implies dielectric B, while the volume fraction of material A is denoted by f_A, etc.

$$\varepsilon_{eff} = f_A\varepsilon_A + f_B\varepsilon_B \tag{3.27}$$

This straightforward equation assumes total homogenization and the effective permittivity is purely a function of the dielectric constants and their volume fractions.

Whether the outer layer is the high or low dielectric contrast the effective permittivity will eventually merge towards the value given by (3.27) as the number or layers is increased. This implies that the effects of the layering is negligible once the layers become extremely thin. Figure 3.6 shows that the effective permittivity can be tuned to any value between 1.65 and 16.6, and Figure 3.8 yields an effective permittivity range from 2.38 to 48.6. Table 3.1 summarizes these ranges for each of the dielectric contrast ratios and volume fractions. These results allow for a potential design platform for planar layered composites, and demonstrate how the different number of layers within a composite can be used to control or tune the effective permittivity to better fit some particular electromagnetic application. A possible reason for the change in permittivity as the number of layers is altered is due to multiple reflections within the composite. A material with multiple interfaces has the potential to trap more power and hence have a greater effective permittivity at the outer edges. Or perhaps a composite material can be designed with a certain number of layers as to allow for greater propagation through the material or to reduce trapped power and lower the effective permittivity. The analysis performed in this chapter for lossless dielectric composites based on contrast ratios and volume fractions has demonstrated the effects of layering. However, in real-world applications the materials being used will have some form of loss associated with the permittivity, permeability or both. Just as the number of layers and multiple reflections can help control the effective permittivity, they can also effect the loss of the composite. As a wave propagates through a lossy material and is bounced back and forth, the wave will have greater attenuation after traveling through the entire composite. This results in a greater negative imaginary portion of permittivity. Now that the effects of layering are better understood, it is imparative that the model be extended to include layers of actual materials since many magnetic materials have a tensor permeability and the goal is ultimately to design and control a composite's permittivity and permeability. This is done in Chapter 4 and includes loss in the analysis.

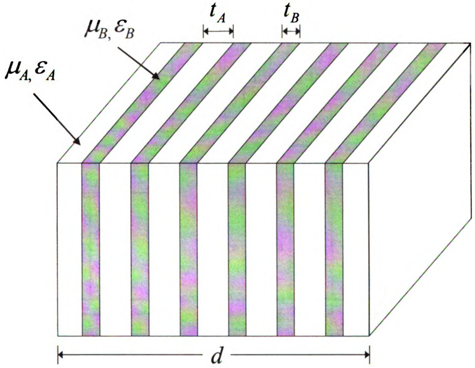

Figure 3.1. Geometry for layered materials.

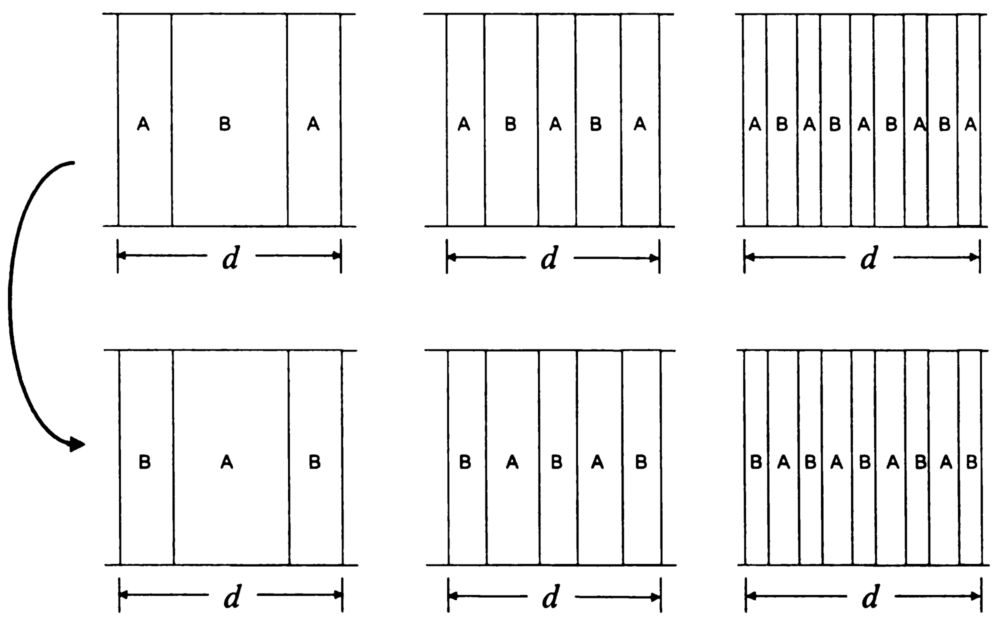

Figure 3.2. Illustration of the analysis on layered materials when layers A and B are swapped.

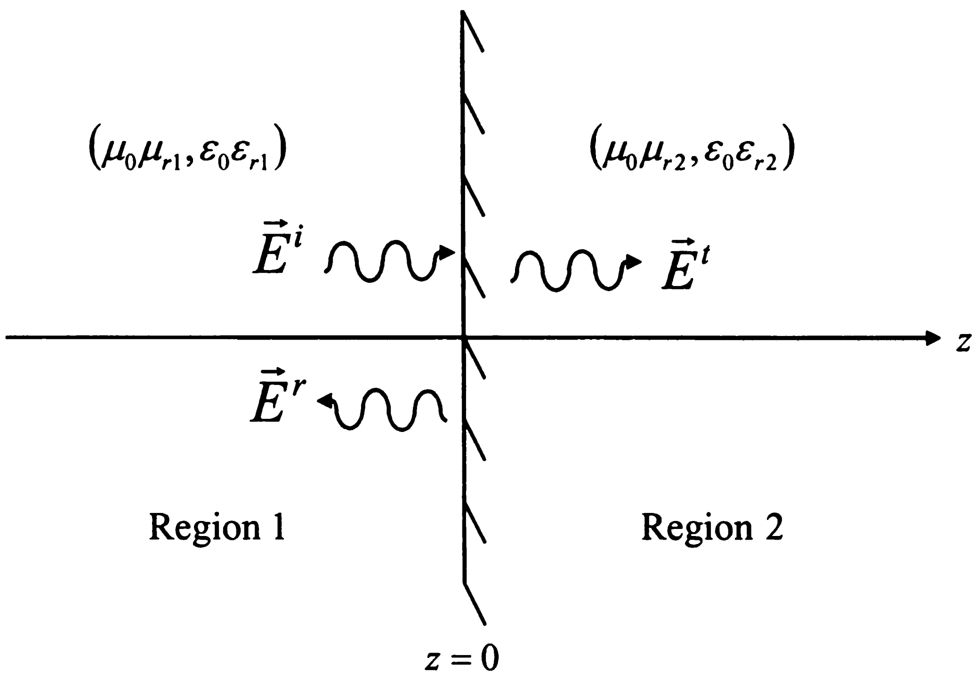

Figure 3.3. Incident, reflected, and transmitted waves for an interface between 2 isotropic materials.

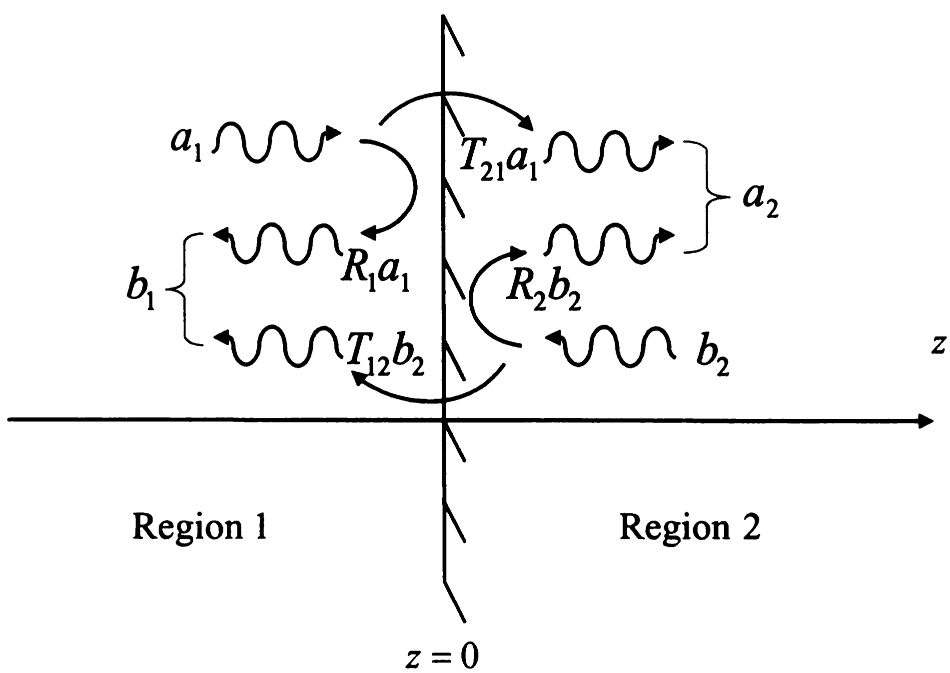

Figure 3.4. Reflection and transmission of plane wave amplitude coefficients.

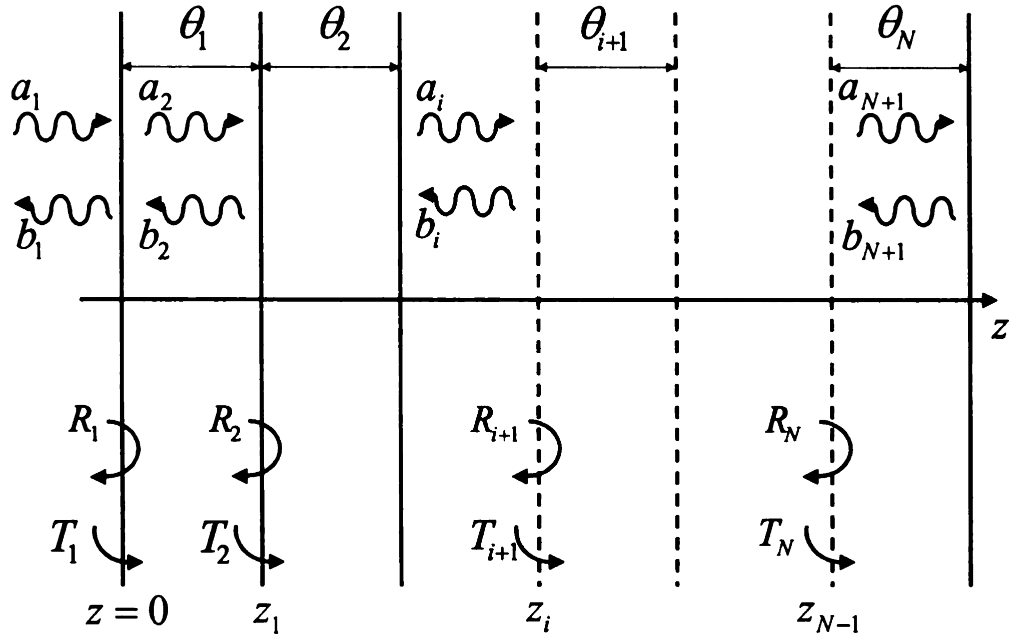

Figure 3.5. Reflection and transmission of plane wave amplitude coefficients for multiple layers.

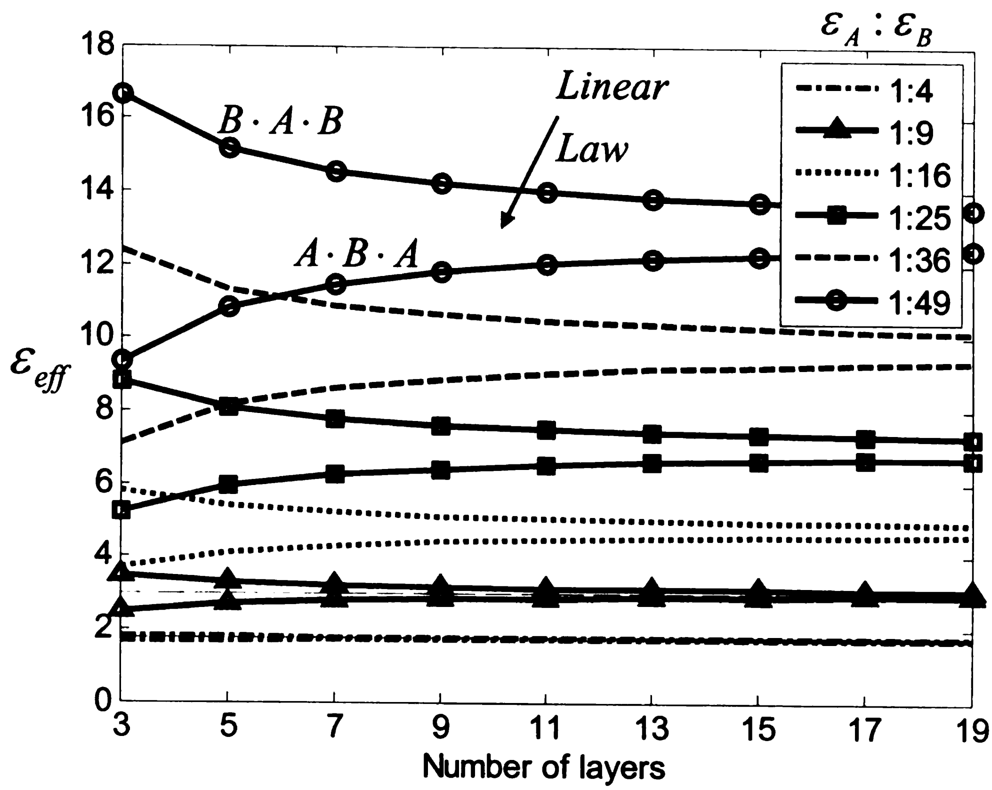

Figure 3.6. Case 1: Layer A has volume fraction 0.75.

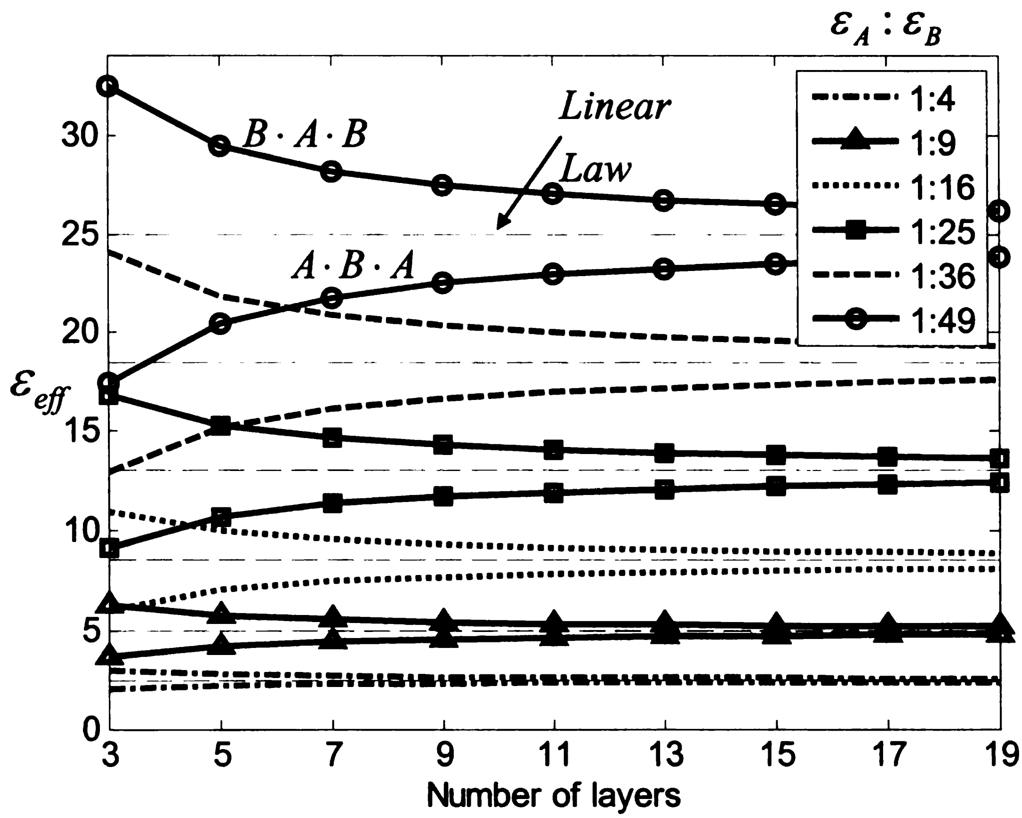

Figure 3.7. Case 2: Layer A has volume fraction 0.50.

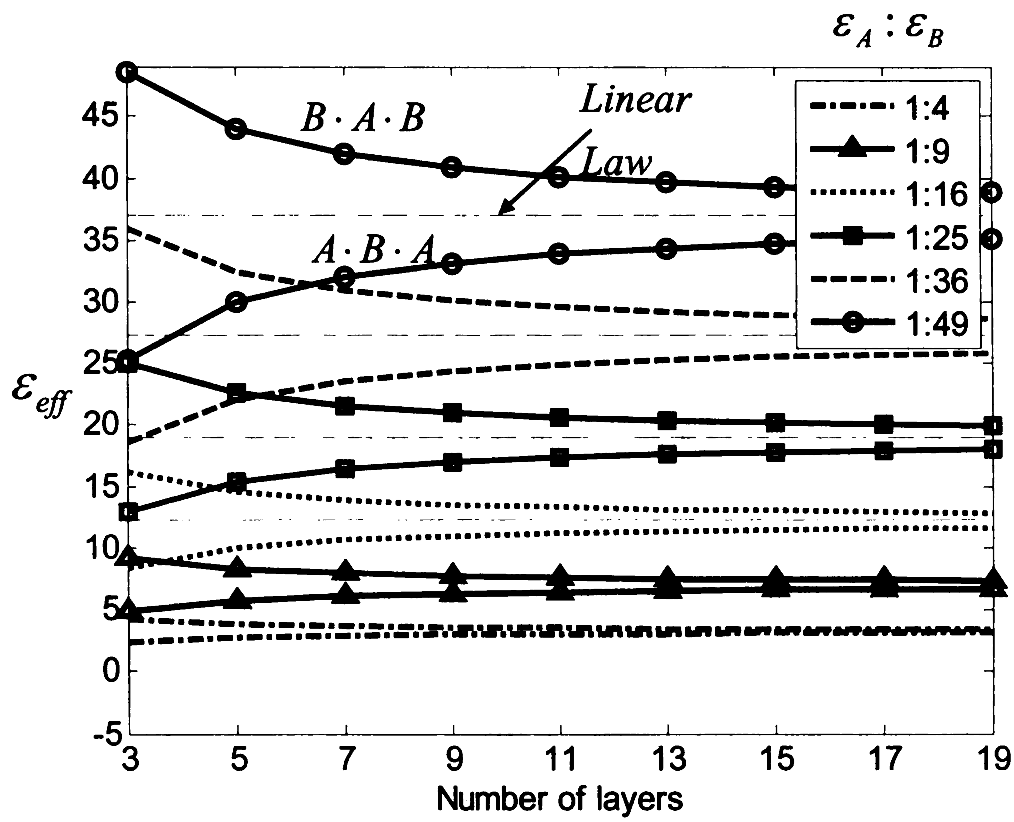

Figure 3.8. Case 3: Layer A has volume fraction 0.25.

	Dielectric Contrast Ratio						
f_A	1:4	1:9	1:16	1:25	1:36	1:49	Total
0.75	1.65-1.82	2.5-3.5	3.7-5.8	5.2-8.8	7.1-12.4	9.4-16.6	1.65-16.6
0.5	2-3	3.7-6.3	6.05-10.95	9.1-16.9	12.95-24	17.5-32.5	2-32.5
0.25	2.38-4.2	4.85-9.1	8.4-16.1	13-25	18.65-35.8	25.4-48.6	2.38-48.6

Table 3.1. Tunable Effective Permittivity range summary for isotropic layered composites.

CHAPTER 4

ANISOTROPIC LAYERED COMPOSITES

The purpose of this chapter is to demonstrate a method of calculating the scattering parameters of a planar, layered, *anisotropic* composite material. From these S-parameters, the complex effective permittivity and permeability of the mixture is extracted using a complex 2D Newton's root searching algorithm as in section 2.4.3. The S-parameters are calculated at the front and back interfaces of the layered composite in order to effectively homogenize the composite. This is accomplished using state vector and state equation formulations stemming from Maxwell's equations [41, 42]. In Chapter 3 the scattering parameters for isotropic dielectric layers were determined using the method of wave matrices. This demonstrated how the number of layers, as well as the volume fractions and dielectric constants of each layer, could be manipulated in order to achieve an effective permittivity that better suits the application. Also, the greater the dielectric contrast ratio, the wider the range of tunable effective permittivities will be accomplished.

In this chapter, the layered composite model is extended to include anisotropic layers such as ferrimagnetic materials which can be comprised of ferrites or magnetic garnets, for example. The objective is to design a layered mixture that exhibits magnetic behavior and achieve a tunable permeability. Ferrites are chosen because unlike ferromagnetic compounds, ferrites or ferrimagnetic materials do not have high resistivity but has anisotropy induced by an external applied field [38]. In ferrimagnetics, the individual elements of the permeability tensor can be controlled using a static magnetic bias field (e.g., the field from a permanent magnet) [40]. The derivation of the reflection and transmission coefficients are introduced as well as various examples including: narrow line-width ferrimagnetic composites, wide line-width ferrimagnetic composites, and double negative materials.

4.1 Background and Derivation

4.1.1 Geometry

The geometry of the composite in this derivation is given by Figure 4.1. Just as in chapter 3, the material extends to infinity in the x and y directions with a finite thicknes in z. The configuration consists of three regions where region 2 contains the anisotropy in the permeability tensor, permittivity tensor, or both. In all but one case in this chapter, both regions 1 and 3 are considered to be free space. The interface between regions 1 and 2 is located at $z = 0$ and between regions 2 and 3 at $z = d$. First, the reflection and transmission from an anisotropic slab is derived. Next, the slab is partitioned into layers such that the fields at the $n-1$ interface will be calculated in terms of the fields at the n interface. Finally, this is continued until the fields at the $z = 0$ interface are known in terms of the fields at the $z = d$ interface as seen in the preceeding chapter.

4.1.2 State Vector and State Equation Formulation

To start, the two bulk Maxwell's equations, more specifically the two curl equations, Faraday's law and Ampere's law, will be separated into their six different components where both permittivity and permeability are rank 2 tensors. The notation used to represent a rank 2 tensor, or matrix, will be square brackets. A rank 1 tensor, or column vector, will be denoted by curly braces. Spatial vectors will remain using the over-right-arrow notation.

$$\nabla \times \overrightarrow{E} = -j\omega[\mu]\cdot \overrightarrow{H} \tag{4.1a}$$

$$\begin{bmatrix} \delta_y E_z - \delta_z E_y \\ \delta_z E_x - \delta_x E_z \\ \delta_x E_y - \delta_y E_x \end{bmatrix} = -j\omega \begin{bmatrix} \mu_{xx} & \mu_{xy} & \mu_{xz} \\ \mu_{yx} & \mu_{yy} & \mu_{yz} \\ \mu_{zx} & \mu_{zy} & \mu_{zz} \end{bmatrix} \begin{bmatrix} H_x \\ H_y \\ H_z \end{bmatrix} \tag{4.1b}$$

$$
\begin{aligned}
\nabla \times \overrightarrow{H} &= j\omega[\varepsilon]\cdot \overrightarrow{E} && (4.2a)\\
\begin{bmatrix} \delta_y H_z - \delta_z H_y \\ \delta_z H_x - \delta_x H_z \\ \delta_x H_y - \delta_y H_x \end{bmatrix} &= j\omega \begin{bmatrix} \varepsilon_{xx} & \varepsilon_{xy} & \varepsilon_{xz} \\ \varepsilon_{yx} & \varepsilon_{yy} & \varepsilon_{yz} \\ \varepsilon_{zx} & \varepsilon_{zy} & \varepsilon_{zz} \end{bmatrix} \begin{bmatrix} E_x \\ E_y \\ E_z \end{bmatrix} && (4.2b)
\end{aligned}
$$

These equations can be separated into transverse, (4.3),(4.4), and longitudinal components (4.5).

$$
\begin{aligned}
\delta_z E_x &= -j\omega\left(\mu_{yx} H_x + \mu_{yy} H_y\right) - j\omega\mu_{yz} H_z + \delta_x E_z && (4.3a)\\
\delta_z E_y &= j\omega\left(\mu_{xx} H_x + \mu_{xy} H_y\right) + j\omega\mu_{xz} H_z + \delta_y E_z && (4.3b)
\end{aligned}
$$

In (4.3), the left side of the equation has the normal derivatives of the transverse electric fields and the right side contains all three components of the magnetic field along with the transverse derivatives of the longitudinal components of the electric field. The same is true of (4.4), except the magnetic and electric fields are transposed.

$$
\begin{aligned}
\delta_z H_x &= j\omega\left(\varepsilon_{yx} E_x + \varepsilon_{yy} E_y\right) + j\omega\varepsilon_{yz} E_z + \delta_x H_z && (4.4a)\\
\delta_z H_y &= -j\omega\left(\varepsilon_{xx} E_x + \varepsilon_{xy} E_y\right) - j\omega\varepsilon_{xz} E_z + \delta_y H_z && (4.4b)
\end{aligned}
$$

Finally, the longitudinal fields in (4.5) can be inserted into both (4.3) and (4.4) reducing the six components of Maxwell's equations into four components in terms of the transverse electric and magnetic fields only.

$$
\begin{aligned}
H_z &= \frac{-1}{j\omega\mu_{zz}}\left(\delta_x E_y - \delta_y E_x\right) - \frac{1}{\mu_{zz}}\left(\mu_{zx} H_x + \mu_{zy} H_y\right) && (4.5a)\\
E_z &= \frac{1}{j\omega\varepsilon_{zz}}\left(\delta_x H_y - \delta_y H_x\right) - \frac{1}{\varepsilon_{zz}}\left(\varepsilon_{zx} E_x + \varepsilon_{zy} E_y\right) && (4.5b)
\end{aligned}
$$

The transverse electric field, $\overrightarrow{E}_t(\overrightarrow{r}) = E_x(\overrightarrow{r})\hat{x} + E_y(\overrightarrow{r})\hat{y}$, and transverse magnetic field, $\overrightarrow{H}_t(\overrightarrow{r}) = H_x(\overrightarrow{r})\hat{x} + H_y(\overrightarrow{r})\hat{y}$, can be represented in a form in which the x, y and z dependences are separated.

$$\overrightarrow{E_t} = \overrightarrow{E_t}(z)e^{-jk_x x - jk_y y} \tag{4.6a}$$

$$\overrightarrow{H_t} = \overrightarrow{H_t}(z)e^{-jk_x x - jk_y y} \tag{4.6b}$$

The reprersentation given by (4.6), illustrates how the dependence in the x and y directions allows phase matching to be achieved at the interfaces and implies that the transverse fields depend on their position in z. Now (4.3) and (4.4) can be put into the matrix form seen in (4.7).

$$\frac{d}{dz}\left\{\begin{array}{c} \overrightarrow{E_t} \\ \overrightarrow{H_t} \end{array}\right\} = [A]\cdot\left\{\begin{array}{c} \overrightarrow{E_t} \\ \overrightarrow{H_t} \end{array}\right\} \tag{4.7}$$

This is called the state equation where the matrix $[A]$ is a 4x4 matrix containing the operations on the transverse components of the fields. The column vector containing the longitudinal dependence of the transverse fields can be represented by the state vector, $\{V\}$, in (4.8).

$$\{V\} = \begin{bmatrix} E_x(z) \\ E_y(z) \\ H_x(z) \\ H_y(z) \end{bmatrix} \tag{4.8}$$

The state equation can now be represented in its compact form given by (4.9).

$$\frac{d}{dz}\{V\} = [A]\cdot\{V\} \tag{4.9}$$

The z dependence from the column vector in (4.8) can be separated out and represented by (4.10).

$$\{V\} = \{\Psi\} e^{\lambda z} = \begin{bmatrix} E_{x0} \\ E_{y0} \\ H_{x0} \\ H_{y0} \end{bmatrix} e^{\lambda z} \tag{4.10}$$

Now the z derivative from the state equation in (4.9) can be replaced by λ which yields the eigenvalue equation in (4.11) where $[I]$ is the identity matrix.

$$([A] - \lambda [I]) \cdot \{\Psi\} = 0 \tag{4.11}$$

The calculated eigenvalue in the representation of $\{V\}$ in (4.10) denotes the propagation phase and attenuation of a plane wave through region 2. The elements in $[A]$ are given by (4.12) in its most general form. It should be noted that in this analysis, the plane wave is assumed to have normal incidence upon the layered composite, this implies that k_x and k_y in (4.12) are zero reducing the complexity of $[A]$. This eigenvalue equation will solve for the fields in an anisotropic region assuming plane wave propagation. The next section derives a solution for the fields at the interfaces of an anisotropic slab of thickness *d*. This method is similar to the wave matrix method in chapter 3 because each layer within region 2 will have a solved matrix that can be cascaded to the solved matrices of the other layers. A non-trivial solution to (4.11) can be obtained by setting the determinant $det\,([A] - \lambda [I])$ equal to zero and solving the resulting characteristic polynomial of $[A]$, for the unknown eigenvalues λ. Once the eigenvalues are determined, they can be used in (4.11) to find the corresponding eigenvectors.

$$
\begin{aligned}
A_{11} &= \frac{jk_y\mu_{yz}}{\mu_{zz}} + \frac{jk_x\varepsilon_{zx}}{\varepsilon_{zz}} && \text{(4.12a)}\\
A_{12} &= \frac{-jk_y\mu_{yz}}{\mu_{zz}} + \frac{jk_x\varepsilon_{xy}}{\varepsilon_{zz}} && \text{(4.12b)}\\
A_{13} &= -j\omega\mu_{yx} + \frac{j\omega\mu_{yz}\mu_{xz}}{\mu_{zz}} - \frac{jk_xk_y}{\omega\varepsilon_{zz}} && \text{(4.12c)}\\
A_{14} &= -j\omega\mu_{yy} + \frac{j\omega\mu_{yz}\mu_{zy}}{\mu_{zz}} + \frac{jk_x^2}{\omega\varepsilon_{zz}} && \text{(4.12d)}\\
A_{21} &= \frac{-jk_y\mu_{xz}}{\mu_{zz}} + \frac{jk_y\varepsilon_{zx}}{\varepsilon_{zz}} && \text{(4.12e)}\\
A_{22} &= \frac{jk_x\mu_{xz}}{\mu_{zz}} + \frac{jk_y\varepsilon_{zy}}{\varepsilon_{zz}} && \text{(4.12f)}\\
A_{23} &= j\omega\mu_{xx} - \frac{j\omega\mu_{xz}\mu_{zx}}{\mu_{zz}} - \frac{jk_y^2}{\omega\varepsilon_{zz}} && \text{(4.12g)}\\
A_{24} &= j\omega\mu_{xy} - \frac{j\omega\mu_{xz}\mu_{zy}}{\mu_{zz}} - \frac{jk_yk_x}{\omega\varepsilon_{zz}} && \text{(4.12h)}\\
A_{31} &= j\omega\varepsilon_{yx} - \frac{j\omega\varepsilon_{yz}\varepsilon_{zx}}{\varepsilon_{zz}} + \frac{jk_xk_y}{\omega\mu_{zz}} && \text{(4.12i)}\\
A_{32} &= j\omega\varepsilon_{yy} - \frac{j\omega\varepsilon_{yz}\varepsilon_{zy}}{\varepsilon_{zz}} - \frac{jk_x^2}{\omega\mu_{zz}} && \text{(4.12j)}\\
A_{33} &= \frac{jk_y\varepsilon_{yz}}{\varepsilon_{zz}} + \frac{jk_x\mu_{zx}}{\mu_{zz}} && \text{(4.12k)}\\
A_{34} &= \frac{-jk_x\varepsilon_{yz}}{\varepsilon_{zz}} + \frac{jk_x\mu_{xy}}{\mu_{zz}} && \text{(4.12l)}\\
A_{41} &= -j\omega\varepsilon_{xx} + \frac{j\omega\varepsilon_{xz}\varepsilon_{zx}}{\varepsilon_{zz}} + \frac{jk_y^2}{\omega\mu_{zz}} && \text{(4.12m)}\\
A_{42} &= -j\varepsilon_{xy} + \frac{j\omega\varepsilon_{xz}\varepsilon_{zy}}{\varepsilon_{zz}} - \frac{jk_yk_x}{\omega\mu_{zz}} && \text{(4.12n)}\\
A_{43} &= \frac{-jk_y\varepsilon_{xz}}{\varepsilon_{zz}} + \frac{jk_y\mu_{zx}}{\mu_{zz}} && \text{(4.12o)}\\
A_{44} &= \frac{jk_x\varepsilon_{xz}}{\varepsilon_{zz}} + \frac{jk_y\mu_{zy}}{\mu_{zz}} && \text{(4.12p)}
\end{aligned}
$$

4.1.3 Transition, Transmission, and Reflection Matrices

The transition matrix is used to describe the relationship between the fields at the $z = 0$ interface to the fields at the $z = d$ interface as illustrated in Figure 4.1a. This matrix is used to describe the transition of the fields through region 2 in terms of material properties and layer thickness. The transition matrix, $[B]$ is given in mathematical form by (4.13)

$$\{V(z = 0)\} = [B] \cdot \{V(z = d)\} \tag{4.13}$$

and is a 4x4 matrix with 2x2 submatrices given by $[b]$ in (4.14).

$$[B] = \begin{bmatrix} [b_1] & [b_2] \\ [b_3] & [b_4] \end{bmatrix} \tag{4.14}$$

Also, the reflected and transmitted electric fields can be represented by (4.15) which introduces 2x2 reflection and transmission matrices for the fields at the interfaces $z = 0$ and $z = d$.

$$\overrightarrow{E_t^r}(0) = [R] \cdot \overrightarrow{E_t^i}(0) \tag{4.15a}$$

$$\overrightarrow{E_t^t}(d) = [T] \cdot \overrightarrow{E_t^i}(0) \tag{4.15b}$$

The subscript "t" implies that these are the transverse fields in the x and y directions, while the superscripts "r", "i", and "t" represent the reflected, incident, and transmitted fields, respectively. The total field in region 1 are given by the superposition of the incident and reflected fields while the total field in region 3 consist of the transmitted field only. Therefore the transition matrix equation given in (4.13) can be written by (4.17).

$$\overrightarrow{E_t^i} + \overrightarrow{E_t^r} = \overrightarrow{E_t^{tot}}(z \leq 0) \tag{4.16a}$$

$$\overrightarrow{E_t^t} = \overrightarrow{E_t^{tot}}(z \geq d) \tag{4.16b}$$

$$\overrightarrow{H_t^i} + \overrightarrow{H_t^r} = \overrightarrow{H_t^{tot}}(z \leq 0) \tag{4.16c}$$

$$\overrightarrow{H_t^t} = \overrightarrow{H_t^{tot}}(z \geq d) \tag{4.16d}$$

$$\begin{bmatrix} E_x^{i+r}(0) \\ E_y^{i+r}(0) \\ H_x^{i+r}(0) \\ H_y^{i+r}(0) \end{bmatrix} = \begin{bmatrix} [b_1] & [b_2] \\ [b_3] & [b_4] \end{bmatrix} \begin{bmatrix} E_x^t(d) \\ E_y^t(d) \\ H_x^t(d) \\ H_y^t(d) \end{bmatrix} \tag{4.17}$$

This can be multiplied out of matrix form to give the following two equations for the electric and magnetic fields.

$$\overrightarrow{E_t^i}(0) + \overrightarrow{E_t^r}(0) = [b_1] \cdot \overrightarrow{E_t^t}(d) + [b_2] \cdot \overrightarrow{H_t^t}(d) \tag{4.18}$$

$$\overrightarrow{H_t^i}(0) + \overrightarrow{H_t^r}(0) = [b_3] \cdot \overrightarrow{E_t^t}(d) + [b_4] \cdot \overrightarrow{H_t^t}(d) \tag{4.19}$$

In order to reduce the number of unknowns in the above equations, the transverse magnetic fields are represented in terms of the corresponding transverse electric field components through wave impedance matrices.

$$\overrightarrow{E_t^i}(0) = [Z_1] \cdot \overrightarrow{H_t^i}(0) \tag{4.20a}$$

$$\overrightarrow{E_t^r}(0) = -[Z_1] \cdot \overrightarrow{H_t^i}(0) \tag{4.20b}$$

$$\overrightarrow{E_t^t}(d) = [Z_3] \cdot \overrightarrow{H_t^t}(d) \tag{4.20c}$$

$$\left[Z_{1,3}\right] = \begin{bmatrix} 0 & \eta_{1,3} \\ -\eta_{1,3} & 0 \end{bmatrix} \tag{4.21a}$$

$$\eta_{1,3} = \sqrt{\frac{\mu_{1,3}}{\varepsilon_{1,3}}} \tag{4.21b}$$

The wave impedances, $\eta_{1,3}$, are functions of both permittivity and permeability of regions 1 or 3. Using (4.15) and the above impedance matrices, (4.18) can be written entirely in terms of the incident electric field. The incident field term can be normalized allowing for the solution of the reflection matrix in terms of the transmission, transition, and impedance matrices.

$$\overrightarrow{E_t^i}(0) + [R] \cdot \overrightarrow{E_t^i}(0) = [b_1] \cdot [T] \cdot \overrightarrow{E_t^i}(0) + [b_2] \cdot \left[Z_3^{-1}\right] \cdot [T] \cdot \overrightarrow{E_t^i}(0) \tag{4.22a}$$

$$[R] = [b_1] \cdot [T] + [b_2] \cdot \left[Z_3^{-1}\right] \cdot [T] - [I] \tag{4.22b}$$

The same procedure can be aplied to (4.19). Once the incident electric field term has been normalized, the reflection matrix from above can be inserted leaving only the transmission matrix as the unknown.

$$\overrightarrow{E_t^i}(0) \cdot [Z_1]^{-1} - [R] \cdot \overrightarrow{E_t^i}(0) \cdot [Z_1]^{-1} = [b_3] \cdot [T] \cdot \overrightarrow{E_t^i}(0) + [b_4] \cdot [T] \cdot \overrightarrow{E_t^i}(0) \cdot [Z_3]^{-1} \tag{4.23}$$

$$[T] \cdot \left([b_3] + [b_4] \cdot [Z_3]^{-1}\right) = \left([Z_1]^{-1} - \left([b_1] \cdot [T] + [b_2] \cdot [Z_3]^{-1} \cdot [T] - [I]\right) \cdot [Z_1]^{-1}\right) \tag{4.24}$$

The transmission matrix is given in terms of the impedance and transition matrices in (4.25).

$$[T] = 2\,[Z_3] \cdot ([b_1] \cdot [Z_3] + [b_2] + [b_3] \cdot [Z_1] \cdot [Z_3] + [b_4] \cdot [Z_1])^{-1} \tag{4.25}$$

This transmission matrix is then inserted into the equation for the reflection matrix in (4.22b).

$$
\begin{aligned}
[R] =&([b_1] + [b_2] \cdot [Z_3]^{-1}) \cdot 2\,[Z_3] \\
&\cdot ([b_1] \cdot [Z_3] + [b_2] + [b_3] \cdot [Z_1] \cdot [Z_3] + [b_4] \cdot [Z_1])^{-1} - [I]
\end{aligned}
$$

Finally, the reflection matrix is given by the following equation in terms of impedance and transition matrices.

$$
\begin{aligned}
[R] =&([b_1] \cdot [Z_3] + [b_2] + [b_3] \cdot [Z_1] \cdot [Z_3] + [b_4] \cdot [Z_1]) \\
&\cdot ([b_1] \cdot [Z_3] + [b_2] + [b_3] \cdot [Z_1] \cdot [Z_3] + [b_4] \cdot [Z_1])^{-1}
\end{aligned}
$$

These reflection and transmission matrices have been derived for a homogeneous slab of anisotropic material as shown in Figure 4.1a, and are functions of impedance matrices which describe the isotropic surrounding regions and the transition matrix which describes the slab.

4.1.4 Layered Media and Local Transition Matrix

Reflection and transmission have now been derived for an anisotropic slab in terms of impedance and transition matrices for which the latter has yet to be solved. The transition matrix represents the propagation inside region 2 between interfaces at $z = 0$ and $z = d$. In this section, region 2 is no longer an anisotropic slab, but a layered anisotropic material. Therefore a local transition matrix, $[B_n]$ is introduced, which represents the fields at the interface $z = z_{n-1}$ to the fields at $z = z_n$ within region 2 where those interfaces surround the n^{th} layer. This is illustrated in Figure 4.1b and mathematically given by (4.26).

$$
\{V_{n-1}\} = [B]_n \cdot \{V_n\} \tag{4.26}
$$

This implies that the eigenvalue equation derived in section 4.1.2 will need to be solved in each individual n^{th} layer.

$$([A_n] - \lambda_n[I]) \cdot \{\Psi_n\} = 0 \tag{4.27}$$

Once the eigenvalues, λ_n, and corresponding eigenvectors, $\{\Psi_n\}$, are known for each layer the state vector is also known and given by the following representation with coefficients $\{C_n\}$.

$$\{V_n\} = \{\Psi_n\} \cdot e^{[\lambda_n]z} \cdot \{C_n\} = \{\Psi_n\} \cdot f\left([D\left(z_n\right)]\right) \cdot \{C_n\} \tag{4.28}$$

$$f\left([D_n\left(z_n\right)]\right) = \begin{bmatrix} e^{\lambda_1 z_n} & 0 & 0 & 0 \\ 0 & e^{\lambda_2 z_n} & 0 & 0 \\ 0 & 0 & e^{\lambda_3 z_n} & 0 \\ 0 & 0 & 0 & e^{\lambda_4 z_n} \end{bmatrix} \tag{4.29}$$

The function $f\left([D(z_n)]\right)$ is an exponential function of the diagonal eigenvalue matrix above and has the property below.

$$f\left(\left[D_n\left(z_{n-1} + z_n\right)\right]\right) = f\left(\left[D_n\left(z_{n-1}\right)\right]\right) \cdot f\left([D_n\left(z_n\right)]\right) \tag{4.30}$$

Using this relationship, the fields at the interface $z = z_{n-1}$ can be written by (4.31).

$$\left\{V_{n-1}\right\} = \{\Psi_n\} \cdot f\left(\left[D_n\left(z_{n-1} - z_n\right)\right]\right) \cdot \left\{\Psi_n^{-1}\right\} \cdot \{\Psi_n\} \cdot f\left([D_n\left(z_n\right)]\right) \cdot \{C_n\} \tag{4.31}$$

Utilizing (4.28) for $\{V_n\}$ into (4.31) for $\left\{V_{n-1}\right\}$ and comparing to (4.26), an expression for the local transition matrix is obtained.

$$[B_n] = \{\Psi_n\} \cdot f\left(\left[D_n\left(z_{n-1} - z_n\right)\right]\right) \cdot \{\Psi_n\}^{-1} \tag{4.32}$$

Once all of the local transition matrices have been solved for each layer, they can be cascaded together in order to obtain the total transition matrix which relates the fields at the $z = 0$ interface to those at the $z = d$ interface and accounts for the interaction of the fields within the anisotropic region.

$$[B] = \prod_{n=1}^{N} [B_n] \tag{4.33}$$

where N denotes the number of layers. Using the total transition matrix and the impedance matrices for the surrounding regions, both reflection and transmission can be calculated and used to extract the complex permittivity and permeability of the layered composite as done in section 2.4.3.

4.2 Verification of Anisotropic Formulation

The solution presented here for reflection and transmission from a planar anisotropic material is an analytical solution. However it is still useful to check the computer program for errors either in the formulation or in the coding process. The following three cases will verify the code and solution by comparison to propagation through free space, reflection from PEC, and scattering from an iostrpic layered composite by which it can be compared to the code from chapter 3.

4.2.1 Transmission through Free Space

The first check of the layered anisotropic formulation will be computed for the case shown in Figure 4.2 where regions 1, 2, and 3 are all free space. Therefore $\mu_i = \mu_0$ and $\varepsilon_i = \varepsilon_0$ for i=1, 2, or 3. As seen in Figure 4.3a the result is that the magnitude of $|S_{11}|$ is 0 and $|S_{21}|$ is 1, which implies total transmission as expected for free space. Phase for S_{21} at z=d is given in Figure 4.2b and demonstrates phase wrap-around occuring at 6GHz. This observation will become useful for verifcation in the following case.

4.2.2 Reflection from PEC space

The next check is performed for free space in regions 1 and 2 and perfect electric conductor (PEC) in region 3 as seen in Figure 4.4. The magnitude of the scattering parameters is shown in Figure 4.5a and illustrates total reflection, $|S_{11}| = 1$ and $|S_{21}| = 0$ as expected from PEC. Also, Figure 4.5b shows the phase of S_{11} at $z = 0$ after the wave has traveled to $z = d$ and back again. Phase wrap around occurs at 3GHz which is half the frequency location for the phase of S_{21} in the previous section for the case of free space. As distance traveled is increased, the phase will take on steeper slopes. In this situation, the wave has traveled twice the distance to get from the PEC and back as opposed to the previous case and hence the slope of S_{11} is twice as steep as for S_{21} in free space and therefore wrap-around occurse at half the frequency. This helps to further verify that the code and formulation are working properly.

4.2.3 Comparison with Isotropic Layers

The final check in the verification process is to simulate a composite of layered isotropic materials and compare the results to the same simulation using the wave matrix method described in chapter 3. The composite has 15 layers with alternating A and B materials each having a thickness of $100\mu m$. Material A has properties of free space while material B is non-magnetic ($\mu_r = 1$) with relative permittivity of 25. Figure 4.6 shows the magnitude and phase of the scattering parameters for both the isotropic and anisotropic analysis methods, while Figure 4.7 illustrates the extracted permittivity and permeability values. Both methods yield the same values for S-parameters and constitutive parameters providing further verification of the anisotropic formulation.

4.3 Ferrimagnetic Materials with Anisotropic Permeability

4.3.1 Permeability Tensor

The purpose for including anisotropic layers is to include ferrimagnetic materials in order to tune the effective permeability as well as permittivity. Narrow line-width ferrites provide a good low-loss magnetic material for which the anisotropy and permeability tensor elements can be controlled using a bias magnetic field. The permeability tensor is given by (4.34) for a bias field in the x-direction [40].

$$[\mu] = \begin{bmatrix} \mu_0 & 0 & 0 \\ 0 & \mu & j\kappa \\ 0 & -j\kappa & \mu \end{bmatrix} \qquad \hat{x} - bias \tag{4.34}$$

The elements in the permeability tensor are calculated by (4.35) where $\omega = 2\pi f$ is the operating frequency and $\mu_0 = 4\pi \times 10^{-7}$ is the permeability of free space.

$$\mu = \mu_0 \left(1 + \frac{\omega_0 \omega_m}{\omega_0^2 - \omega^2}\right) \tag{4.35a}$$

$$\kappa = \mu_0 \frac{\omega \omega_m}{\omega_0^2 - \omega^2} \tag{4.35b}$$

Also, $\omega_0 = \mu_0 \gamma H_0$ and $\omega_m = \mu_0 \gamma M_s$ where H_0 is the strength of the internal bias field in oersteds and $M_s = 4\pi M_s$ is the saturation magnetization in gauss. The ratio of the spin magnetic moment to the spin angular momentum for an electron is called the gyromagnetic ratio and is given by $\gamma = 1.759 \times 10^{11}\ C/Kg$ [40]. The larmor frequency can be calculated by $f_0 = \omega_0/2\pi = (2.8MHz/oersted)(H_0\ oersted)$ and $f_m = \omega_m/2\pi = (2.8MHz/oersted)(4\pi M_s\ gauss)$. One more thing to include in the calculation of larmor frequency is the linewidth, ΔH in order to account for magnetic losses inherent in magnetic materials. This is done by using (4.36), giving a complex valued larmor frequency.

$$f_0(MHz) \to f_0 + j\frac{\mu_0 \gamma \Delta H}{4\pi} = f_0 + j\frac{(2.8MHz/oersted)(\Delta H\ oersted)}{2} \tag{4.36}$$

4.3.2 Demagnetization Factor

The internal bias field, H_0 is not only dependent on the strength of the external static bias field H_a, but also the direction of the field due to boundary conditions at the surface of the ferrite [40]. Continuity of the tangential magnetic fields is an example of such boundary conditions. For a thin plate or layer, an internal bias field will be equal to the external bias field if it is in the direction parallel to the face of the layer. However, if H_a is in the direction normal to that face, then the internal bias field is reduced by a designated fraction of saturation magnetization.

$$H_0 = H_a - NM_s \tag{4.37}$$

This fraction is called the *demagnetization factor*, N. For thin plates, the demagnetization factor of the normal bias field is 1, and hence the internal field is reduced by the full saturation magnetization. The demagnetization factor can be represented by three components, N_x, N_y, and N_z, such that their sum is equal to 1. These three components represent the demagnetization factors in the x, y, and z-directions.

$$N_x + N_y + N_z = 1 \tag{4.38}$$

The components in (4.38) are illustrated in Figure 4.8 for thin plates, thin rods, and spheres. The three components of the internal magnetic bias field can be written as in (4.39).

$$H_{0x} = H_{ax} - N_x M_s \tag{4.39a}$$

$$H_{0y} = H_{ay} - N_y M_s \tag{4.39b}$$

$$H_{0z} = H_{az} - N_z M_s \tag{4.39c}$$

The choice in this analysis for a bias field in the x-direction was motivated by the fact that the demagnetization factor is zero in this direction and the internal bias field is unaffected by the saturation magnetization.

4.3.3 Bias Transverse to Direction of Propagation

Assume the geometry shown in Figure 4.1a where region 2 is a ferrimagnetic material with no variance in the x and y directions and a x-directed bias field. The incident wave is a plane wave traveling in the z-direction given by (4.40) where both $\vec{E}_0$ and $\vec{H}_0$ are constant vectors describing the transverse dependence of the fields.

$$\vec{E} = \vec{E}_0 e^{-jk_z z} \tag{4.40a}$$

$$\vec{H} = \vec{H}_0 e^{-jk_z z} \tag{4.40b}$$

Then the six components of the two curl Maxwell's equations are given by the following:

$$
\begin{aligned}
jk_z E_y &= -j\omega\mu_0 H_x && (4.41a)\\
-jk_z E_x &= -j\omega\left(\mu H_y + j\kappa H_z\right) && (4.41b)\\
0 &= -j\omega\left(-j\kappa H_y + \mu H_z\right) && (4.41c)\\
jk_z H_y &= j\omega\varepsilon E_x && (4.41d)\\
-jk_z H_x &= j\omega\varepsilon E_y && (4.41e)\\
0 &= j\omega\varepsilon E_z && (4.41f)
\end{aligned}
$$

Solving (4.41d,e) for H_x and H_y and inserting them into (4.41a,b,c), then (4.41a,b) can be written in terms of E_x and E_y only as given by (4.42).

$$
\begin{aligned}
k_z^2 E_y &= \omega^2\mu_0\varepsilon E_y && (4.42a)\\
\mu\left(k_z^2 - \omega^2\mu\varepsilon\right) E_x &= -\omega^2\varepsilon\kappa^2 E_x && (4.42b)
\end{aligned}
$$

It is evident that there are two possible solutions for the wavenumber, k_z, in (4.42). The first solution from (4.42a) which can only be obtained assuming $E_x = 0$, is given by (4.43).

$$k_o = \omega\sqrt{\mu_0\varepsilon} \tag{4.43}$$

This wavenumber represents that of an *ordinary wave* since it is unaffected by the magnetization. Therefore the permeability is that of free space and exhibits no magnetic behavior. This is due to the fact that the magnetic field components perpendicular to the direction of bias are zero, hence $H_y = H_z = 0$ for x directed bias fields. The other solution for k_z occurs when $E_y = 0$ for (4.42b) and is given by (4.44), where μ_e is given by (4.45).

$$k_e = \omega\sqrt{\mu_e\varepsilon} \tag{4.44}$$

$$\mu_e = \frac{\mu^2 - \kappa^2}{\mu} \tag{4.45}$$

This wavenumber and effective permeability are representative of the *extraordinary wave* which is affected by the magnetization and exhibits magnetic behavior. This permeability is dependent on the values, ω, ω_0, and ω_m introduced earlier in section 4.3.1. Thus if a wave has electric polarization in the y direction the wave is ordinary, while an x-directed electric polarized wave will be extraordinary. This effect is termed *birefringence* [40]. Figure 4.9 illustrates a plot of normalized effective permeability for an extraordinary wave as shown in (4.45). In Figure 4.9 the wavey line indicates the ferrimagnetic resonance (FMR) frequency which separates the region where the real part of permeability is positive ($\mu^2 > \kappa^2$) from the region where the real part of permeability is negative ($\mu^2 < \kappa^2$). Thus the effective wavenumber for an extraordinary wave, $k_e = \omega\sqrt{\mu_e\varepsilon}$, will show propagating modes for frequencies less than FMR. However, assuming negligible loss, the effective wavenumber will become purely imaginary for frequencies above FMR, and the waves will become evanescent. This is illustrated in Figure 4.10 for the effective wavenumber normalized by the free space wavenumber. A final note on FMR, as the static bias field is increased or decreased, the FMR frequency will also increase or decrease. This is a very useful property of ferrimagnetic materials since the permeability can be controlled.

4.4 Layered Composite of Ferrimagnetic and Dielectric Materials

This section analyzes the effects of layering on a composite consisting of alternating biased ferrimagnetic materials with anisotropic permeability and isotropic dielectric layers. The analysis follows the same approach as in section 3.2. The effective permittivity and permeability will be calculated for three different volume fractions and plotted versus number of layers in order to observe the effects of increased layering and volume fraction. The ferrimagnetic material is a magnetic garnet (Yttrium Iron Garnet, TYIG), with $4\pi M_S = 2050\ gauss$, $\Delta H = 5\ Oe$, $\varepsilon_T = 14 - \jmath 0.002$ and is biased by a static magnetic field in the x-direction with a field strength of 250 Oe. The YIG material properties are taken from a Trans-tech data sheet . The dielectric layers are Teflon with the properties $\varepsilon_T = 2.08 - \jmath 0.001$ and $\mu_T = 1$. The frequency was chosen to be 1GHz such that it is below FMR with a real permeability of approximately 10 and the material thickness is fixed to $2mm$ while the number of layers is increased for three different volume fractions. The choice of thickness was to ensure the composite was much smaller than a wavelength for homogenization. Using the formulation above, the reflection and transmission coefficients are calculated for the layered anisotropic region so that the effective permittivity and permeability may be extracted. Figure 4.11 illustrates the effective permeability of the layered composite for ferrite volume fractions $f_F = 0.75,\ 0.5$, and 0.25, for the case when the ferrite is the outside layer and also when the dielectric is the outside layer. Figure 4.12 illustrates the same analysis for the effective permittivity. As observed in 3.2, the permittivity and permeability can be controlled by the number of layers and volume fractions such that the tunable permeability range is 2.5 to 9.4 and 3.8 to 12.2 for tunable permittivity. This is summarized in Table 4.1. In conclusion, the effects of layering demonstrated in Chapter 3 for tunable permittivity based on volume fraction and contrast ratio have been illustrated here for both permittivity and permeability for physical materials that can be realizably manufactured into this form. Finally, a method for analyzing a structure with anisotropic materials has been presented and confirmed. This tool is used in a further analysis in the simulation of a layered compsoite which yields negative effective permittivity and permeability. This is described in the following section.

4.5 Simulation of Double Negative (DNG) Material

Double Negative (DNG) materials offer the potential for realizing interesting effects when used in a variety of applications. A DNG material is a composite material, or mixture, whether ordered or unordered, of two or more constitutive materials yielding effective properties significantly different than the individual components. The majority of these materials to date are made by embedding periodic metallic inclusions in a polymer matrix (sometimes literally by hand assembly using laminated boards [43]). There is some controversy regarding the behavior of such materials, especially on the scale of the inclusions themselves; however, there is clear macroscopic experimental evidence that some interesting behavior can be predicted if the two constitutive properties are simultaneously negative. One of the main subjects of controversy involves the use of periodic inclusions and whether such a composite material really can be interpreted as being DNG [44].

In this section, the use of non-periodic solutions to achieve both negative permittivity and permeability is discussed using the method derived in this chapter. The hypothetical composite will be formed by a bilayer stack comprised of alternating layers of narrow linewidth ferrite and suitable plasma tubes. The miniature plasma tubes can be created using microwave applicators [45] and can exhibit the behavior of negative permittivity for an operating frequency below the plasma frequency. Finally, the dimensions of the layers are key to homogenization: the effective materials properties must result from a large number of layers within a single wavelength.

4.5.1 Plasma as ENG Layer

Plasmas operating below the plasma frequency ($\omega < \omega_p$) will exhibit a negative effective permittivity as is evident by (4.46) for the effective permittivity of a plasma.

$$\varepsilon_{eff} = \varepsilon_0 \left(1 - \frac{\omega_p^2}{\omega^2}\right) \tag{4.46}$$

Typically, the plasma frequency can be calculated by (4.47), which is a function of number density, n, as well as charge of an electron, $e = 1.6 \times 10^{-19}$, mass of an electron, $m = 9.31 \times 10^{-31}$, and permittivity of free space.

$$\omega_p = \left(\frac{ne^2}{\varepsilon_0 m}\right)^{\frac{1}{2}} \tag{4.47}$$

Once plasma is immersed in a bias field, H_a, both the plasma frequency and effective permittivity will be altered. The plasma frequency is replaced with the upper hybrid frequency, ω_h, which is a function of both plasma frequency and cyclotron frequency [46]. The cyclotron frequency is dependent on the bias magnetic flux strength, $B = \mu_0 H_a$ where the permeability of the plasma is taken to be that of free space.

$$\omega_c = \frac{eB}{m} \tag{4.48}$$

Using (4.48) along with the plasma frequency the upper hybrid frequency is calculated and inserted into the equation for effective permittivity of plasma biased by a magnetic field.

$$\omega_h^2 = \omega_p^2 + \omega_c^2 \tag{4.49a}$$

$$\varepsilon_{eff} = \varepsilon_0 \left(1 - \frac{\omega_h^2}{\omega^2}\right) \tag{4.49b}$$

This effectively negative dielectric constant is illustrated in Figure 4.13 for two different number densities and two different bias field strengths. The upper hybrid plasma frequencies are also displayed for the different cases from left to right as vertical dashed lines. The effective permittivity is negative for frequencies to left of the dashed lines for the corresponding cases. As seen in Figure 4.13, increasing the number density or bias field strength will shift ω_h higher in frequency. This will be useful for controlling the plasma permittivity when trying to simulate a double negative material. The effective permittivity of biased plasma shown in (4.49b) and Figure 4.13 is an approximation that allows representation of the plasma as an isotropic medium. This is useful for quickly determining the number density and bias field strength necessary to achieve the desired plasma properties. However, the permittivity of magnetized plasma is anisotropic with the permittivity tensor shown in (4.50) for a bias field in the x-direction.

$$[\varepsilon] = \begin{bmatrix} \varepsilon_3 & 0 & 0 \\ 0 & \varepsilon_1 & j\varepsilon_2 \\ 0 & -j\varepsilon_2 & \varepsilon_1 \end{bmatrix} \qquad \hat{x} - bias \tag{4.50}$$

The elements of the permitivity tensor are given by (4.51).

$$\varepsilon_1 = \varepsilon_0 \left(\frac{(\omega_p/\omega)^2}{1 - (\omega_c/\omega)^2} \right) \tag{4.51a}$$

$$\varepsilon_2 = \varepsilon_0 \left(\frac{(\omega_p/\omega)^2 (\omega_c/\omega)}{1 - (\omega_c/\omega)^2} \right) \tag{4.51b}$$

$$\varepsilon_3 = \varepsilon_0 \left(1 - \frac{\omega_p^2}{\omega^2} \right) \tag{4.51c}$$

Ideally the plasma layer would be solely plasma, however this is not always practical. Therefore, the plasma layer can be implemented using an array of tightly packed plasma tubes or one wide plasma tube [45]. Preferably the tube or tubes would be rectangular in shape to improve packing. The tubes are generally made with quartz, which is used in this analysis and when referring to the plasma layer it implies that each layer is surrounded by a thin layer of quartz. Within each plasma layer, the quartz between adjacent plasma tubes has been neglected since it represents only a small portion of the layer volume and contributes little to the effective material properties.

4.5.2 YIG as MNG Layer

The other material in this double negative composite is a narrow linewidth magnetic garnet operated near ferrimagnetic resonance (FMR). Frequencies immediately above FMR will exhibit a negative effective permeability over a narrow frequency band as can be seen in Figure 4.9.

4.5.3 DNG Layered Composite

Now that the individual plasma and ferrite layers have been introduced, the layered composite with negative effective permittivity and permeability can be modeled through the use of the methods described in section 4.1. One layer consists of the tightly packed rectangular plasma tubes with electron number density $n = 8 \times 10^{17}\ (m^{-3})$. The thickness of each plasma layer is 0.5mm and surrounding the plasma layer is 0.1mm layers of quartz on both sides. YIG is again chosen as the narrow line-width ferrimagnetic material with layer thickness of 0.4mm and material properties described in section 4.3 The x-directed static bias field is chosen to be $100Oe$ such that the plasma permittivity and the ferrite permeability will be simultaneously negative as shown in Figure 4.14. These values were calculated using the effective permeability and permittivity equations given in (4.45) and (4.49b). Figure 4.15a illustrates the configuration for the first case to be analyzed. This case has the ferrimagnetic layer first followed by the quartz-plasma-quartz layer next and continues for a total number of seven plasma and ferrimagnetic layers. As expected, this composite yields effective constitutive parameters of a double negative material shown in Figure 4.16. Another observation is the non-trivial loss this material exhibits, rendering it so lossy it will not be of very much practical use except as a narrow-band absorber. The next case interchanges the ferrimagnetic and plasma layers as shown in Figure 4.15b and the permittivity and permeability are displayed in Figure 4.17.

This also yields double negative material properties along with the resulting high loss. An interesting result in this latter case is how the real and imaginary parts of permittivity and permeability are approximately the same around 2-2.1GHz. This implies that this material has all the same effects as the double negative composite however the wave impedance which is the square root of the ratio of permeability to permittivity is nearly 1, which is that of free space.

This section discussed using the formulation in section 4.1 to synthesize a DNG material through the use of multi-layer anisotropic structures. By using a layered material with alternating narrow linewidth ferrimagnetic and plasma sub-wavelength layers emerged in a static bias magnetic field, an effective double negative material can be achieved if operated at the proper frequencies. This multilayer structure avoided the use of transverse periodic arrays typically used to form a DNG material. Use of wave matrices allowed for determination of the propagator matrix, which was used to calculate the reflection and transmission matrices. This gave the S_{21} and S_{11} from which the complex permittivity and permeability of the composite could be extracted using a two dimensional traditional root searching algorithm and was shown to exhibit negative effective homogenized permittivity and permeability. There has been much research into DNG materials and their applications [47, 48, 49, 50, 51, 52]. The purpose of this section is to look at alternative physical materials in the making of such a material. It has been shown the layered composite does exhibit the effective properties of a DNG material, although the material exhibits high dielectric and magnetic loss as well as narrow bandwidth thereby limiting its practical applications. The fundamental explanation for this behavior is the fact that a resonator is used to achieve a negative effective permittivity (e.g. the ferrite acts like a lossy capacitive material).

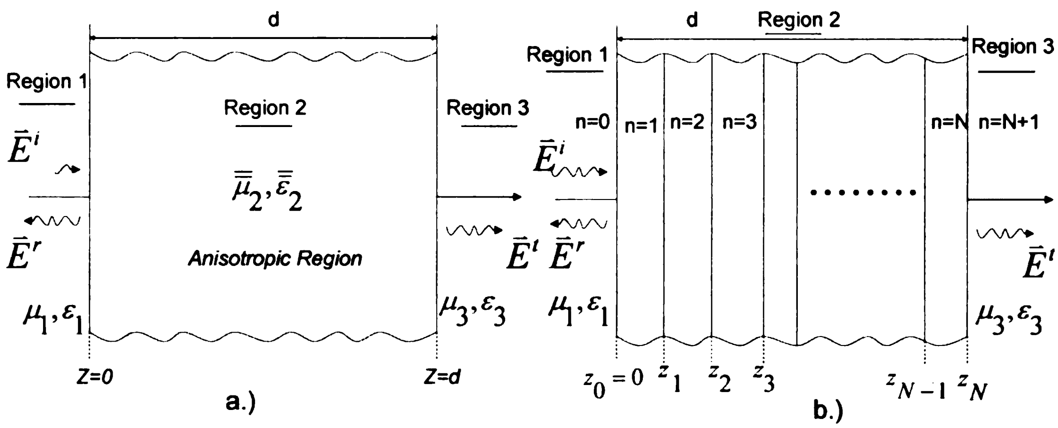

Figure 4.1. Geometry for anisotropic layered material derivation.

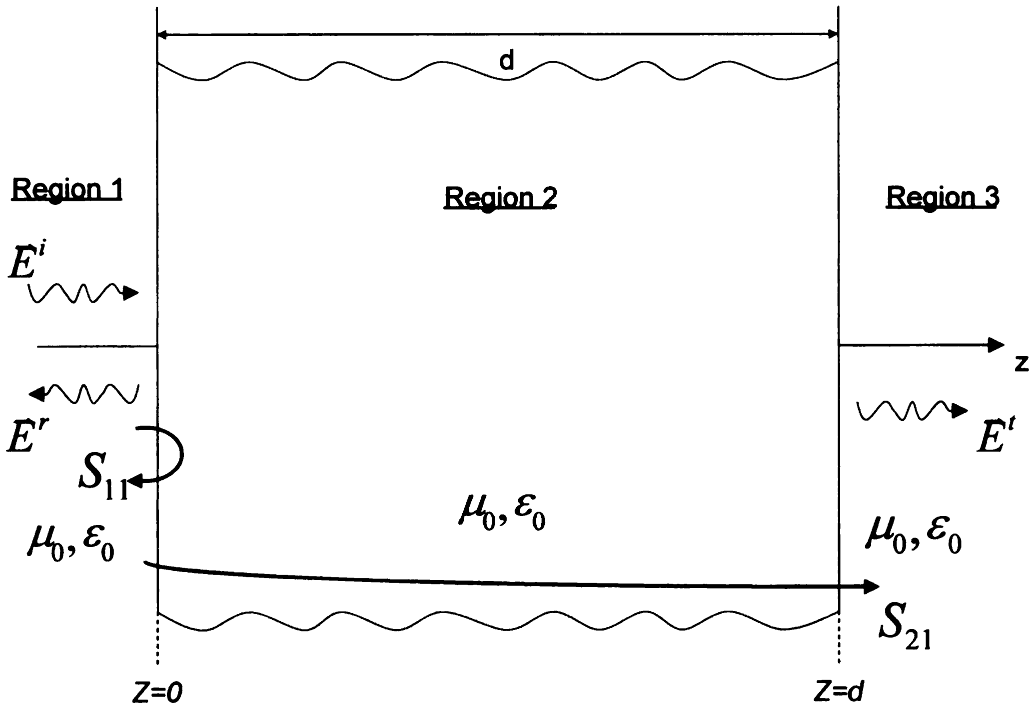

Figure 4.2. Transmission through free space geometry.

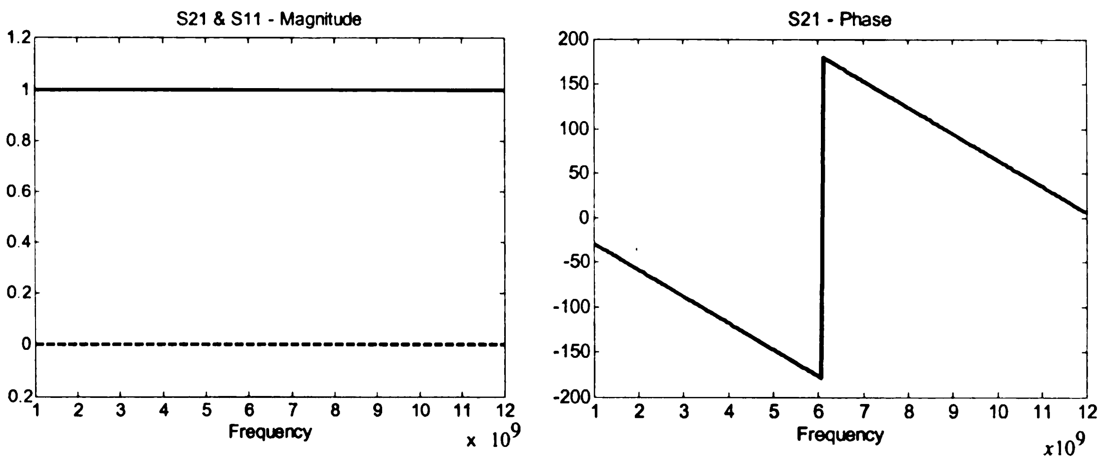

a.) b.)

Figure 4.3. Scattering parameters for free space case.

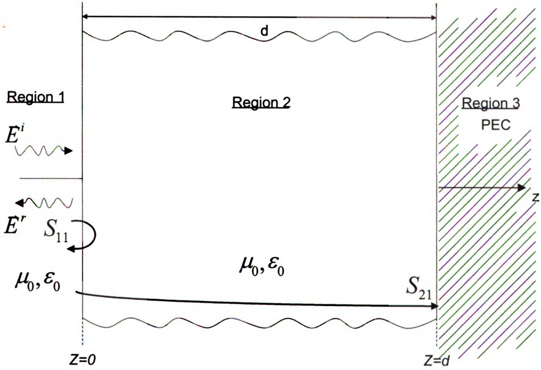

Figure 4.4. Reflection from PEC in region 3.

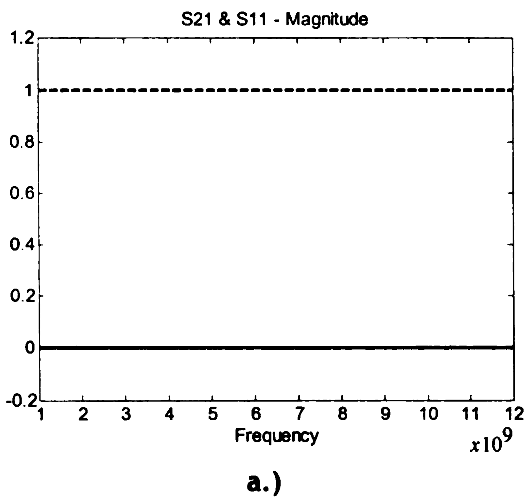

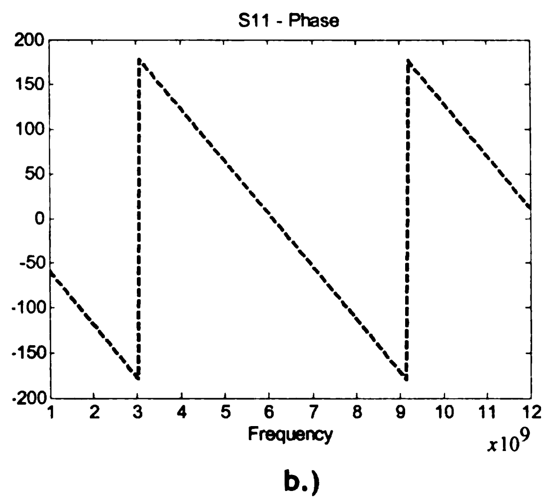

Figure 4.5. Scattering parameters for PEC case.

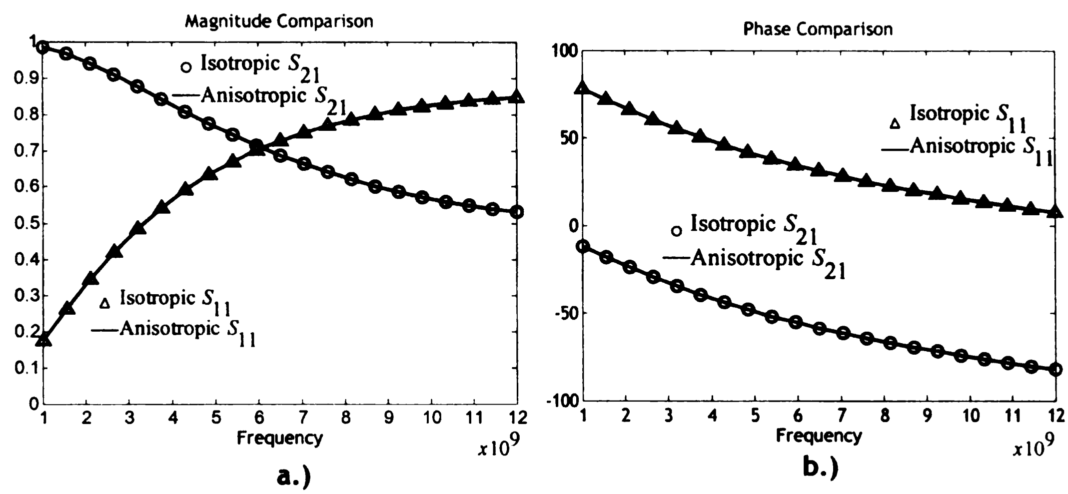

Figure 4.6. Comparison of calculated S-parameters using the isotropic and anisotropic formulations.

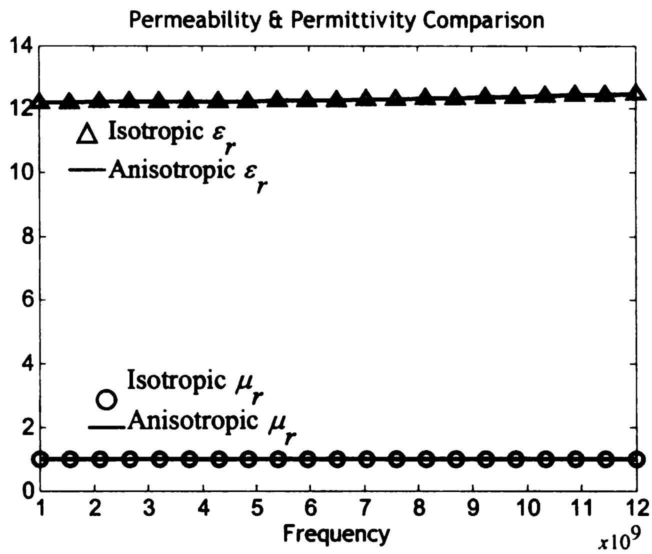

Figure 4.7. Comparison of extracted permeability and permittivity for both isotropic and anisotropic methods.

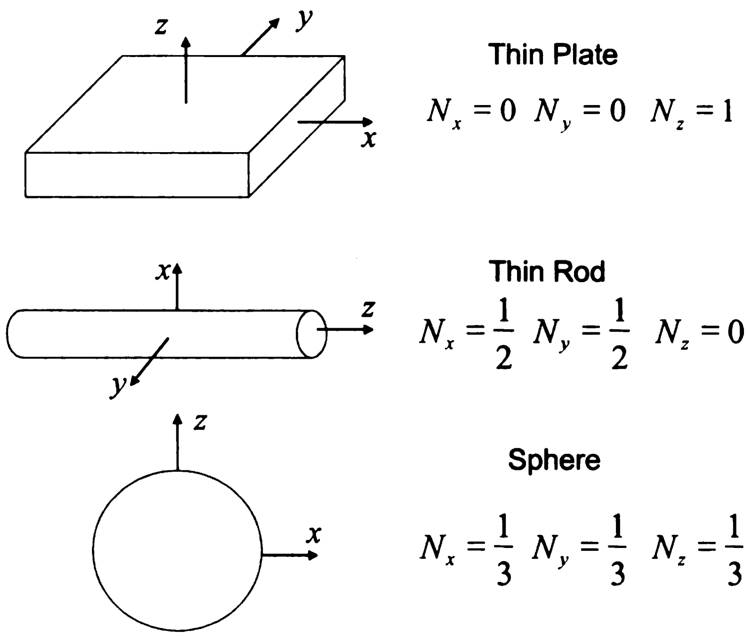

Figure 4.8. Demagnetization Factors for various geometries.

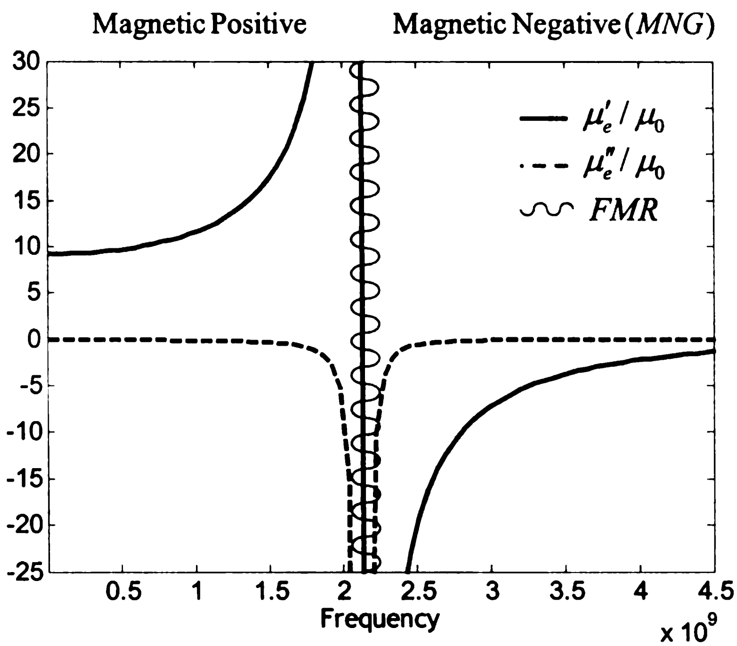

Figure 4.9. Effective permeability for extraordinary wave with the illustration of ferrimagnetic resonance (FMR).

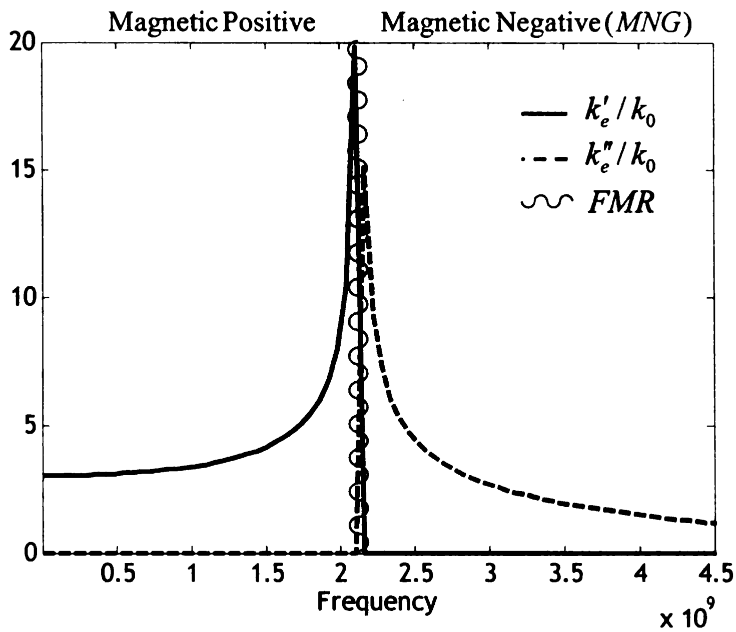

Figure 4.10. Effective wavenumber for extraordinary wave assuming negligible loss.

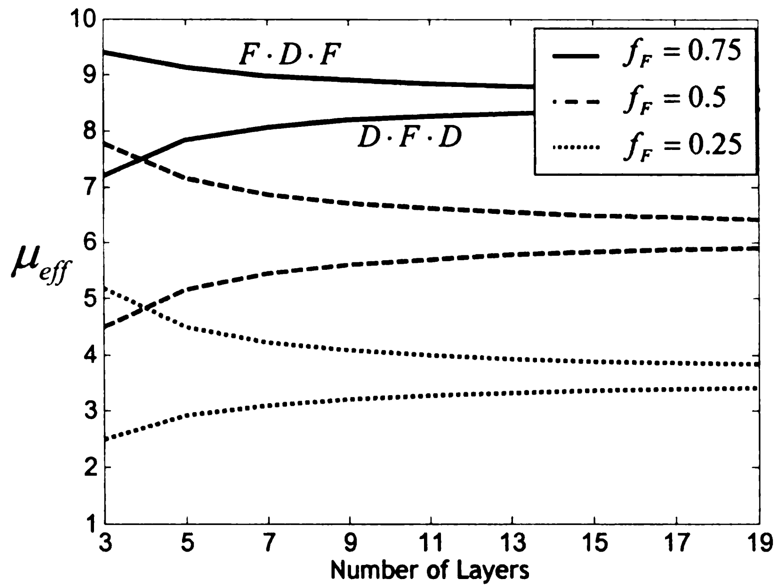

Figure 4.11. Effective permeability for layered anisotropic composite consisting of biased ferrite and dielectric materials for different volume fractions, where subscript "F" denotes the volume fraction of the ferrite. Also, F-D-F implies that the ferrimagnetic material is the outer layer while D-F-D implies that the dielectric layer is on the outside

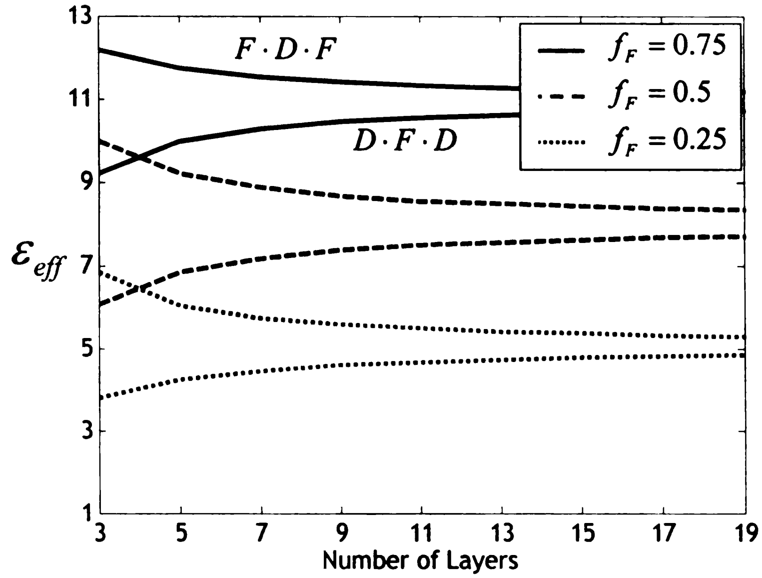

Figure 4.12. Effective permittivity for layered anisotropic composite consisting of biased ferrite and dielectric materials for different volume fractions, where subscript "F" denotes the volume fraction of the ferrite.

f_F	0.25	0.5	0.75	Total
μ_{eff}	2.5-5.2	4.5-7.8	7.2-9.4	2.5-9.4
ε_{eff}	3.8-6.8	6.1-10	9.2-12.1	3.8-12.1

Table 4.1. Tunable Effective Permittivity range summary for anisotropic layered composites.

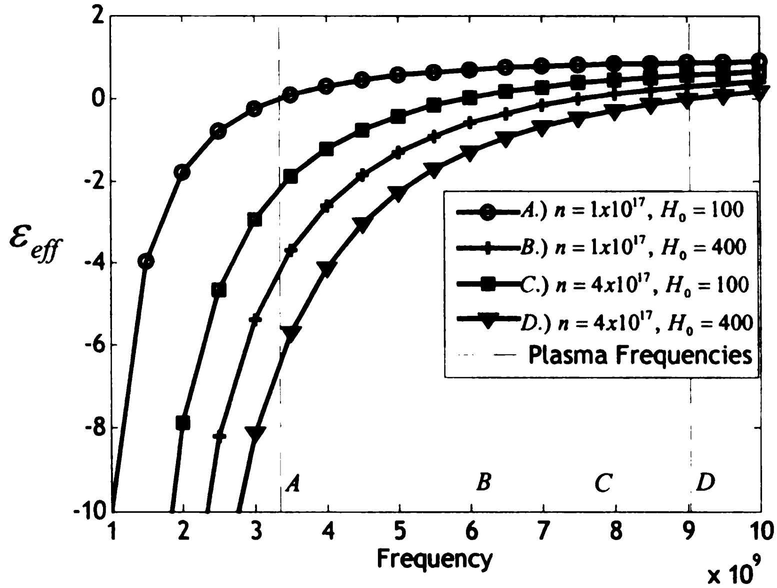

Figure 4.13. Effective permittivity for plasma immersed in a magnetic bias field.

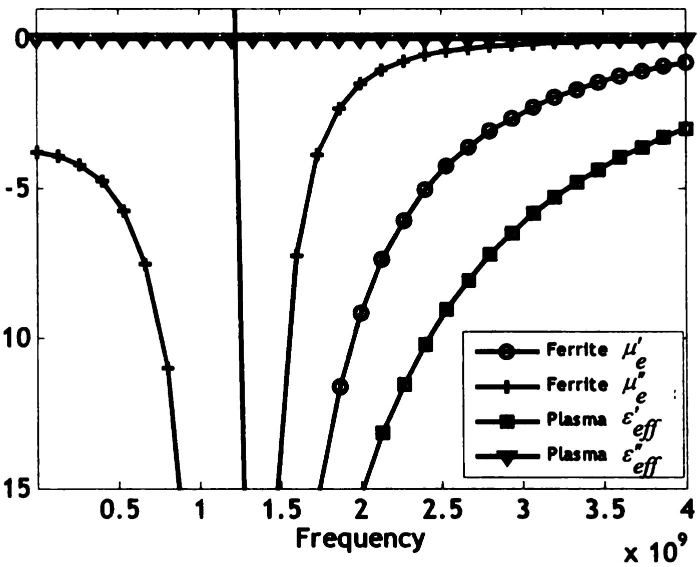

Figure 4.14. Ferrite effective permeability and plasma effective permittivity with negative values.

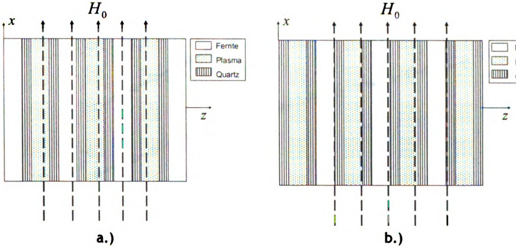

Figure 4.15. Layered composite for DNG simulation.

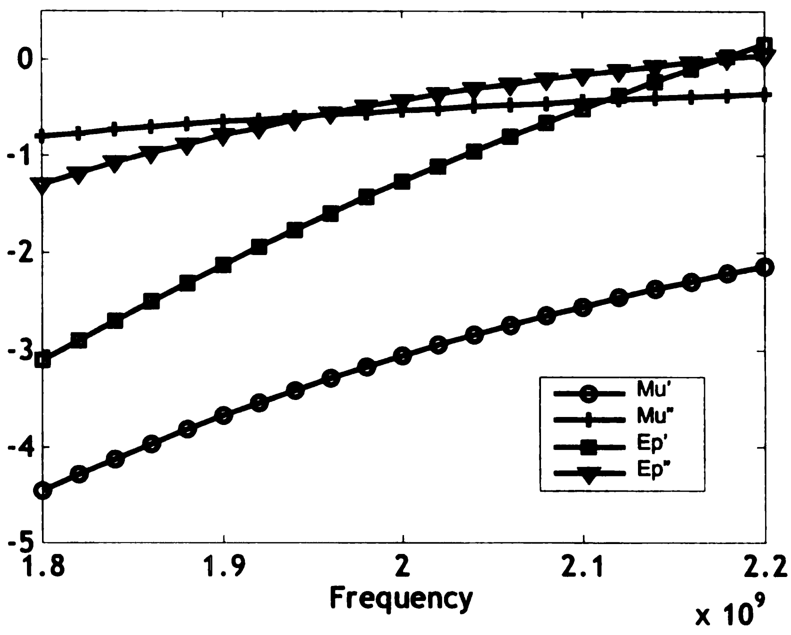

Figure 4.16. Negative permeability and permittivity for layered composite in Figure 4.15a.

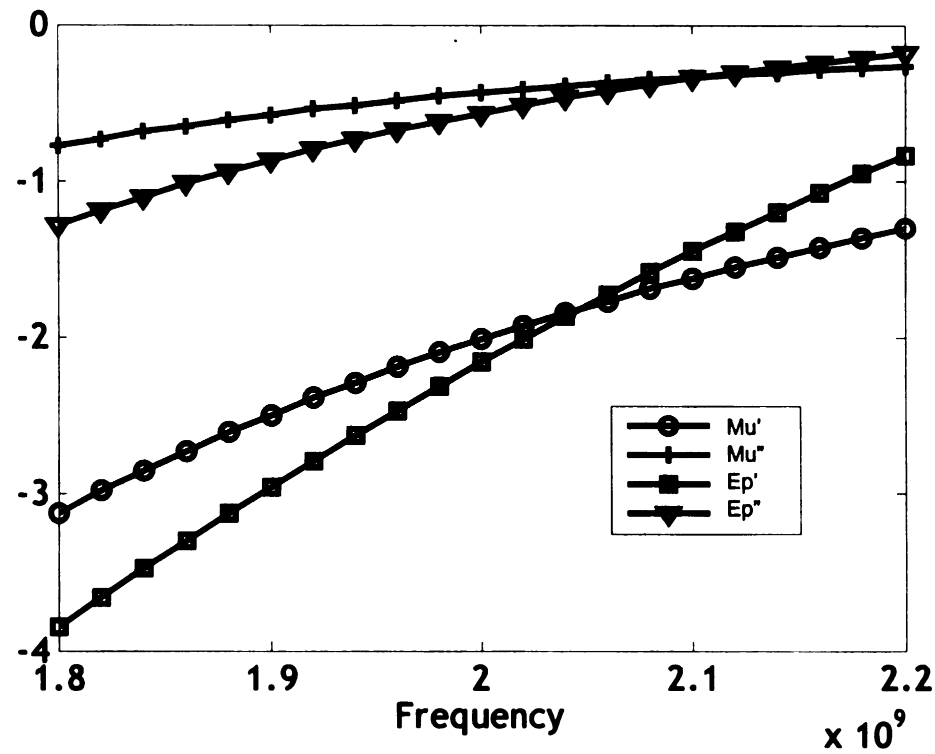

Figure 4.17. Negative permeability and permittivity for layered composite in Figure 4.15b.

CHAPTER 5

COMPOSITES WITH ROD SHAPED INCLUSIONS

The purpose of this chapter is to gain insight into the possibility of a composite material with tunable permittivity and permeability using a geometry consisting of rods (or wires) evenly dispersed throughout a background medium. As was done in the previous chapters, the scattering parameters are calculated at the front and back interfaces of the composite through which the complex permittivity and permeability can be extracted [5]. A domain integral equation formulation is employed to calculate the unknown electric fields within the material region [53, 54, 55]. Once these fields are known, the scattering parameters can be determined by taking the ratios of the reflected and transmitted fields to that of the incident field. The integral equation is solved using the method of moments with pyramidal basis functions and point matching over a mesh of triangular cells [58, 54, 55]. Although the composite is infinite in the y-direction, use of a periodic green's function allows the problem to be reduced to a unit cell. This unit cell is then replicated infinitely in the ±y-direction through a Floquet series [54]. However, the periodic Green's function is slowly converging when performing the necessary summation in the spatial domain. Therefore a method for accelerating this calculation using the Poisson summation formula is employed to convert the spatial summation into a spectral summation which is more rapidly convergent [56, 57].

Once the formulation has been completed and verified against exact solutions, the analysis will proceed using the same two materials as in the previous chapter. These are Teflon and a narrow line-width garnet, YIG, which is biased by a static magnetic field perpendicular to the direction of propagation. The bias field allows the permeability of the YIG to be controlled at the desired frequency of operation, see section 4.3. Although YIG is an anisotropic medium, the permeability tensor can be accurately simulated using a scalar quantity which predicts the effective permeability and allows the ferrimagnetic material to be modeled as an isotropic material [40]. The effects on the homogenized permittivity and permeability of the composite will be investigated by altering the volume fractions of the two materials and increasing the number of cylinders in the direction of propagation either in a row or stagered between adjacent layers. Finally, the effects of inserting holes, or pockets of free space, into the composite will be examined.

5.1 Background and Derivation

5.1.1 Geometry

The geometry of the unit cell for a core-shell cylinder inside a square background is illustrated in Figure 5.1. The two-dimensional surface, which lies in the x-y plane, is discretized into small triangles, called facets. The composite is assumed to be finite in the x-direction and to extend to $\pm\infty$ in the z-direction with no z-variation ($\delta/\delta z = 0$). Also, since the unit cell is replicated to $\pm\infty$ in the y-direction, the edges at the top and bottom of the unit cell are periodic boundaries. As will be explained further in section 5.1.2, the vertices of each triangle are the locations of the unknown electric field expansion functions called nodes. The fundamental geometry is designated such that concentric cylinders are placed in a rectangular region. The radius of the outer cylinder is chosen based on the desired volume fraction for that region. Thus for the example given by Figure 5.1, the outer radius gives a cylinder whose volume fraction is 0.5 implying that it occupies half of the total volume of the composite. Finally, the radius of the inner cylinder is always chosen as half the radius of the outer cylinder for convenience.

5.1.2 Integral Equation

The process of calculating the scattering parameters for this type of composite is done using an integral equation formulation for which the unknown electric field is found using the method of moments [53, 58]. An integral equation is one in which the unknown appears within the integral. This particular approach uses an electric field integral equation, $EFIE$, to model a two-dimensional penetrable scatterer assuming a normally incident transverse magnetic, TM, plane wave traveling in the +x-direction. The term penetrable is used to indicate that the unit cell is inhomogeneous with varying permittivity and permeability for which the incident wave can penetrate. This implies that the integral equation unknowns must be calculated throughout the entire domain as opposed to just along a particular surface, as is the case for a PEC scatterer or homogeneous region. In the example shown in Figure 5.1, the composite could be broken into three regions in which each region has a different permittivity and permeability. For instance, one region could be the area exterior to the outer cylinder, a second would be the ring-shaped area between the concentric cylinders, while the third and final area would be the innermost cylinder.

As illustrated in Figure 5.1, the unit cell is discretized into nodes, edges, and facets. The nodes represent the unknowns that are to be calculated and the patches are regions of constant permittivity and permeability while the edges separate these regions. In many cases, the unknowns are electric or magnetic currents; however, in the case of a penetrable scatterer it is often more convenient to represent the unknowns in terms of the electric and/or magnetic fields. In this work, the unknowns are the z-directed electric field as will be shown below.

Physically speaking, the incident plane wave will strike the composite and set up polarization currents within the material. These currents then reradiate a field called the scattered field. The superpostion of these two fields gives the total field.

$$\vec{E}^{tot} = \vec{E}^{inc} + \vec{E}^{sca} \tag{5.1}$$

One possible manner of representing the electric and magnetic scattered fields is in terms of their vector potentials. More specifically, the magnetic vector potential, $\vec{A}$, is calculated from electric current density, $\vec{J}$, and the electric vector potential, $\vec{F}$, from magnetic current density, $\vec{K}$, through the relationship given by 5.2.

$$\vec{A} = \vec{J} * G \tag{5.2a}$$

$$\vec{F} = \vec{K} * G \tag{5.2b}$$

The symbol $*$ is used to denote the spatial convolution where G signifies the Green's function. For the geometry used in this analysis, G is the two-dimensional free space Green's function

$$G = \frac{1}{4j} H_0^{(2)}(k|\vec{\rho}|) \tag{5.3}$$

where $H_0^{(2)}$ is the zero-th order Hankel function of the second kind representing an outgoing cylindrical wave with free space wavenumber, $k = \omega\sqrt{\mu_0\epsilon_0}$. Combining 5.2 and 5.3 and giving the convolution in its integral form, the vector potentials can be written by 5.4 where $\vec{\rho}'$ and $\vec{\rho}$ indicate source and observation locations, respectively.

$$\vec{A} = \iint \vec{J}(\vec{\rho}') \frac{1}{4j} H_0^{(2)}(k|\vec{\rho} - \vec{\rho}'|) d\vec{\rho}' \tag{5.4a}$$

$$\vec{F} = \iint \vec{K}(\vec{\rho}') \frac{1}{4j} H_0^{(2)}(k|\vec{\rho} - \vec{\rho}'|) d\vec{\rho}' \tag{5.4b}$$

Using 5.4, the scattered electric and magnetic fields can be calculated by the following equation through a process known as *integration-followed-by-differentiation* [54].

$$\overrightarrow{E}^{sca} = -jk\eta\overrightarrow{A} - \nabla \times \overrightarrow{F} \tag{5.5}$$

The symbol $\eta = \sqrt{\mu_0/\varepsilon_0}$ is the impedance of free space. Equation 5.5 represents the scattered electric field in terms of the electric and magnetic current densities. Using this expression in the equation for the total electric field and rearranging gives a commonly used form of an integral equation.

$$\overrightarrow{E}^{tot} + jk\eta\overrightarrow{A} + \nabla \times \overrightarrow{F} = \overrightarrow{E}^{inc} \tag{5.6}$$

The incident field is placed on the left hand side of this equation since it is a known quantity and for the upcoming linear algebra operations is the most convenient position. The unknowns on the right hand side of the equation are the electric and magnetic current densities as well as the total electric field. Each of these values are vector quantities which have three components, one for each direction in the Cartersian coordinate system (x, y, z).

Since the incident field is TM^z, all six of its electric and magnetic field components may be written in terms of the z-component of the electric field. Also, a z-directed electric field incident on a scatterer will induce surface currents that are in the z-direction and proportional to the total z-directed electric field. Therefore, it would be most beneficial to represent all the unknowns solely in terms of the z-directed total electric field E_z. Note the subscript "*tot*" for the total field has now been suppressed for ease of notation. The integral equation is now reduced from a vector form to a scalar form.

$$E_z + jk\eta A_z + \hat{z} \cdot \nabla \times \overrightarrow{F} = E_z^{inc} \tag{5.7}$$

The electric and magnetic vector potentials are functions of magnetic and electric currents which can also be written in terms of the total electric and magnetic fields through the following relationships.

$$\vec{J} = j\omega\varepsilon_0(\varepsilon_r - 1)\vec{E} \tag{5.8a}$$

$$\vec{K} = j\omega\mu_0(\mu_r - 1)\vec{H} \tag{5.8b}$$

where the relative permittivity and permeability are given by ε_r and μ_r, respectively. Now using the following form of Faraday's law, the magnetic field can be written in terms of the electric field. This can be used in the expression for the electric vector potential $\vec{F}$ through the calculation of the magnetic current density $\vec{K}$.

$$\nabla \times \vec{E} = -j\omega\mu_0\mu_r\vec{H} \tag{5.9}$$

$$\vec{K} = -\frac{\mu_r - 1}{\mu_r}\nabla \times \vec{E} \tag{5.10}$$

Now the integral equation in 5.7 can be written entirely in terms of the total z-directed electric field, E_z, using 5.10, 5.8b, and 5.2.

$$E_z^{inc} = E_z - k^2(\varepsilon_r - 1)E_z * G - \hat{z}\cdot\nabla \times \left\{\left(\frac{\mu_r - 1}{\mu_r}\nabla \times \hat{z}E_z\right) * G\right\} \tag{5.11}$$

Since it is a constant within each triangular region, the relative permeability in the last portion of the right hand side of 5.11 can be brought outside the curl operations. Also, since the integral operations will be performed numerically, it is more efficient to move the differentiation inside of the integral where it can be performed analytically. This changes the current process to a *differentiation-followed-by-integration* procedure [54]. The identity in 5.12 shows how the curl-curl operation in 5.11 can be reduced to a transverse laplacian operation.

$$\nabla \times \nabla \times \vec{A} = \left(\nabla_t \times \nabla_t \times \vec{A}_t - \frac{\partial^2 \vec{A}_t}{\partial z^2} + \nabla_t \frac{\partial A_z}{\partial z} \right) + \hat{z} \left(\frac{\partial}{\partial z} \left(\nabla_t \cdot \vec{A}_t \right) - \nabla_t^2 A_z \right) \tag{5.12}$$

Finally, the integral equation can be given entirely in terms of E_z in its most compact form.

$$E_z^{inc} = E_z - k^2(\varepsilon_r - 1)E_z * G + \frac{\mu_r - 1}{\mu_r} \nabla_t^2 E_z * G \tag{5.13}$$

The integral equation can now be solved for using the method of moments [58]. The scatterer is discretized into N nodes forming a mesh of triangular facets as demonstrated in Figure 5.1. The unknowns are expanded in terms of pyramidal basis functions in which the unknown becomes a linear interpolation of its surrounding nodes. This is illustrated in Figure 5.2 and displayed mathematically in 5.14 for a single triangular patch with a local numbering system such that local node 1 is the n^{th} node of interest.

$$B_n(x,y) = \frac{(x_2y_3 - x_3y_2) + x(y_2 - y_3) + y(x_3 - x_2)}{(x_2y_3 - x_3y_2) + x_1(y_2 - y_3) + y_1(x_3 - x_2)} \tag{5.14}$$

As node n is approached the value of the basis function tends to one, and as the other nodes are approached the basis function goes to zero. Using this basis function, the total field within the cylinder can be given by the superposition of the unknown electric fields multiplied by the basis function.

$$E_z(x,y) \approx \sum_{n=1}^{N} e_n B_n(x,y) \tag{5.15}$$

Applying point matching, and inserting 5.15 into 5.13 and separating out the still unknown electric field coefficient, e_n, the following matrix equation is formed.

$$\begin{bmatrix} Z \end{bmatrix} \begin{Bmatrix} e_1 \\ e_2 \\ \bullet \\ \bullet \\ e_N \end{Bmatrix} = \begin{Bmatrix} E_z^{inc}(x_1, y_1) \\ E_z^{inc}(x_2, y_2) \\ \bullet \\ \bullet \\ E_z^{inc}(x_N, y_N) \end{Bmatrix} \tag{5.16}$$

The impedance matrix, Z, is given by 5.17 where δ_n^m is the Kronecker delta funtion (i.e. $\delta_n^m = 1$ if $n = m$ and is zero otherwise). If the total number of nodes is given by N, the impedance matrix has NxN elements since for every m^{th} observation node there is a contribution from every n^{th} source node. For instance, the entry Z_{25} is the contribution of the field at node two due to the source at node five.

$$[Z] = \delta_n^m - \left\{ k^2(\varepsilon_r - 1)B_n * G + \frac{\mu_r - 1}{\mu_r} \nabla_t^2 B_n * G \right\}_{x=x_m, y=y_m} \tag{5.17}$$

Once the impedance matrix has been constructed, the unknown electric field coefficients, e_n, can be calculated by inverting the impedance matrix and multiplying it by the incident field column vector.

$$\{e_n\} = [Z]^{-1} \left\{ E_z^{inc} \right\} \tag{5.18}$$

In the process of evaluating the impedance matrix it is important to note that the terms which perform a derivative on the basis function can be reduced from a two dimensional convolution of the surface of each triangular patch to a one dimensional convolution over the patch's edges using Stoke's theorem. This is more easily seen in

5.11 with the curl-curl operation.

$$\iint \nabla \times (\nabla \times \hat{z}E_z) \cdot d\vec{S} = \int_{\triangle} (\nabla \times \hat{z}E_z) \cdot d\vec{l} \qquad (5.19)$$

The triangle symbol under the integrand in the right hand side is used to denote a closed loop integral around the entire triangular surface. The pyramidal basis function is now only differentiated once each with respect to x and y, then it is dotted with the vector tangent to the triangle edge being integrated, $d\vec{l}$. The second term on the right hand side in 5.17 is integrated over the surface of the facet and is performed using a seven-point quadrature routine.

A final important point involves the use of the pyramidal basis functions. As the impedance matrix is filled, the fields at node m due to the sources at node n are being calculated as mentioned earlier. However, this basis function is slightly more complex than in the case of pulse basis functions since the source at node n has contributions for all its neighboring facets for which it is a vertex. Therefore, in each entry of the impedance matrix there is a summation over all adjacent triangles at every n^{th} source node.

Section 5.2 will illustrate some examples of this formulation for a single circular cylindrical rod in free space along with comparison to an exact solution of the same problem for purposes of verification.

5.1.3 Periodic Green's Function

The geometry being modeled is a slab with dimensions that are infinite in the y and z directions and has a finite thickness in the x-direction. The infinite extent in the z-direction is accounted for by the fact that the problem is implemented in two dimensions (x-y plane). However, the infinite y-direction is realized through boundary conditions inherent in the periodic Green's function. These periodic boundary conditions are sometimes referred to as Floquet harmonics. The periodic Green's function with period b is given by 5.20 where the primary difference from the original Green's function in 5.3 is the dependence on the progressive phase shift of the incident field in the y-direction.

$$G_P(x,y|x',y') = \frac{1}{4j}\sum_{i=-\infty}^{\infty} H_0^{(2)}\left(k\sqrt{(x-x')^2+(y-y'-ib)^2}\right)e^{-jik_y b} \quad (5.20)$$

For the problem presented here, the incident field is propagating along the x-axis and therefore $k_y = 0$ and the exponential term at the end is equal to unity. This periodic Green's function may be inserted into 5.17 for the two-dimensional Green's function allowing for the simulation of a large (ie. infinite) structure to be reduced to that of a unit cell. The difficulty of this method is in the slow convergence of the periodic Green's function which involves a spatial summation of the zero-th order Hankel function [56, 57]. This is visually demonstrated in Figure 5.3 which shows how oscillatory the real and imaginary parts of the hankel function can be as the argument gets larger. The usefulness of the periodic Green's function is greatly limited by this slow convergence since it significantly increases the computation time in the method of moments solution of the integral equation formulation in order to get an accurate result. Therefore, it is desirable to find a method to accelerate this convergence.

The Green's function in 5.20 can be seen as a response to a periodic array of phase shifted point/line sources given by 5.21 [57].

$$J(x,y) = \sum_{i=-\infty}^{\infty} \delta(x-x')e^{-jk_y ib}\delta(y-y'-ib) \quad (5.21)$$

A method commonly referred to as the *Poisson sum transformation* can be applied to this expression for current which involves taking the Fourier transform and then its inverse [54]. The transform of the periodic array of point/line sources will give an array of periodic current sheets [57]. Once the inverse transform has been performed, the resultant expression for the periodic current sources is a spectral summation rather than a spatial summation.

$$J(x,y) = \frac{1}{b} \sum_{i=-\infty}^{\infty} \delta(x-x')e^{jk_{yi}(y-y')} \tag{5.22}$$

where

$$k_{yi} = \frac{2\pi i}{b} - k_y \tag{5.23}$$

Therefore the response to this expression for current is given by a new form of the periodic Green's function which is also a spectral summation and is proportional to the inverse of the period.

$$Gp(x,y) = \frac{1}{b} \sum_{i=-\infty}^{\infty} \frac{e^{-jk_x|x-x'|}}{2jk_x} e^{jk_{yi}(y-y')} \tag{5.24}$$

where

$$k_x = \begin{array}{ll} \sqrt{k^2 - k_{yi}^2} & \text{if } k^2 > k_{yi}^2 \\ -j\sqrt{k_{yi}^2 - k^2} & \text{if } k_{yi}^2 > k^2 \end{array} \tag{5.25}$$

For the "off-plane" case ($x \neq x'$), as $|i|$ is increased, the wavenumber k_{yi} transforms from positive real which represents an outgoing propagating wave to negative imaginary which gives an evanescent wave. Therefore, as $|i|$ increases, the summation in 5.24 begins to converge exponetially reducing the computational cost considerably. However, in the "on-plane" case ($x = x'$), the source and observation point lie on the same current sheet, and the exponetial term with k_x disappears and the summation is again slowly converging. There are additional/alternate approaches to accelerate the summation and to account for the "on-plane" situations [54, 56, 57], but as shown in section 5.2, this method provides sufficient accuracy as long as the summation is given enough terms in the case when $x = x'$.

A final consideration when using the periodic Green's function is that the nodes along the periodic boundaries on the top and bottom of the unit cell must be congruent. The reason is that the nodes along opposite boundaries are essentially the same node since as the unit cell is repeated in one direction or the other, the nodes that were on the top, become the nodes on the bottom and so on. For the case of a strip grating where a portion of the unit cell is PEC which has a surface contribution to the convolution integral, and the other is free space, which is not being integrated, the congruency can be easily realized. As long as that portion not being integrated is placed at one of the periodic boundaries there will be no further steps needed. However, if both boundaries contribute to the convolution, as is the case in this work, than this problem can not be ignored. If nothing is done, when the operation in 5.18 is done, the unknowns will be incorrectly calculated because the top and bottom nodes would have been superimposed yielding inaccurate results. The solution is to create the impedance matrix, $[Z]$, as normal but before calculation of the unknowns using 5.18 can be performed, the nodes at either the top or bottom must be eliminated after their contribution has been incorporated into the remaining entries of the impedance matrix. This is best explained through a simple example, consider the following 3x3 impedance matrix and 3x1 forcing vector.

$$[Z] = \begin{bmatrix} A_{11} & A_{12} & A_{13} \\ A_{21} & A_{22} & A_{23} \\ A_{31} & A_{32} & A_{33} \end{bmatrix}, \quad \{v\} = \begin{bmatrix} b_1 \\ b_2 \\ b_3 \end{bmatrix} \tag{5.26}$$

The 3x3 impedance matrix is analogous to a mesh containing three nodes. Suppose node three is the node on the periodic boundary chosen to be eliminated. The impedance matrix and forcing vector would be reduced to a 2x2 matrix and 2x1 column vector and the contribution from node three is absorbed into the remaining entries of the reduced tensors.

$$[Z_{new}] = \begin{bmatrix} A_{11} + A_{31} + A_{13} + A_{33} & A_{12} + A_{32} \\ A_{21} + A_{23} & A_{22} \end{bmatrix} \tag{5.27a}$$

$$\{v_{new}\} = \begin{bmatrix} b_1 + b_3 \\ b_2 \end{bmatrix} \tag{5.27b}$$

Even if the situation from the strip grating example were present in which the nodes along the periodic boundary were free space, this step could be utilized to reduce the size of the impedance matrix and forcing vector. The reason is that there would be no contribution from node three if it was free space and those entries would be zero.

Once the integral equation formulation in section 5.1.2 has been verified by comparison to the exact solution for the unit cell alone, see section 5.2, the periodic Green's function will be inserted in place of the two-dimensional free-space Green's function given by 5.3. This will give the infinite structure needed for the analysis.

5.2 Verification of IE Code

If possible, it is important that once computer code is written, it should be checked against exact solutions to look for errors. If it is not feasible to get an exact solution for comparison, then possibly one could obtain experimental data or even another code which has been verified. In this section, the code implemented in this dissertation will be compared against exact solutions for a circular cylindrical rod extending to infinity along its axis, and an infinite planar slab. The slab extends to infinity in both directions perpendicular to the direction of wave propagation.

5.2.1 Penetrable Cylinder

Surface currents on a penetrable cylinder in free space that extends to infinity in the z-direction along its axis will be compared to an exact solution using the integral equation described in section 5.1.2. A TM^z plane wave is incident in the x-y plane along the $\phi = 0$ direction and is assumed to have unit amplitude. Three cases will be calculated and compared to determine validity. These are for a purely dielectric rod, purely magnetic rod, and a combination of lossy dielectric and magnetic material properties. A derivation of the exact solution for scattering from a cylinder can be found in the appendix of [55]. The region outside the outer cylinder is set to free space while the region within the outer cylinder is set to a homogenous material depending on the rod material being analyzed. In all three cases the radius of the cylinder is 0.6λ.

The first case to be investigated is a lossless dielectric cylinder, with relative permittivity $\varepsilon_r = 4$. Figure 5.4 illustrates the accuracy of the integral equation calculations in both magnitude and phase for the surface currents along the cylinder. This provides assurance that the geometry and mesh input information are in correct format as well as the quadrature performing the surface integration is yielding accurate results. The next case will confirm the line integration is working correctly. The cylinder is now a purely magnetic rod with relative permeability $\mu_r = 3.3$ and $\varepsilon_r = 1$. Again, the results shown in Figure 5.5 demonstrate good agreement with the exact solution and verfication in the use of the line integral routine. The final test of the code is a cylinder with both permittivity and permeability greater than one, as well as dielectric and magnetic losses. The properties of the rod are $\mu_r = 5.1 - j0.2$ and $\varepsilon_r = 2.2 - j0.01$. Figure 5.6 shows good agreement between the integral equation formulation and the exact solution. The results of the previous three tests gives confidence in this code and its ability to accurately calculate the fields for a variety of material types. The following section will take the verification process one step further and ensure that the periodic green's function is properly implemented.

5.2.2 Infinite Slab

This section will check the validity of the periodic Green's function when inserted into the integral equation code which was demonstrated to yield accurate results in section 5.2.1. The periodic green's function allows in infinite periodic structure to be modeled using only a unit cell the size of the structure's period. Verification of this capability can be accomplished through comparison of scattering parameters for that of an infinite homogeneous slab. The exact solution for scattering from a slab has been illustrated in both chapters 3 and 4 for isotropic and anisotropic materials, respectively. As before, the incoming wave is TM^z and normally incident on the planar surface. The thickness of the slab is 5mm and the material properties are the same as those in the preceding example of a lossy magneto-dielectric rod, $\mu_r = 5.1 - j0.2$ and $\varepsilon_r = 2.2 - j0.01$. The scattering parameters, S_{11} and S_{21}, are calculated from 1-3GHz. Figure 5.7 shows how accurate the integral equation formulation is able to calculate the scattering from a structure with infinite one-dimenstional periodicity.

One further test of this formulation is to extract the complex permittivitiy and permeability from the scattering parameters of the slab using a two-dimensional Newton's root searching algorithm as described section 2.4.3. The permittivity and permeability of the slab whose scattering parameters are given by Figure 5.7, are shown versus frequency in Figure 5.8. The extracted values are exactly the permittivity and permeability entered in order to calculate the scattering parameters.

The code and formulation has now been sufficiently verified, the next step is to see the effects of various circumstances on the homogenized permittivity and permeability of a composite involving cylindrical shaped inclusions.

5.3 Analysis of Composite

Now that the formulation and code has been verified as being capable of handling this analysis, the goal is to understand how this type of geometry can be used to control and effectively tune the electromagnetic properties of a composite containing rod shaped inclusions. The investigation will proceed using the same two materials used in the analysis of layered anisotropic materials in chapter 4 and the frequency will again be $1GHz$. The dielectric material is Teflon with $\varepsilon_r = 2.08 - j0.001$, $\mu_r = 1$ and the magnetic material is YIG with a static magnetic bias field directed along the axis of the cylinder. The choice for this direction of the magnetic field is due to the fact that the demagnetization factor along this axis is zero and hence does not require a very strong field to achieve the desired magnetic properties. This is equivalent to a bias field in the direction transverse to the wave propagation in the layered material analysis in the previous chapters. The permeability of the magnetic material is modeled using the extraordinary wave effective permeability from 4.45. The permeabililty for a slab of anisotropic ferrimagnetic material with a bias field perpendicular to the direction of propagation is caclulated using methods of chapter 4 and given in Figure 5.9 along with the permeability using 4.45. This reinforces the possibility of representing the anisotropic magnetic material in this analysis using a scalar value for simplicity without loss of accuracy. In the following cases, the thickness of the composite slab is kept constant at 2mm. The effects of layering are investigated by increasing the layers of rods from one to five layers. By varying the radius of the cylindrical inclusions, the volume fraction effects can be illustrated. Also, the effects of placing holes, cylinders of free space, inside the composite are analyzed and finally for all situations the dielectric and magnetic materials are interchanged to see those effects as well.

5.3.1 Geometries

The mesh created for each geometry begins with a specified volume fraction for the cylindrical inclusions. The two main choices have been 0.5 and 0.2 which implies that the volume contained within the outermost cylindrical radius is half and one-fifth the total composite volume, respectively. However, within each mesh is a second concentric cylindrical ring at a radius exactly one-half that of the outer radius. This additional radius gives the option to analyze smaller volume fractions or to attempt any core-shell models. A consideration of the mesh will show how the actual volume fractions differ from the specified volume fractions of 0.5 and 0.2 since the cylinders are broken up into eight triangles as illustrated in Figure 5.1. This actually gives a volume fraction of 0.45 and 0.18 rather than 0.5 and 0.2 respectively. Finally, the effects of additional layers of cylinders inline with each other and staggered are incorporated as well. Figure 5.10 - Figure 5.14 show all of the geometries created and described in this paragraph where the values of a, b, and h are different depending on the situation while $t = 2mm$ in all cases.

5.3.2 Increasing Layers

The first case involves the magnetic cylinders with inclusion phase volume fraction of 0.45 and the number of cylinders are increased from one to five. Figure 5.15 a,b illustrates the effective permittivity and permeability for the case when the layers are aligned such that each successive rod is directly behind the other. Figure 5.15 c,d is for the case when the rods are staggered. It is clear that there is no effect on the composite's electromagnetic properties when increasing the number of layers for evenly spaced cylindrical rod-shaped inclusions. Another important observation is the permittivity and permeability are the same whether the rods are aligned in a straight row or whether they are staggered. These results could be the consequence of the electrical sizes of the rods and composite structure. The thickness of the entire composite is only $1/150^{th}$ of a free-space wavelength and the rod is still smaller yet. The subwavelength thickness allows the properties of the material to easily become homogenized as in the case of large number of planar layers. In comparison to increasing planar layers, as the number of cylinders increases, wave propagation is not impeded as dramatically since portions of the slab with cylinders are homogeneous depending on the line of sight which would allow for easier propagation. As the planar layers are increased the waves experience more reflections or bounces and this creates different values for permittivity and permeability and increases loss in the case of greater attenuation. The effect of increasing the number of cylinders was investigated for other volume fractions and the result was always the same and therefore those results have been left out of this work to avoid redundancy. All the following analysis have also been performed for one, three and five layer cases but have also been left out here for the same reason.

5.3.3 Volume Fraction

The next aspect of design to be investigated involves the effects of volume fraction. For the case of a one cylinder layer a volume fraction of 0.45 would require an outer cylinder radius of $b = 0.8mm$ giving an inner radius $a = 0.4mm$. The volume fraction for the outer radius of $0.8mm$ implies that the entire cylinder including the inner cylinder is part of that inclusion phase. Thus the inner radius yields a volume fraction of 0.08 for the inclusion phase. In the other case, with a volume fraction of 0.18, the outer radius is $b = 0.5mm$ and the inner radius becomes $a = 0.252mm$ analogous to a volume fraction of 0.032. Therefore, with these two meshes, four different volume fractions can be investigated and then if the materials are interchanged, such that Teflon becomes the cylindrical inclusion and YIG becomes the environment medium, another four volume fractions of the magnetic material can be realized which are 0.55, 0.82, 0.92, and 0.968. The effects of volume fraction on homogenized permittivity and permeability have been illustrated in Figure 5.16a for increasing volume fraction. The loss tangents are given in Figure 5.16b.

As expected, the effective permittivity and permeability increase as the volume of YIG is increased within the composite. The permittivity increases steadily as the volume fraction is increased. On the other hand, it seems that volume fraction has only a slight effect on permeability when that value is below 0.45 and the rod is YIG with a surrounding dielectric. Once the materials have been interchanged the permeability takes a large jump from 2 to 4.3 for the a volume fraction of 0.55 then begins to take a steady increase as the volume fraction is continuously raised. This phenomenon also occured in Chapter 4 for the case when the YIG was the outer layer a higher effective permeability was achieved. A possible explanation for the large jump in permeabililty is that when the YIG is the environment it interacts with the incoming field directly as opposed to the wave propagating through the dielectric first and this seems to yield a greater permeability. This is evident in the case of interchanging the YIG and Teflon material phases. However, having the YIG as the environment gives it a planar surface, which happens to match the incident field's wavefront and this could have an impact on the permeability as well. It should be noted that greater volume fractions for the cylinder were not attempted because the cylinder would need to take on non-cylindrical shapes if the volume fraction were going to increase in order to fit within the unit cell. This analysis illustrates a tuneable relative permittivity from 2.8-13.9 and relative permeability from 1-10.8 based on the volume fraction of YIG versus that of Teflon. Unfortunately, for the cylindrical geometry, as the volume fraction for YIG is increased, the magnetic loss is also increased.

In many situations, researchers are avoiding the use of magnetics because of the loss inherent in most magnetic materials. Therefore, much work involves purely low-loss dielectric composites consisting of some polymer and a ceramic called alumina which has a dielectric constant of 10 [59]-[62]. So as an illustration, a composite consisting of Teflon and alumina will be analyzed using this geometry over various volume fractions. The composite will begin with an alumina cylindrical inclusion and the Teflon background material and once a volume fraction of 0.45 is reached, the materials will be switched as was done previously. The results are displayed in Figure 5.17. Only the permittivity has been included in the plot since the composite is non-magnetic. The effective permittivity for this composite takes a similar trend to that of the YIG and Teflon previously shown and gives a tunable permittivity range of 2.3 to 9.8 with very low loss.

5.3.4 Free-Space Inclusions

The final step in analyzing this composite is to see the effects of holes, or pockets of free space on the permittivity and permeability. The first of four trials is just a YIG cylinder inside Teflon, followed by replacing the innermost cylinder by Teflon which gives a dielectric filled cylinder of YIG inside Teflon. The third trial is to remove the innermost cylinder and replace it with free space giving a hollowed out YIG cylinder, and finally removing the YIG altogether and filling the entire cylindrical region with free space surrounded by Teflon. These configurations are given in Figure 5.18 with the extracted values of permittivity and permeability for the two meshes having volume fractions of 0.45 and 0.18 are displayed in Figure 5.19 and Figure 5.20, respectively. The permittivity seems to be effected slightly when the core of the YIG rod is replaced with Teflon and seems unaffected by removing the Teflon and replacing the core with free space. The final case shows a drastic drop in permittivity down to a value just slightly less than that of Teflon by itself. This is expected because the high contrast composite has been replaced with a very low contrast composite once the YIG is completely removed. The permeability seems to be unaffected by the changes made until the YIG is completely removed and the composite no longer contains any magnetic material which gives an expected value of one for permeability.

Now the materials are swapped as was done in the case of the volume fraction analysis. The first of four trials is a Teflon cylinder inside a YIG background, followed by a YIG cylinder inside the Teflon cylinder. Finally, the last two steps are to have a hollow Teflon cylinder inside YIG and then removing the Teflon altogether giving a YIG background with a free space cylinder inside. These geometries are given in Figure 5.21 while the extracted permittivity and permeability are shown in Figure 5.22 and Figure 5.23 for outer radius inclusion volume fractions of 0.45 and 0.18 respectively. The permeability appears to be unaffected by the different cylinders of Teflon and free space except for the case of a Teflon rod with a YIG core which causes a slight increase. The permittivity seems to decrease a small amount as the quantity of free space is increased. When the YIG is used as the environment, it appears to dominate the effective electromagnetic properties since it is the higher permittivity and permeability in this high contrast composite. Therefore the difference in permittivity and permeability for Teflon and free space does not seem to make a significant difference and therefore could replace the Teflon if weight was an issue in the design of a composite.

5.4 Conclusions

In this chapter, an integral equation formulation has been shown to accurately evaluate a structure with infinite periodicity in one direction. The use of a periodic Green's function allows the mesh to be truncated to that of a unit cell the size of one period and reduced computation time greatly. The integral equation calculation was shown to match exact solutions for a cylinder in free space and an infinite slab of a homogeneous material with both complex permittivity and permeability. The analysis of composites with rod shaped inclusions proceeded by first looking at the effects of increasing the layers or number of rods within the composite. This showed a negligible change in the effective permittivity and permeability and thus is not a good design tool for tuning those properties if the columnar inclusions are evenly distributed. The next mode of analysis involved the effects of increasing volume fraction which did yield a significant change in the permittivity and permeability and could possibly be a method for creating a composite with the desired electromagnetic characteristics. Finally, the last case analyzed was the effects of inserting inclusions of free-space into the composite and it was shown that the difference was small compared to the effects of having Teflon cylinders instead. Therefore, unless the weight of the composite is of great concern, it may just be best to use a polymer with low dielectric constant such as Teflon.

In conclusion, the best tool for material composite design with tunable electromagnetic properties using this geometry is to alter the volume fraction of each material.

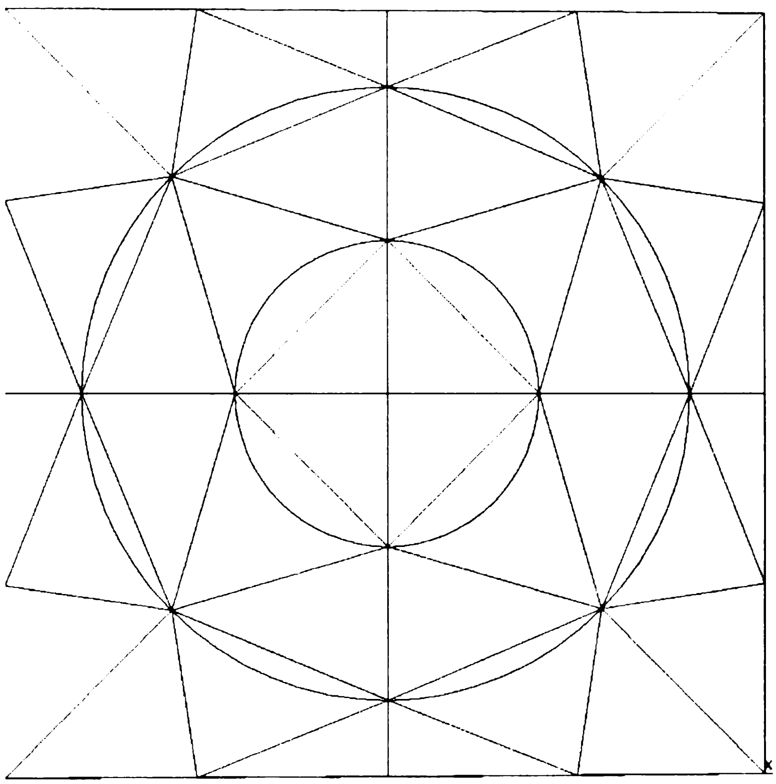

Figure 5.1. Geometry and mesh for core-shell model used in IE formulation.

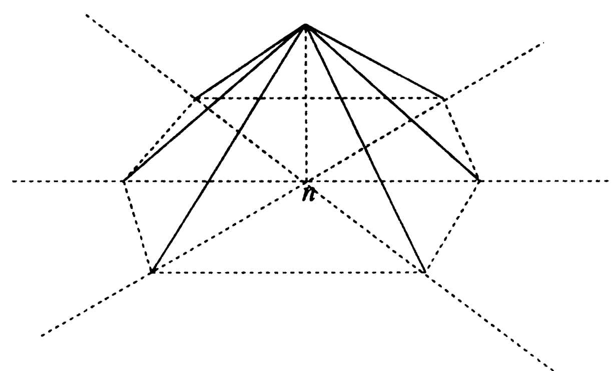

Figure 5.2. Pyramidal basis function for node n [53, 54, 55]

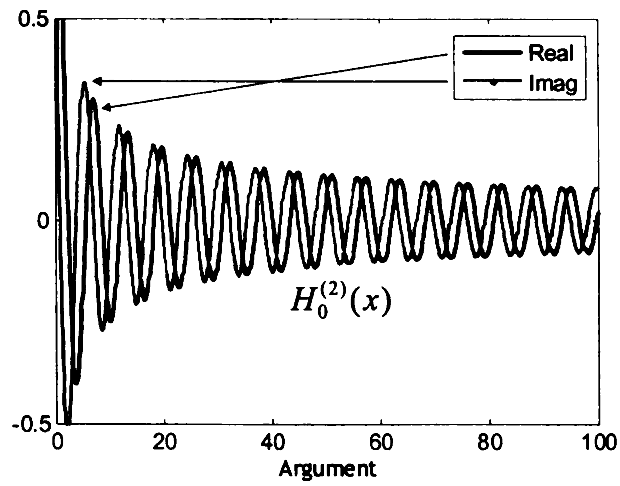

Figure 5.3. Convergence of the hankel function.

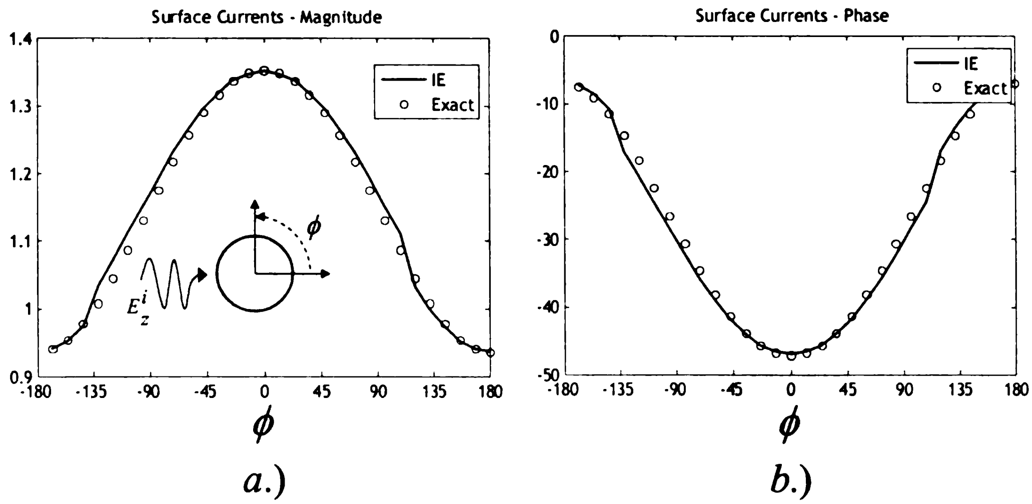

Figure 5.4. Comparison of the exact and IE surface fields for dielectric rod.

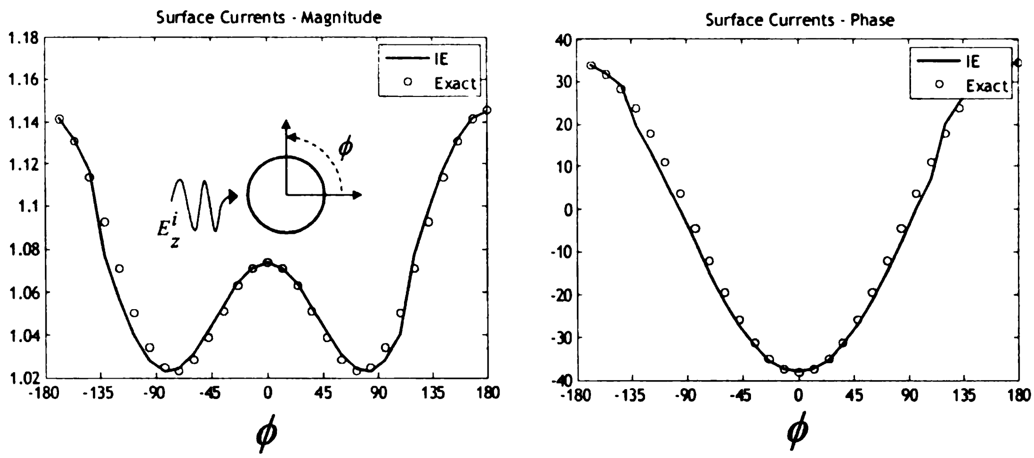

a.) *b.)*

Figure 5.5. Comparison of the exact and IE surface fields for magnetic rod.

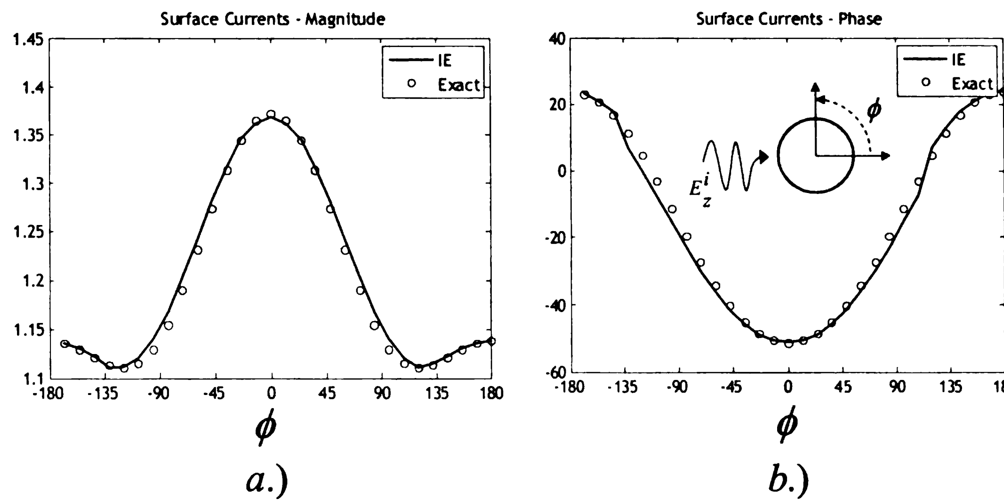

Figure 5.6. Comparison of the exact and IE surface fields for lossy rod.

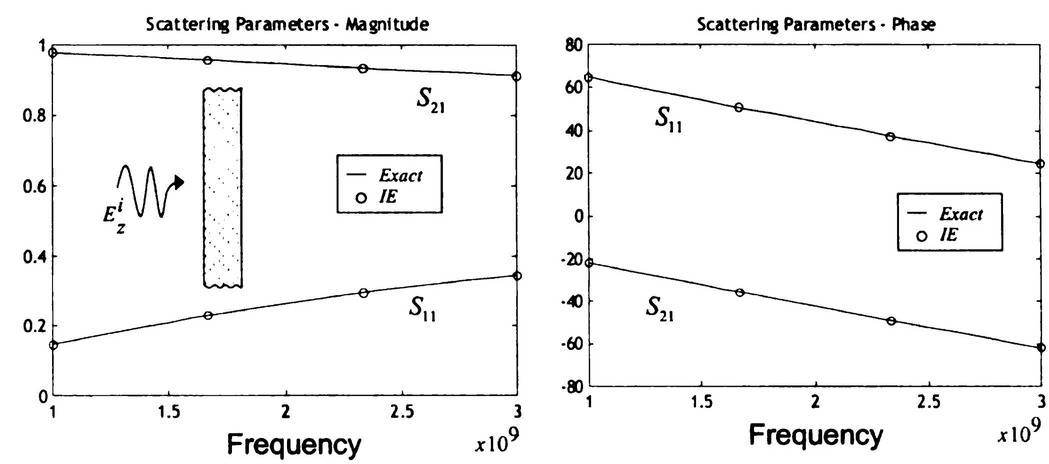

a.) *b.)*

Figure 5.7. Comparison of the exact and IE scattering parameters for lossy slab.

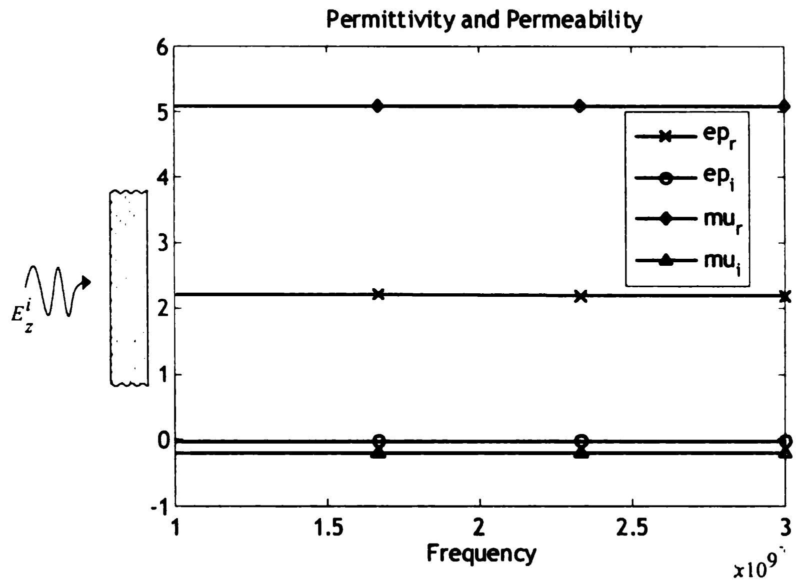

Figure 5.8. Extracted permittivity and permeability for a lossy slab.

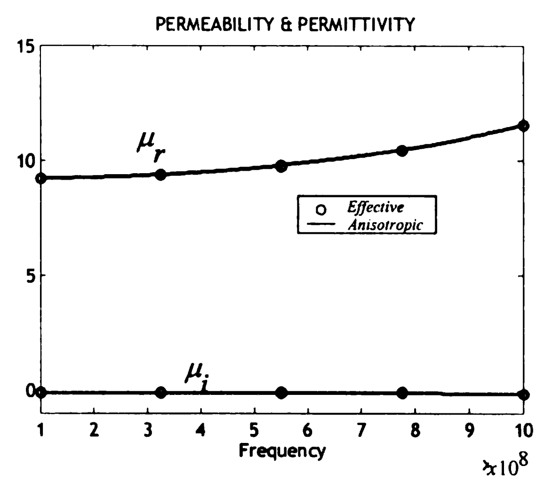

Figure 5.9. Comparison of effective permeability of anisotropic to isotropic ferrite.

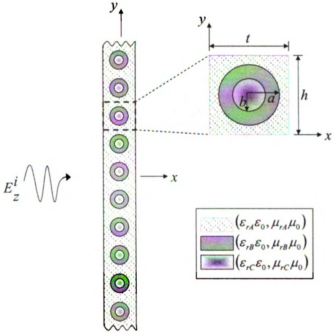

Figure 5.10. Geometry and unit cell for the core-shell model with one cylinder.

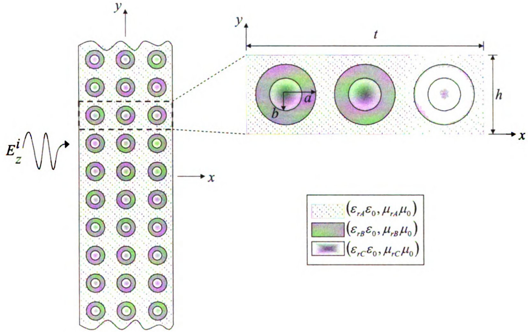

Figure 5.11. Geometry and unit cell for the core-shell model with three cylinders.

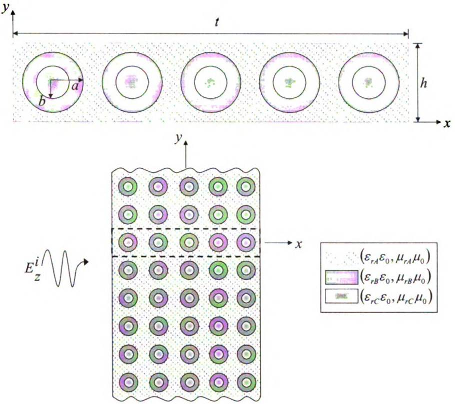

Figure 5.12. Geometry and unit cell for the core-shell model with five cylinders.

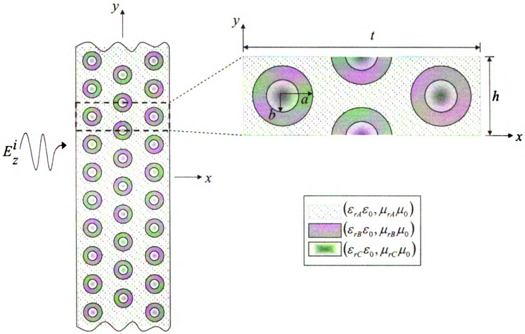

Figure 5.13. Geometry and unit cell for the alternating core-shell model with three cylinders.

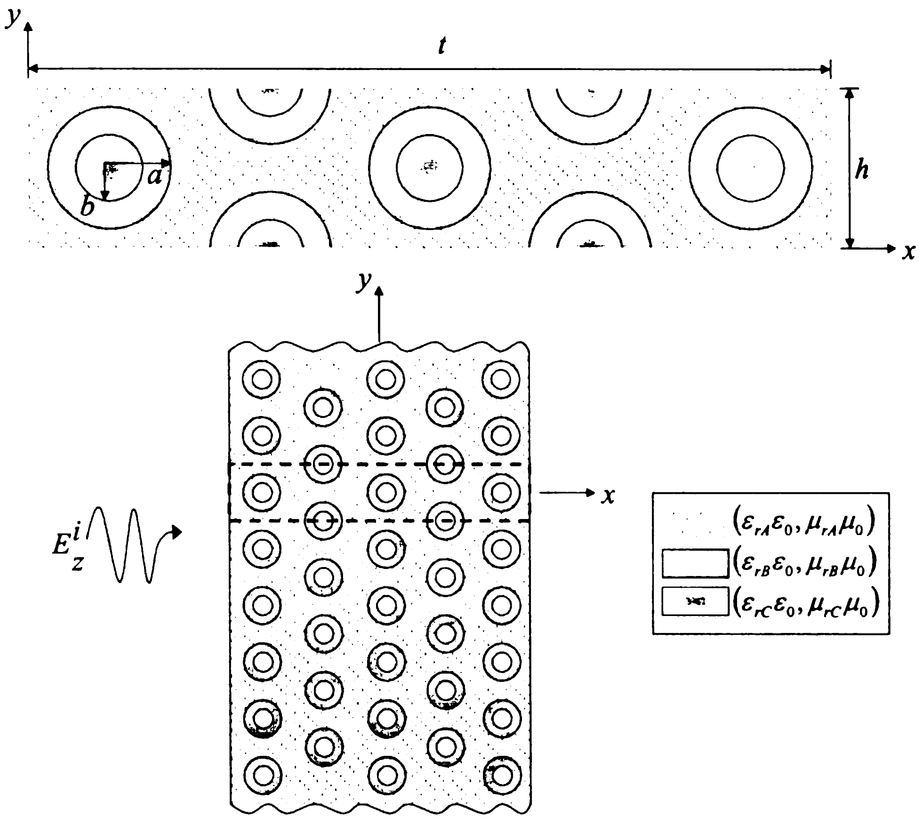

Figure 5.14. Geometry and unit cell for the alternating core-shell model with five cylinders.

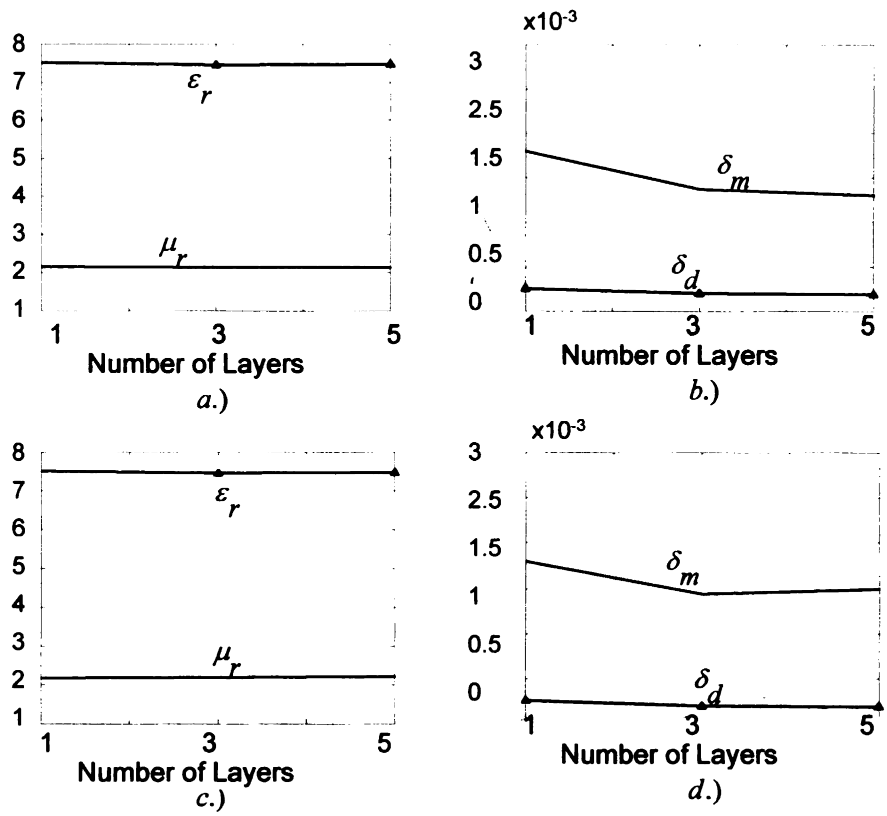

Figure 5.15. Effect of increasing layers on homogenized permittivity and permeability for rods in a row [a,b] and alternating [c,d] with a volume fraction of 0.45.

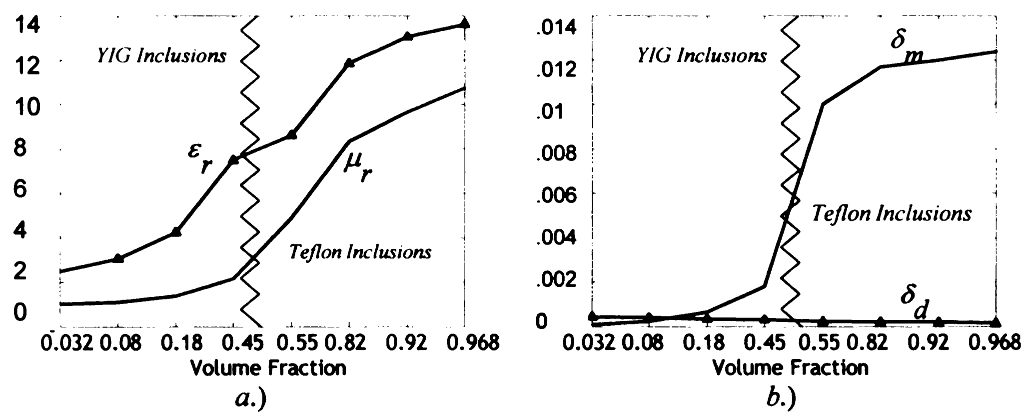

Figure 5.16. Effect of increasing volume fraction on homogenized permittivity and permeability.

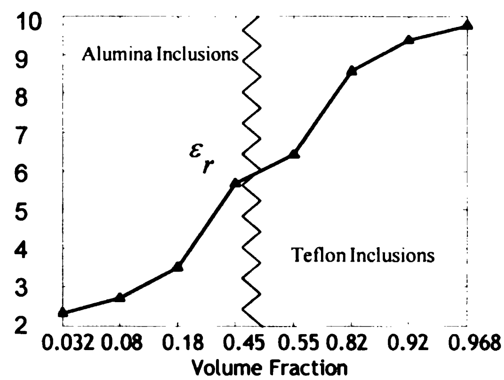

a.)

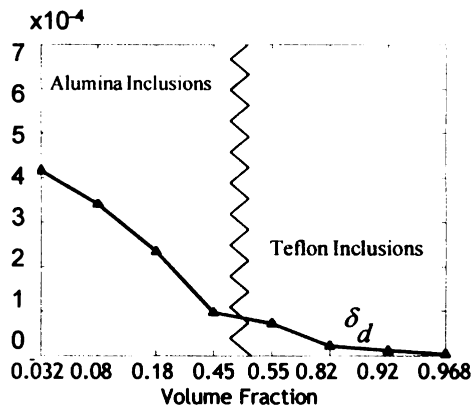

b.)

Figure 5.17. Effect of increasing volume fraction on homogenized permittivity for composite consisting of alumina and teflon.

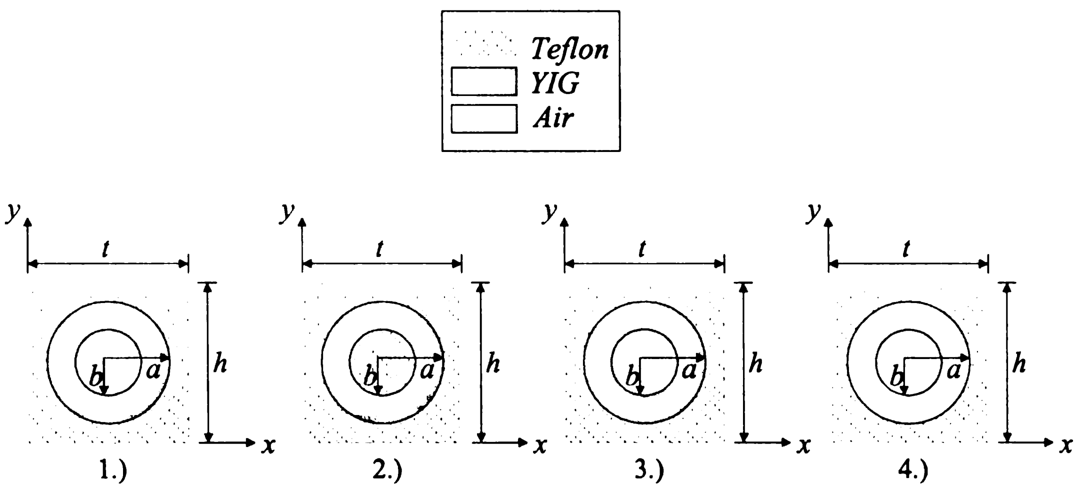

Figure 5.18. Geometry for analysis on effects of air gaps on permittivity and permeability.

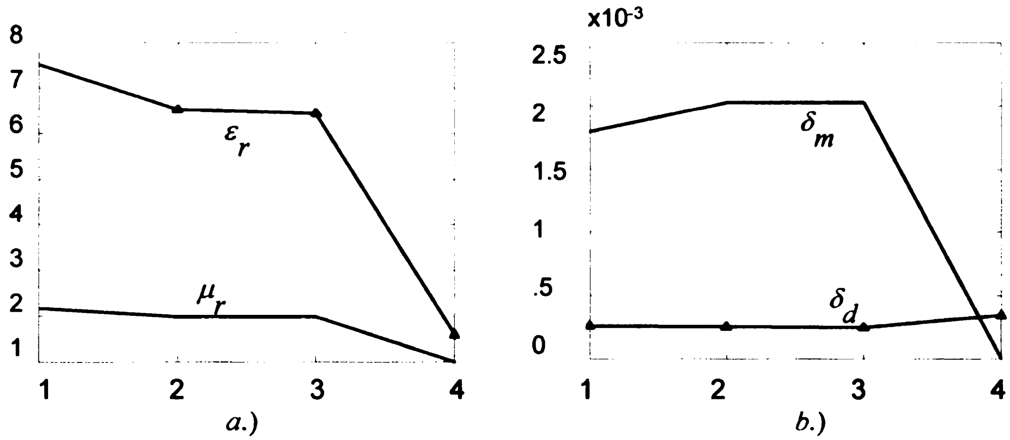

Figure 5.19. Effective permittivity and permeability of composite with holes for volume fraction of 0.45 with YIG as cylindrical inclusion.

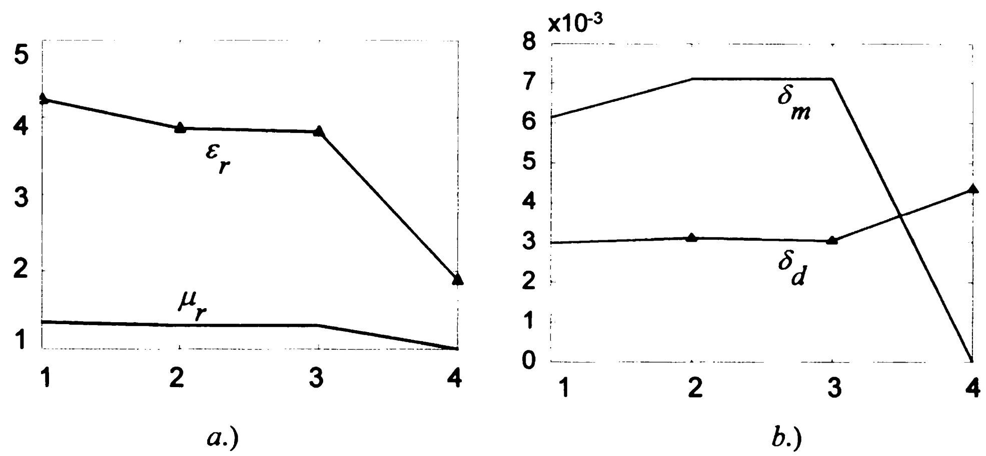

Figure 5.20. Effective permittivity and permeability of composite with holes for volume fraction of 0.18 with YIG as cylindrical inclusion.

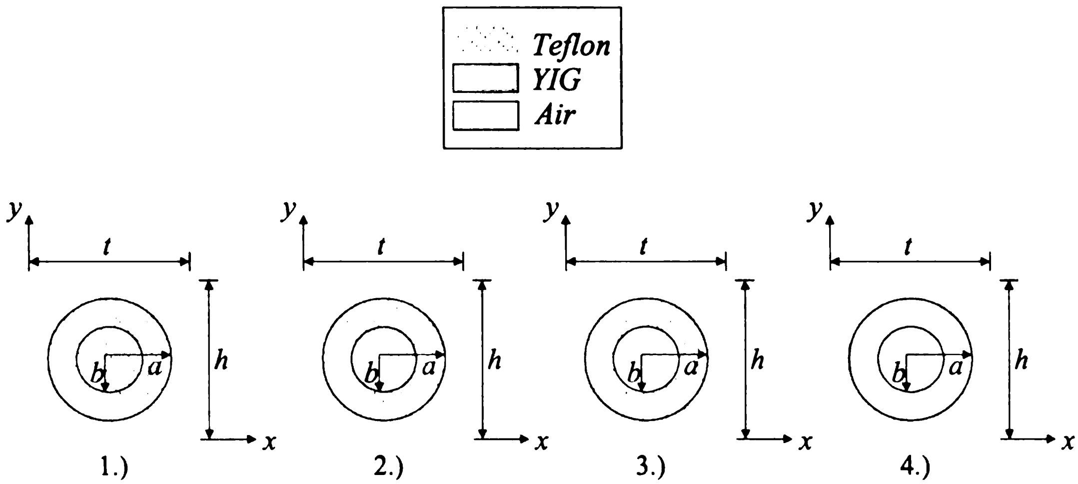

Figure 5.21. Geometry for analysis on effects of air gaps on permittivity and permeability.

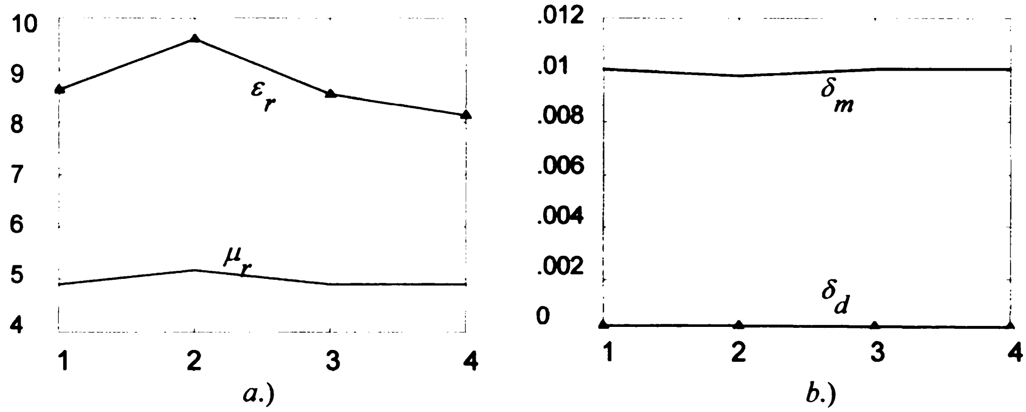

Figure 5.22. Effective permittivity and permeability of composite with holes for volume fraction of 0.45 with Teflon as cylindrical inclusion.

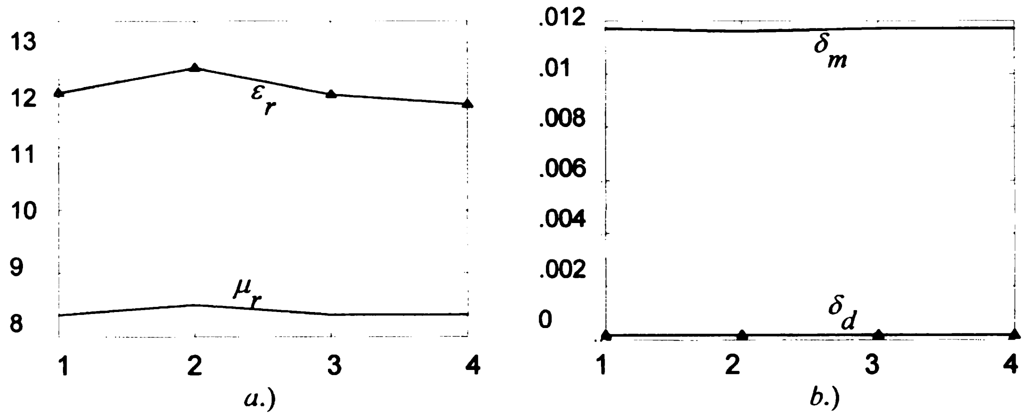

Figure 5.23. Effective permittivity and permeability of composite with holes for volume fraction of 0.18 with Teflon as cylindrical inclusion.

CHAPTER 6

CONCLUSIONS AND FUTURE WORK

Presented in this work is a foundation for composite material design. Using various methods including both analytical and numerical techniques, accurate electromagnetic models have been formulated for three geometries of two-phase composite materials. These geometries include: spherical inclusions, alternating layers, and cylindrical inclusions. The following sections summarize the work done in the previous chapters on composite modeling followed by a description of future work in the field of composite simulation and design.

6.1 Material Characterization

In this dissertation, material characterization involves the process of indirectly measuring the electromagnetic properties of materials. Two of the various material characterization methods employed at Michigan State University have been introduced in section 2.3. One of the methods uses the E4991A Impedance Analyzer to measure the capacitance and inductance of materials separately in order to calculate the complex permittivity and permeability, respectively. This allows for electromagnetic characterization for disk-shaped materials of fairly small size (diameter$< 20mm$; thickness$< 3mm$) in the frequency range of 100MHz-1GHz. The second method uses a stripline field applicator and a two-dimensional root-searching algorithm to extract the complex permittivity and permeability from the measured scattering parameters. This characterization technique involves a stripline with a center conductor that supports a TEM wave normally incident on the material being interrogated in the frequency range of 1-18GHz. This is the basis for the electromagnetic models created in this dissertation for layered composites and composites with cylindrical inclusions where the scattering parameters are the focus of the calculations. These calculated scattering parameters are used in conjunction with the root-searching algorithm to determine the effective permittivity and permeability of the composites.

6.2 Composites and Unique Contributions

6.2.1 Composites with Spherical Inclusions

Composites with spherical inclusions have been investigated in [3] and summarized in this work for sake of entirety. Three of the many classical mixing laws for effective permittivity and a composite consisting of small dielectric particles dispersed throughout a dielectric background were summarized. Based on the concept of duality, these classical mixing laws were used to predict permeability of a magneto-dielectric composite. Through experimental measurements, the author was able to show that the classical mixing laws were capable of accurately predicting the effective permittivity of a magneto-dielectric composite for low volume fractions (e.g. $f \lessapprox 0.3$). However, these mixing laws are not dependable for predicting the effective permeability nor were they capable of determing effective permittivity for composites with high volume fractions. The reason for this is due to the lack of particle to particle interactions in the classical mixing law formulations.

6.2.2 Composites of Alternating Layers

Using the method of wave matrices, composites consisting of alternating layers were analyzed for both isotropic and anisotropic materials. This formulation provided an analytic solution for the scattering paramters of a layered composite from which the effective permittivity and permeability can be extracted using the same methods as the stripline material characterization techniques. This fast and relatively straightforward process for calculating the scattering parameters provided a very useful tool in the analysis of how the electromagnetic properties are effected by various aspects of layered composites. The author was able to demonstrate three degrees of freedom in the design of a layered composite with tunable permittivity and permeability. These degrees of design freedom include: the number of layers, the volume fractions of the materials, and the difference in the constitutive parameters of the materials being combined. The latter of these is termed the dielectric or magnetic contrast ratio. Using actual materials, namely YIG and Teflon, the author showed how the effective permittivity and permeability varied as the number of layers and the volume fraction were increased. As a final illustration of the usefulness of this formulation, a material exhibiting both negative permittivity and permeability was demonstrating by interchanging the Telfon layers with plasma tubes. By controlling the external bias field, the permeability tensor of YIG is shown to have negative values at frequencies greater than ferrimagnetic resonance and the permittivity tensor of the plasma yields negative effective values at frequencies below the plasma frequency. An important point in this example is that the coalescence of these materials biased by a static magnetic field revealed that a double-negative material (i.e. simultaneous negative permittivity and permeability) is acheivable without the use of periodic metallic structures.

6.2.3 Composites with Cylindrical Inclusions

The final composite analyzed in this dissertation is one involving cylindrically shaped inclusions. An integral equation formulation was utilized to model a penetrable two-dimensional geometry. The periodicity of the composite was incorporated in the periodic Green's function and it was shown how the Poisson summation formula was able to accelerate its convergence. Just as in the layered composite analysis, the materials being used to form the mixture are YIG and Teflon. The first analysis of this composite involves increasing the number of cylinders in the direction of propagation of the incident wave. It was shown how the number of cylinders, whether in-line or staggered, has no change on the effective permittivity or permeability for inclusions spaced evenly in both the directions transverse and parallel to the direction of propagation. In the final portion of this section, the author demonstrated how the volume fraction of the YIG was able to yield a tunable range of permittivity and permeability. An even greater permeability was achieved in the case of a YIG background with either Teflon or free-space cylindrical inclusions. However, this configuration yielded loss tangents on the order of 10^{-2}. In conclusion, the only degrees of freedom in the design of a composite with cylindrical inclusions are the volume fraction and the contrast ratios.

6.3 Future Work

The work presented in this dissertation formed a foundation for RF composite design by analyzing three geometries of two-phase mixtures. In the analysis of layered composite, only the case of normal incidence has been considered. This has allowed the author to simulate the characterization technique used by the stripline field applicator in which scattering parameters for normal incidence are used to extract permittivity and permeability. However, the effects of propagation in the direction not parallel to the axis of the stack of layers could yield interesting values for permittivity and permeability. This might involve altering the root searching algorithm used in the extraction process to account for off-normal incidence. In the calculation of the reflection and transmission coefficients, Snell's law must be obeyed at each interface. Also, in this dissertation the layered composites have consisted of mixtures of two dissimilar materials and the effects of layering, volume fraction, and contrast ratio have demonstrated a tunable permittivity and permeability. The use of multiple materials in various combinations could present many different results and therefore an optimization routine for layered composites should be implemented that allows the user to specify either a desired amount of reflection and transmission or a specific permittivity and permeability.

In the geometry with rod shaped inclusions aligned along the z-axis, it was shown how the volume fraction of YIG was able to alter the permittivity and permeability of the composite. However, rather high volume fractions were a necessity for appreciable tunable permeability with the consequence of loss tangents on the order of 10^{-2}. Future analysis of this form of geometry would involve finite length cylindrical inclusions aligned along the z-axis, but with propagation also along the axis of the cylinders rather than perpendicular. The initial difficulty in this work would be the need to overcome the demagnetization factor of the rod for bias fields transverse to the direction of propagation.

Besides further analysis on the geometries presented in this disseration, other geometries should be investigated. One such geometry is that of hexagonal flakes evenly dispersed throughout a background material. These flakes could improve packing and also allow for greater flexibility in a composite mixture.

Also, characterization of materials is important in the design of composites. Verification of the models could be obtained through various characterization techniques already utilized at Michigan State University if the composites discussed could be manufactured for testing. Finally, applications for these materials should be provided to demonstrate their usefulness. For example, using a properly designed magneto-dielectric material to reduce the overall size of a patch antenna while simulataneously increasing the bandwidth.

BIBLIOGRAPHY

BIBLIOGRAPHY

[1] R.C. Hansen and M. Burke, "Antennas with Magneto-Dielectrics," Microwave and Optical Technology Letters, 26(2), 75-78, July 20, 2000.

[2] O. Acher, "Frequency Response of Engineering of Magnetic Composite Materials", Advances in Electromagnetics of Complex Media and Metamaterials. 39-59, 2003.

[3] D. Killips, "Classical Mixing Approaches to Determine Effective Permittivity and Permeability of a Two-Phase Mixture," M.S. Thesis, Michigan State University, East Lansing, MI, 2004.

[4] A. Sihvola, *Electromagnetic mixing formulas and applications,* London: The Institution of Electrical Engineers, 1999.

[5] D.J. Infante, Applications and Theory of Broadband Stripline Field Applicators, Michigan State University: February 2000.

[6] Agilent Technologies, Agilent E4991A RF Impedance/Material Analyzer Operation Manual, Agilent, July 2006.

[7] G. Maze, S. Tedjini, and J-L Bonnefoy, "Effect of anisotropic layers on the characteristics of MMIC's", 20th European Microwave Conference, Oct. 1990.

[8] O. Acher, P.L. Gourierec, G. Perrin, P. Baclet, and O. Roblin, "Demonstration of anisotropic composites with tuneable microwave permeability manufactured from ferromagnetic thin films", IEEE Transactions on Microwave theory and techniques, Vol. 44, No. 5, May 1996.

[9] C.L. Holloway, M. Sabrina Sarto, and M. Johansson, "Analyzing carbon fiber composite materials with equivalent layer models", IEEE Transactions on electromagnetic compatibility, Vol. 47, No. 4, Nov. 2005.

[10] J. Ish-Shalom, "Composite magnetic structure for planar motors", IEEE Transactions on magnetics, Vol. 31, No. 6, Nov. 1995.

[11] S.A. Tretyakov, I.S. Nefedov, P.A. Belov, and A.J. Viitanen, "Recent developments in exotic materials: negative permittivity and permeability, nonreciprocal composites", 14th International Conference on Microwaves, Radar and Wireless Communications, 2002, MIKON-2002.

[12] M. Amano and Y. Kotsuka, "A method of effective use of ferrite for microwave absorber", IEEE Transactions on Microwave Theory and Techniques, Vol. 51, No. 1, Jan. 2003.

[13] C.G. Aumiller, D.H. Harris, M.C. Willson, Y.S. Wu, F.J. Rosenbaum, and D.L. LaCombe, "Ferrite-dielectric composite integrated microwave circuit development", GMTT International Microwave Symposium Digest, Vol. 71, Issue 1, May 1971.

[14] O. Ouchette, S. Zouhdi, A. Bossavit, G. Griso, and B. Miara, "Modeling of 3D periodic multiphase composites by homogenization", IEEE Transactions on Microwave Theory and Techniques, Vol. 54, No. 6, June 2006.

[15] P. Jacquart and O. Acher, "Permeability measurement on composites made of oriented metallic wires from 0.1 to 18 GHz", IEEE Transactions on Microwave Theory and Techniques, Vol. 44, No. 11, Nov. 1996.

[16] V. Bannyi, A. Makarevich, and L. Pinchuk, "Radioabsorbing composite materials based on thermoplastics: production technology and structural optimization principles", 33rd European Microwave Conference, Munich 2003.

[17] A. Bogle, "Electromagnetic Material Characterization using a Partially Filled Rectangular Waveguide", M.S. Thesis, Michigan State University, East Lansing, MI, 2004.

[18] B.B. Szendrenyi, K. Kazi, and I. Mozes, "An alternative broadband method for automatic measurement of the complex permeability and permittivity of materials at microwave frequencies", IEEE MTT-S International Microwave Symposium Digest, May 1988.

[19] J.A. Jargon and M.D. Janezic, "Measuring complex permittivity and permeability using time domain network analysis", IEEE MTT-S International Microwave Symposium Digest, June 1996.

[20] S.V. Maly, "The technique for calculation of the electromagnetic properties of composite materials and nonuniform media", VIII-th International Conference on Mathemattical Methods in Electromagnetic Theory, Kharkov, Ukraine, 2000.

[21] P.I. Somlo, "A convenient self-checking method for the automated microwave measurement of μ and ε", IEEE Transactions on Instrumentation and Measurement, Vol. 42, No. 2, April 1993.

[22] B.K. Chung, "Dielectric constant measurement for thin material at microwave frequencies", Progress in Electromagnetics Research, PIER 75, 239-252, 2007.

[23] W.E. Courtney, "Analysis and evaluation of a method of measuring the complex permittivity and permeability of microwave insulators", IEEE Transactions on Microwave Theory and Techniques, Vol. MTT-18, No. 8, August 1970.

[24] A. Bogle, L. Kempel, E. Rothwell, D. Nyquist, M. Hawley, S. Schneider, and M. Havrilla, "Measurement techniques for ferrromagnetic materials using a stripline", IEEE Antennas and Propagation Society Internation Symposium, Vol. 4, pp. 456-459, June 2003.

[25] M.D. Deshpande, C.J. Reddy, P.I. Tiemsin, and R. Cravey, "A new approach to estimate complex permittivity of dielectric materials at microwave frequencies using waveguide measurements", IEEE Transactions on Microwave Theory and Techniques, Vol. 45, No. 3, March 1997.

[26] D. Misra, M. Chabbra, B.R. Epstein, M. Mirotznik, an K.R. Foster, "Noninvasive electrical characterization of materials at microwave frequencies using an open-ended coaxial line: test of an improved calibration technique", IEEE Transactions on Microwave Theory and Techniques, Vol. 38, No. 1, January 1990.

[27] Wikipedia contributors, "Composite Material", *Wikipedia, The Free Encyclopedia*, http://en.wikipedia.org/w/index.php?title=Composite_material&oldid=144672083> [accessed July 16, 2007].

[28] H. Ishida, "Chapter 5: Introduction to Polymer Composite Processing", NSF Center for Molecular and Microstructure of Composites (CMMC), Department of Mascromolecular Science, Case Western Reserve University, Cleveland, OH. http://filer.case.edu/org/emac270.

[29] I.V. Lindell and A.H. Sihvola, "Effective Permeability of Mixtures", PIER 6: Progress in Electromagnetics Research: Dielectric Properties of Heterogeneous Materials. New York: Elsevier Science Publishing Co., Inc., 1992.

[30] J.A. Kong and A.H Sihvola, "Effective permittivity of dielectric mixtures", IEEE Transactions Geoscience Remote Sensing, 26(4), 420-429, July 1988.

[31] J.C. Maxwell Garnett, "Colours in metal glasses and metal films", Trans. of the Royal Society, (London), CCIII, 1904, pp. 385-420.

[32] D.A.G. Bruggeman, "Berechnung verschiedener physikalischer Konstanten von heterogenen Substanzen, I. Dielektrizitätskonstanten und Leitfähigkeiten der Mischkörper aus isotropen Substanzen", Annalen der Physik, 1935, Ser. 5, 24, pp. 636-664.

[33] D. Polder and J.H. Van Santen, "The effective permeability of mixtures of solids", Physica, 1946, XII, (5), pp. 257-271.

[34] G.P. De Loor, "Dielectric properties of heterogeneous mixtures containing water", The Journal of Microwave Power, 1968, 3, pp. 67-73.

[35] C.J.F. Böttcher, *Theory of electric polarization'* Elsevier, Amsterdam, 1952.

[36] G. Grimvall, *Thermophysical properties of materials,* North-Holland, Amsterdam, 1986.

[37] L. Tsang, J.A. Kong, and R.T. Shin, *Theory of microwave remote sensing,* Wiley, New York, 1985.

[38] E.J. Rothwell and M.J. Cloud, *Electromagnetics,* CRC Press, Boca Raton, Florida, 2001.

[39] R.E. Collin, *Field Theory of Guided Waves,* McGraw-Hill Book Company, New York, New York, 1960.

[40] D.M. Pozar, *Microwave Engineering, 3rd ed.,* John Wiley and Sons, Inc., Hoboken, New Jersey, 2005.

[41] W.C. Chew, *Waves and Fields in Inhomogeneous Media,* Van Nostrand Reinhold, New York, New York, 1990.

[42] M.A. Morgan, D.L. Fisher, and E.A. Milne, "Electromagnetic Scattering by Stratified Inhomogeneous Anisotropic Media", IEEE Trans. on Ant. and Prop., 1987, Vol. AP-35, No. 2.

[43] C. G. Parazzoli, R.B. Greegor, K. Li, B.E.C. Koltenbah, and M. Tanielian, "Experimental verification and simulation of negative index of refraction using Snell's Law," Phys. Rev. Ltrs., 90, March 2003.

[44] B. Munk, "Negative μ and ε: Fact and fiction," unpublished work, 2004.

[45] S. Zuo, K. Hemawan, J.J. Narendra, T. Grotjohn, and J. Asmussen, "Miniature microwave plasma torch applicator and its characteristics," ICOPS 2004, p. 310, July 2004.

[46] Chen, F.F., *Introduction to Plasma Physics and Controlled Fusion*, New York, New York: Plenum Press, 1984.

[47] J.B. Jarvis, M.D. Janezic, B.F. Riddle, R.T. Johnk, P. Kabos, C.L. Holloway, R.G. Geyer, and C.A. Grosvenor, "NIST Technical Note 1536: Measuring the Permittivity and Permeability of Lossy Materials: Solids, Liquids, Metals, Building Materials, and Negative-Index Materials". Boulder, CO: National Institute of Standards and Technology, Dec. 2004.

[48] Alu, Andrea and Engheta, Nader, "Pairing an Epsilon-Negative Slab With a Mu-Negative Slab: Resonance, Tunneling and Transparency," IEEE Transactions on Antennas and Propagation. Vol. 51, No. 10, Oct. 2003.

[49] P. Baccarelli, P. Burghignoli, G. Lovat, and S. Paulotto, "Surface-Wave Suppression in a Double-Negative Metamaterial Grounded Slab," IEEE Antennas and Wireless Propagation Letters. Vol. 2, 2003.

[50] C.L. Holloway, E.F. Kuester, J.B. Jarvis, and P. Kabos, "A Double Negative (DNG) Composite Medium Composed of Magnetodielectric Spherical Particles Embedded in a Matrix" IEEE Transactions on Antennas and Propagation. Vol. 51, No 10, Oct. 2003.

[51] D.A. Smith, and N. Kroll, "Negative refractive index in left-handed materials," Phys. Rev. Lett., Vol. 85, pp. 2933-2936, 2000.

[52] C. Caloz, C.C. Chang, and T. Itoh, "Full-wave verification of the fundamental properties of left-handed materials in waveguide configurations," J. Appl Phys., Vol. 90, pp. 5483-5486, 2001.

[53] E. Michielssen, A.F. Peterson, and R. Mittra, "Oblique scattering from inhomogeneous cylinders using a coupled integral equation formulation with triangular cells," IEEE Transactions on Antennas and Propagation. Vol. 39, No 4, April 1991.

[54] A.F. Peterson, S.L. Ray, and R. Mittra, *Computation Methods for Electromagnetics*, Oxford, Tokyo, Melbourne: Oxford Univeristy Press-IEEE Press, 1998.

[55] B. Shanker and E. Michielssen, "Oblique scattering from an inhomogeneous chiral cylindrical object with use of axial Beltrami fields and the fast multipole method," J. Opt. Soc. Am. A. Vol. 14, No 10, Oct. 1997.

[56] A.W. Mathis and A.F. Peterson, "A Comparison of acceleration procedures for the two-dimensional periodic green's function," IEEE Transactions on Antennas and Propagation. Vol. 44, No 4, April 1996.

[57] R.E. Jorgenson and R. Mittra, "Efficient calculation of the free-space periodic green's function," IEEE Transactions on Antennas and Propagation. Vol. 38, No 5, May 1990.

[58] R.F. Harrington, *Field Computation by Moment Methods*, Malabar, FL: Krieger, 1982 reprint.

[59] K. Kamogawa, T. Tokumitsu, and M. Aikawa, "Multifrequency microstrip antennas using alumina-ceramic/polyimide multilayer Dielectric substrate," IEEE Transactions on Microwave Theory and Techniques. Vol. 44, No. 12, December 1996.

[60] Y. Lee, X. Lu, Y. Hao, S. Yang, R. Ubic, J.R.G. Evans and C.G. Parini, "Directive millimetre-wave antenna based on freeformed woodpile EBG structure," Electronics Letters, Vol. 43, No. 4, February 2007.

[61] Y. Taguchi, K. Miyauchi, and T. Ishida, "A GHz-band ceramic multi-layer substrate and its application to a hybrid IC," IEEE MTT-S International Microwave Symposium Digest, Vol. 3, 1993.

[62] T. Seki, H. Yamamoto, T. Hori, and M. Nakatsugawa, "Active antenna using multi-layer ceramic polymide substrates for wireless communication systems," IEEE MTT-S International Microwave Symposium Digest. Vol. 1, May 2001.

[63] R.F. Harrington, *Time-Harmonic Electromagnetic Fields*, New York, New York: Wiley-IEEE Press, 2001.